(25)

N73-11266

NASA TECHNICAL REPORT

NASA TR R-388

NASA TR R-388

AN IMPLICIT FINITE-DIFFERENCE SOLUTION TO THE VISCOUS SHOCK LAYER, INCLUDING THE EFFECTS OF RADIATION AND STRONG BLOWING

by L. Bernard Garrett, G. Louis Smith,
and John N. Perkins

Langley Research Center
Hampton, Va. 23365

NATIONAL AERONAUTICS AND SPACE ADMINISTRATION • WASHINGTON, D. C. • NOVEMBER 1972

1. Report No. NASA TR R-388	2. Government Accession No.	3. Recipient's Catalog No.

4. Title and Subtitle
AN IMPLICIT FINITE-DIFFERENCE SOLUTION TO THE VISCOUS SHOCK LAYER, INCLUDING THE EFFECTS OF RADIATION AND STRONG BLOWING

5. Report Date
November 1972

6. Performing Organization Code

7. Author(s)
L. Bernard Garrett; G. Louis Smith; and
John N. Perkins (North Carolina State University at Raleigh)

8. Performing Organization Report No.
L-8302

9. Performing Organization Name and Address
NASA Langley Research Center
Hampton, Va. 23365

10. Work Unit No.
117-07-04-08

11. Contract or Grant No.

12. Sponsoring Agency Name and Address
National Aeronautics and Space Administration
Washington, D.C. 20546

13. Type of Report and Period Covered
Technical Report

14. Sponsoring Agency Code

15. Supplementary Notes

16. Abstract

An implicit finite-difference scheme is developed for the fully coupled solution of the viscous, radiating stagnation-streamline equations, including strong blowing. Solutions are presented for both air injection and injection of carbon-phenolic ablation products into air at conditions near the peak radiative heating point in an earth entry trajectory from interplanetary return missions. A detailed radiative-transport code that accounts for the important radiative exchange processes for gaseous mixtures in local thermodynamic and chemical equilibrium is utilized in the study.

With minimum number of assumptions for the initially unknown parameters and profile distributions, convergent solutions to the full stagnation-line equations are rapidly obtained by a method of successive approximations. Damping of selected profiles is required to aid convergence of the solutions for massive blowing. It is shown that certain finite-difference approximations to the governing differential equations stabilize and improve the solutions.

Detailed comparisons are made with the numerical results of previous investigations. Results of the present study indicate lower radiative heat fluxes at the wall for carbon-phenolic ablation than previously predicted.

17. Key Words (Suggested by Author(s)) Radiative heat transfer Shock layer, viscous Stagnation flow Equilibrium flow Mass transfer	18. Distribution Statement Unclassified — Unlimited

19. Security Classif. (of this report) Unclassified	20. Security Classif. (of this page) Unclassified	21. No. of Pages 122	22. Price* $3.00

*For sale by the National Technical Information Service, Springfield, Virginia 22151

CONTENTS

AN IMPLICIT FINITE-DIFFERENCE SOLUTION TO THE VISCOUS SHOCK LAYER, INCLUDING THE EFFECTS OF RADIATION AND STRONG BLOWING

By L. Bernard Garrett, G. Louis Smith,
and John N. Perkins*
Langley Research Center

SUMMARY

An implicit finite-difference scheme is developed for the fully coupled solution of the viscous, radiating stagnation-streamline equations, including strong blowing. Solutions are presented for both air injection and injection of carbon-phenolic ablation products into air at conditions near the peak radiative heating point in an earth entry trajectory from interplanetary return missions. A detailed radiative-transport code that accounts for the important radiative exchange processes for gaseous mixtures in local thermodynamic and chemical equilibrium is utilized in the study.

With minimum number of assumptions for the initially unknown parameters and profile distributions, convergent solutions to the full stagnation-line equations are rapidly obtained by a method of successive approximations. Damping of selected profiles is required to aid convergence of the solutions for massive blowing. It is shown that certain finite-difference approximations to the governing differential equations stabilize and improve the solutions.

Detailed comparisons are made with the numerical results of previous investigations. Results of the present study indicate lower radiative heat fluxes at the wall for carbon-phenolic ablation than previously predicted.

INTRODUCTION

A blunt spacecraft entering planetary atmospheres at earth hyperbolic speeds encounters intense radiative heating rates, particularly in the frontal or stagnation region. Acceptable interior temperatures can be maintained by mass-transfer cooling through the use of heat shields constructed of polymeric ablator materials (Walberg and Sullivan (ref. 1)). Near altitudes for peak heating in many entry trajectories, such as the trajectory for entry into the Earth's atmosphere from a direct-return Mars mission, the mass of gas from ablation products injected into the flow field is an appreciable fraction of the

---

* Professor, North Carolina State University at Raleigh.

mass of the oncoming flow (Chin (ref. 2)) and can blow the viscous boundary layer off the surface of the spacecraft.

This condition, which is generally referred to as strong, or massive, blowing, has a physically destabilizing effect on the flow field which seriously impairs numerical solutions to the governing equations (Libby and Sepri (ref. 3)). Libby (ref. 4) describes the physics of the problem to be that of an inner region near the wall which is dominated by pressure and inertia forces and in which viscous effects are small, and a thin viscous region which adjusts to the flow in the outer inviscid region. For small blowing rates, the viscous boundary layer is attached to the wall, and the presence of the solid wall has a stabilizing effect on the flow. However, for the strong-blowing problem the boundary layer is not attached to the wall, and the gaseous inner layer may destabilize the flow.

The problem of massive blowing where the viscous flow adjusts to the outer inviscid flow has been studied extensively for nonradiating flows (cf., e.g., refs. 3 to 7). However, there has been limited attention directed to the solution when radiation is coupled into the problem. Numerous previous investigators using a variety of assumptions and numerical techniques have arrived at different conclusions regarding the effects of ablation products on the attenuation of radiation. These approaches either required excessive computer time for the numerical solution or were approximate analyses which led to questionable inputs of the thermodynamic properties required for the radiation computations. Since radiative heat fluxes (in addition to being strong functions of temperature and density) can also be sensitive to the chemical species within the shock layer, some of which are strong radiation emitters and absorbers (Hoshizaki and Lasher (ref. 8)), care should be taken in defining these quantities across the entire shock layer.

The purpose of this investigation is to develop an approach for the numerical solution to the coupled equations for the viscous, radiating flow field along the stagnation line of a blunt body under both weak and strong blowing conditions. The method solves the governing Navier-Stokes equations without making unnecessary simplifying assumptions to the equations or in the numerical solution which could degrade the radiative-flux computations.

An implicit finite-difference method, which has previously been shown to be computationally efficient for chemical-nonequilibrium studies without mass addition (Blottner (ref. 9)), is developed for the solution to the proposed problem. The nonlinear governing differential equations are written in finite-difference form at all nodal points within the shock layer, with boundary conditions specified at the wall and immediately behind the shock. The formulation results in a tridiagonal matrix system of algebraic equations which is efficient for machine computation. The governing equations are solved "one at a time" in succession across the entire shock layer. The technique for the overall numerical solution to the two-point boundary problem is by iteration of the flow variables at each nodal point in the shock layer. Since the governing equations are solved one at a time rather than concurrently at each nodal point (as in initial-value forward-integration techniques), then the nodal-spacing requirement for all the equations is not limited by the stability requirement of the most unstable equations.

The stability of the finite-difference solutions to the governing equations is treated extensively. Particular attention is directed to the stability of the species-continuity equation with binary diffusion by using central differencing and a two-point windward-differencing scheme that provides automatic damping of the profiles.

Radiation computations are carried out with the use of an existing radiative-transport computer program, RATRAP, which was developed by Wilson and Hoshizaki (e.g., ref. 10) for a nongray gas. The program uses the tangent-slab approximation (one-dimensional) that accounts for absorption and emission within a layer of arbitrary optical thickness and is for equilibrium gaseous mixtures of hydrogen, carbon, nitrogen, and oxygen. Profiles of pressure, enthalpy, and elemental composition are computed by the viscous-flow-field solution and are used as inputs to the radiation program. Radiative fluxes are evaluated at various nodal points within the shock layer to provide coupling with the flow field. The transport properties for equilibrium air (i.e., viscosity and reactive Prandtl number, see Hansen (ref. 11)) are used in the computations to account for the energy transport due to binary diffusion.

Numerical results are presented for both air-to-air injection and for the injection of the ablation products of a carbon-phenolic ablating heat shield into an airstream for a range of blowing rates of interest. Additional computations are presented for constant-density flows and for viscous, nonradiating flows with air-to-air injection.

The air-to-air injection cases include calculations for a body with a spherical nose radius of 3.05 meters entering the earth's atmosphere at a velocity of 15.24 kilometers per second, at an altitude of 61 kilometers, and with a ratio of blowing mass rate to free-stream mass-flow rate of 0.1. The results are compared with the initial-value forward-integration method of Rigdon et al. (ref. 12), the integral approaches of Smith et al. (ref. 13), and an "exact" numerical solution of Wilson (ref. 14), for identical free-stream and wall boundary conditions. An assessment is made of some approximations contained in these analyses.

REVIEW OF LITERATURE

Recent reviews of the advances in analyses for the radiating shock layer are given by Anderson (ref. 15), Garrett (ref. 16), and Goulard et al. (ref. 17). Investigations related to the present work are reviewed in this section.

Radiation-Transport Models

Some existing radiation-transport computer programs which consider ablation products in addition to air chemical species are RATRAP, developed by Hoshizaki and Wilson (see Wilson (ref. 10)); SPECS, developed by Thomas (ref. 18); and RADICAL, developed by Nicolet (refs. 19 and 20). These programs, which perform radiation computations based on the spectral details of the individual chemical species, are time consuming for stagnation-line analyses. However, usage of this type of program is required since realistic analyses have indicated that the addition of ablation products to the flow field can reduce the heat fluxes to the body by factors of 2 below those for pure-air flow. (See, e.g., Hoshizaki and Lasher (ref. 8), Coleman et al. (ref. 21), and Chin (ref. 2).)

For air, significant differences still exist not only in the spectral absorption coefficients for certain chemical species but also in the radiation models that are coded for computer solutions (Suttles (ref. 22)). It is noted that differences in the heat-flux predictions at the body can result not only from differences in the radiation-transport codes but also from the inaccuracies in the solutions to the flow equations. In particular, the predicted concentration, or number density, of strongly absorbing or emitting chemical species in the ablation products can be greatly affected by computed temperatures and densities within the shock layer.

RATRAP is used in this analysis. This program is somewhat time consuming but contains the appropriate detail for the rigorous flow-field computations of the present analysis.

Flow-Field Analyses With Radiation

The appearance of the divergence of the radiative flux as a term in the general energy equation describing the flow of a radiating gas couples the flow-field and the radiative-transport analyses. For hyperbolic entry velocities, typical of return missions from Mars, the radiative heat fluxes are large, and thus radiative cooling (energy losses) with the shock layer must be considered. The net effect of radiative cooling is a reduction of the radiative heat flux to the body because of a decrease in temperature and a subsequent increase in shock-layer density from that for adiabatic conditions. (See, e.g., Wick (ref. 23) and Hoshizaki and Wilson (ref. 24).) This coupling between radiative transport and gas dynamics for this problem is commonly referred to as the "coupled radiating shock-layer problem."

Howe and Viegas (ref. 25) were the first to investigate the flow of a viscous, radiating, self-absorbing gas in the stagnation region with the effects of mass addition included. Since they assumed a gray radiation model, the radiation-flux results are not quantitative. For the axisymmetric stagnation region, they reduced the Navier-Stokes equations to ordinary differential equations. They solved the momentum equation numerically by an initial-value forward-integration method. The energy and species-continuity equations were solved by numerical evaluation of the exponential integrals that appear in the exact analytical solutions to the differential equations. The solution to the coupled system of equations was iterated by convergence on the value of the shear stress at the wall. In the fully viscous analysis of Howe and Viegas the mass injection rates were restricted to moderate amounts which did not upset the stability of the boundary layer near the wall. The difficulty with the stronger blowing rates can be traced to numerical instability problems associated with evaluating the exponential integrals in the exact analytical solutions to the governing equation.

Wilson (ref. 14), who applied an approach similar to that of Howe and Viegas (ref. 25) (with the notable exception being his momentum-equation solution), describes the problem for the fully viscous shock layer with massive blowing to be one of numerical precision required to take the differences between the large numbers which appear in the exponential integrals. Further aspects of this problem will be discussed in association with Wilson's paper (ref. 14) and in the section "Results and Discussion."

Hoshizaki, Wilson, and Lasher developed integral methods for the coupled solution of the viscous, radiating shock layer around a blunt body (refs. 24, 26, and 8). In each paper, the velocity profile was expressed as a fifth-order polynomial. In reference 8 by Hoshizaki and Lasher, the species continuity and energy equations were solved by means of similarity transformations and numerical integration of the resulting exponential integrals. Their detailed analysis of the spectral absorption coefficients for 20 air and ablation-product chemical species showed that the carbon atoms, which diffuse far into the shock layer, act as strong radiation absorbers.

Chin (ref. 2) developed a numerical method for solving the coupled equations for the radiating, inviscid stagnation flow with mass addition. He integrated the conservation equations for the air layer from the shock wave to the interface between the air layer and the ablation-products layer, and from the body to the interface. He iterated on the wall heat flux, the blowing rate, and the velocity and enthalpy profiles until the solution converged on the enthalpy distribution and heat flux to the wall. His solutions to the inviscid governing equations converged very rapidly; however, since the viscous region (which typically occupies about 10 percent of the shock layer for the Reynolds numbers of interest) was neglected, there was no mechanism provided for the diffusion of the strongly absorbing carbon atoms and ions into the air layer.

The first numerical solution to the exact Navier-Stokes equations for the thin shock layer at the stagnation line, including radiative transport, was presented by Rigdon, Dirling, and Thomas (ref. 27). This analysis included massive blowing (up to 10 percent) for air-to-air injection. In 1969 they extended the solution to massive blowing of ablation products (ref. 12), with blowing rates up to 20 percent. The numerical procedure which they employed is computationally time consuming. They used an initial-value forward-integration scheme in which they were required to adjust four initial conditions (temperature, tangential velocity gradient, temperature gradient, and the shear) evaluated at the stagnation point. These initial conditions were iterated until the two boundary conditions for both the momentum and energy equations were satisfied at the shock and at the body. In the ablation analysis they were further required to satisfy the binary species-continuity equation over the shock layer. If the same initial-value forward-integration scheme is used, then this requires a guess for the mass fraction of the injected foreign material and its gradient at the stagnation point in order to satisfy the boundary conditions at the shock wave and the body. The net result is the requirement that one guess a priori six coupled initial conditions which are unknown in order to satisfy the boundary conditions.

Rigdon et al. (ref. 12), from the results of their solution to the exact governing equations, were able to make direct comparisons with the integral results of Wilson and Hoshizaki (ref. 28) and concluded that the polynomial approximations which had worked so well in the solution for nonblowing were not sufficient to describe the solution for the momentum equation in the presence of massive blowing. Although differences existed in the radiation models (Rigdon et al. (ref. 12) used the SPECS code of ref. 18, whereas Wilson and Hoshizaki (ref. 28) used an updated version of RATRAP (see ref. 10)), the differences by factors of 2 to 4 in the ablation-layer thicknesses could not be explained on the basis of differences in radiation models.

In reference 14 Wilson concluded that the approximate integral solution to the momentum equation was inadequate for large mass injection and/or the Reynolds numbers of interest. As mentioned previously, his treatment of the energy and species-continuity equations was similar to that of Howe and Viegas (ref. 25). He used similarity conditions to obtain exact analytic solutions to the energy and species-continuity equations. He attributes the momentum-equation solution (see ref. 28) to a solution technique developed by Chou and Blake (ref. 29) for a similar problem. Upon performing an additional coordinate transformation which involves viscosity, and assuming that the density-viscosity product is a constant across the shock layer, Wilson (ref. 14) developed the second-order differential equation. He subsequently differentiated the equation, which makes it linear (in the second derivative), to obtain an exact analytical solution to the equation in terms of exponential integrals. Rather than solve the momentum equation with an initial-value technique as was done by Howe and Viegas (ref. 25), Wilson employed a successive approximation algorithm to all the analytical governing equations. In the successive approximation scheme, which is similar to the technique applied in the present study, the distribution of properties is initially specified across the shock layer and the governing equations are iterated until satisfactory convergence is obtained.

Wilson (ref. 14) observed that with his formulated equations he was unable to obtain a numerical solution to the fully viscous equations for relatively large blowing rates (greater than 5 percent, approximately). As previously mentioned, Wilson traced the problem to numerical instability associated with taking the differences between exponentially large numbers (greater than about e^{10}) which were about the same order of magnitude. Since the computer carries only about eight to 16 significant digits, then the resulting difference between these large numbers becomes meaningless. Apparently, these exponentially large numbers occur in the numerical solution in regions where the viscous effects become small (Wilson observed the effect in the inner region near the wall for large blowing). Part of the problem could be due to the loss in precision when Simpson's rule or the like (Conte (ref. 30)) is used to integrate numerically under an exponential curve.

Wilson (ref. 14) was able to circumvent the numerical precision problem for massive blowing by solving inviscid equations in the inner region and the fully viscous equations at a somewhat arbitrary distance from the body. The interface criteria was that e be raised to a power less than 10.

In reference 13, Smith, Suttles, Sullivan, and Graves presented a combined flowfield and ablation study of a blunt body entering the earth's atmosphere at interplanetary return velocities. The analysis yielded transient histories of ablator mass-loss rate for a complete entry trajectory. Smith, Suttles, et al. (ref. 13) examined the entire subsonic flow region surrounding the blunt body by dividing it into three interacting regions: an inviscid outer layer, a boundary layer, and a charring heat shield. The flow in the inviscid outer layer with radiation was determined by a one-strip integral method developed by Suttles (ref. 31). The combined solution for the inviscid flow field with ablation provided the boundary conditions for the radiating-boundary-layer computations. The boundary-layer and the ablation calculations were iterated until the heating rates and the ablation rates converged. For the larger blowing rates the numerical method for the solution of the boundary-layer equations was not suitable and they adapted an integral procedure by Libby (ref. 6) for the radiating-boundary-layer solution. The solutions for the boundary layer and the inviscid outer layer were joined by assuming a cubic variation for the distribution of the elemental mass fractions within the boundary layer and by adjusting the edge enthalpy condition.

One of the significant conclusions of Smith, Suttles, et al. (ref. 13) was that the introduction of ablation products into the boundary layer did little to attenuate the radiative flux to the wall. In their analysis they used the RATRAP computer code developed by Wilson (ref. 10). Whereas Chin's solutions (ref. 2) for a blowing rate of 7.6 percent and the solutions of Rigdon et al. (ref. 12) for a blowing rate of 20 percent indicated reductions in the wall heat flux of about 45 percent below the nonblowing rates, Smith, Suttles, et al. (ref. 13) calculated reductions of only about 22 percent. Wilson and Hoshizaki (ref. 28) in their approximate integral approach indicated (by use of the RATRAP radiation code) that for a blowing rate of 10 percent, the radiative heat flux was reduced 40 percent below the value for no blowing, and for blowing rate of 20 percent, the heat flux was reduced 60 percent below the no-blowing value. Wilson's more recent results (ref. 14), using his improved momentum-equation solution, have indicated much lower heat-flux reductions (only 18 percent) at blowing rates of 5 and 10 percent. Although there are differences in the free-stream conditions in the studies of references 28 and 14, they do not appear to be sufficient to account for the differences in the radiation blockage effects in the two analyses. Apparently, the answer to these differences must reside in part in the analytical and numerical treatments of the governing flow equations.

One of the questions which the present analysis will attempt to answer is whether the approximate integral treatments of the governing equations and/or "exact" numerical treatments of approximate systems of equations can accurately define the flow properties required for the radiation computations with and without blowing. The numerical technique to be developed for the analysis of the coupled, viscous, radiating flow along the stagnation line with massive blowing included is an implicit finite-difference scheme. Blottner (ref. 9) has shown this approach to be computationally superior to initial-value schemes for studies of the stagnation-line flow with chemical nonequilibrium and without blowing.

In the implicit method, the problem is treated as a two-point boundary-value problem in which boundary conditions are specified at the shock and at the body. The entire shock layer is treated as viscous; thus, no "patching" of two or more solutions is required. The governing equations for the thin shock layer which describe the viscous flow along the stagnation line (Ho and Probstein (ref. 32)) and which are exact through second order are solved at discrete nodal points along the stagnation line by iteration through the application of a method of successive approximations. Singularities do not appear in the formulation since the viscous term takes effect as the convective terms (mass flux) approach zero in the vicinity of the stagnation point.

SYMBOLS

a	tangential velocity gradient
A_n	coefficient of the (n - 1)th unknown quantity for the nth governing equation (see, e.g., eqs. (52) and (53))
B_n	coefficient of nth unknown quantity for the nth governing equation (see, e.g., eqs. (52) and (53))

B_ν	Planck function defined by equation (17), watt-sec/cm^2-sr
c	arbitrary function (see eqs. (42))
c_p	specific heat
C_n	coefficient of the (n + 1)th unknown quantity for the nth governing equation (see, e.g., eqs. (52) and (53))
d_h	damping factor for the enthalpy solution
d_ρ	density damping factor
D_{ij}	binary diffusion coefficient for the ith and jth chemical species
D_n	known function appearing on the right-hand side of the nth governing equation (see, e.g., eqs. (52) and (53))
$\overline{D}_n$	modified known function appearing on the right-hand side of the nth governing x-momentum equation (see eq. (60))
E_2	exponential integral of order 2 (see eq. (17))
f	arbitrary function (see eqs. (42))
h	static enthalpy
$\not{h}$	Planck's constant, $\not{h} = 6.6256 \times 10^{-34}$ J-sec
H	total enthalpy
J_i	mass diffusion flux of the ith chemical species
k	thermal conductivity
k^*	Boltzmann constant, $k^* = 1.38054 \times 10^{-23}$ J/K
K	body curvature, $K = 1/R_b$

M_i	molecular weight of species i, g/g mole
N	total number of nodal points across the shock layer
N_{Pr}	Prandtl number
N_{Re}	Reynolds number defined by $N_{Re} = \frac{\rho'_\infty U'_\infty R'_b}{\mu'_s}$
N_{Sc}	Schmidt number
p	static pressure
$q_{C,y}, q_{D,y}, q_{R,y}$	heat flux in y-direction due to conduction, diffusion, and radiation, respectively
r	radius measured from axis of symmetry of body (see fig. 1)
R_b	body radius
$S(x)$	step function, $S(x) = 0$ for $x < 0$ $S(x) = 1$ for $x \geqq 0$
T'	temperature, K
u	tangential velocity component
U	resultant velocity
v	normal velocity component
v_i	diffusion velocity of the ith chemical species
x	distance measured along the body surface (see fig. 1)
$\overline{X}_i$	mole fraction of the ith chemical species
y	distance measured normal to the body surface (see fig. 1)

α_i	mass fraction of the ith chemical species
$\overline{\alpha}_i$	mass fraction of the ith chemical element
α_ν	modified linear absorption coefficient, cm^{-1}
β	pressure-gradient term (see eq. (14))
$\hat{\delta}$	normalizing parameter in the y to η transformation defined by $\hat{\delta} = \int_0^{y_s} \rho(y)dy$
$\Delta\eta$	nodal spacing
ϵ_i'/k^*	molecular constant for the ith chemical species (see eq. (25)), K
ϵ_{ij}'/k^*	molecular constant for the ith and jth chemical species (see eq. (25)), K
ϵ_n	error in the ith iteration at the nth nodal point
ζ	dummy variable
η	transformed coordinate defined by equation (30)
θ_b	local body angle
κ	scale factor, $\kappa = 1 + Ky = 1 + K\hat{\delta}\int_0^\eta \frac{d\eta}{\rho}$
λ	eigenvalue for the stability analysis
μ	viscosity (also dummy variable used in exponential term E_2 in eq. (17))
ρ	density
σ_i'	collision cross section of species i, Å
σ_{ij}'	mean collision cross section for species i and j, Å
τ	convergence integral

$\dot{\omega}_i$	net volumetric rate of production of species i
$\Omega_{ij}^{(1,1)*}$	reduced collision integral used in equation (25)

Subscripts:

A	air products
F	foreign or ablation products
inj	injected species (at $\eta = 0$)
n	nth nodal point; $n = 1$ at the body ($\eta = 0$) and $n = N$ at the shock ($\eta = 1$)
s	shock
w	wall
∞	free-stream conditions

Superscript:

i	ith iteration

Primed quantities are dimensional.

ANALYSIS

Thin-Shock-Layer Equations

The governing equations for the steady-state flow of a viscous radiating gas in the stagnation region of a blunt axisymmetric body at moderate-to-high Reynolds numbers are given by Ho and Probstein (ref. 32) and by Scala (ref. 33). These equations are

Continuity:

$$\frac{\partial}{\partial x'}(r'\rho'u') + \frac{\partial}{\partial y'}(\kappa' r'\rho'v') = 0 \tag{1}$$

x-momentum:

$$\rho'u'\frac{\partial u'}{\partial x'} + \kappa'\rho'v'\frac{\partial u'}{\partial y'} + K'\rho'u'v' = -\frac{\partial p'}{\partial x'} + \frac{\partial}{\partial y'}\left(\kappa'\mu'\frac{\partial u'}{\partial y'}\right) \tag{2}$$

y-momentum:

$$\rho' u' \frac{\partial v'}{\partial x'} + \kappa' \rho' v' \frac{\partial v'}{\partial y'} - K' \rho' (u')^2 = -\kappa' \frac{\partial p'}{\partial y'} \tag{3}$$

Energy:

$$r' \rho' u' \frac{\partial H'}{\partial x'} + \kappa' \rho' v' r' \frac{\partial H'}{\partial y'} = - \frac{\partial}{\partial y'} \left[\kappa' r' \left(q'_{C,y} + q'_{D,y} + q'_{R,y} \right) \right] + \frac{\partial}{\partial y'} \left(\kappa' r' \mu' u' \frac{\partial u'}{\partial y'} \right) \tag{4}$$

Species continuity:

$$\frac{\partial}{\partial x'} \left(r' \rho' u' \alpha_i \right) + \frac{\partial}{\partial y'} \left(\kappa' r' \rho' v' \alpha_i \right) = - \frac{\partial}{\partial y'} \left(\kappa' r' J'_{i,y} \right) + \kappa' r' \dot{\omega}'_i$$

$$(i = 1, \ldots, M \text{ species}) \tag{5}$$

Primed symbols are used to denote dimensional quantities; unprimed, dimensionless quantities.

For the body-oriented coordinate system shown in figure 1, the quantity κ', which is the coordinate stretching function, is defined by

$$\kappa' = 1 + K' y' \tag{6a}$$

where

$$K' = K'(x) = \frac{1}{R'_b} \tag{6b}$$

and r satisfies the equation

$$dr' = \kappa' \sin \theta_b \, dx' + \cos \theta_b \, dy' \tag{6c}$$

In equations (4) and (5), the quantities $q'_{C,y}$, $q'_{D,y}$, and $q'_{R,y}$ are the heat fluxes in the y'-direction due to conduction, diffusion, and radiation, respectively; $J'_{i,y}$ is the mass diffusion flux in the y'-direction; and $\dot{\omega}'_i$ is the net rate of production of the ith chemical species.

In comparison with the heat and mass diffusion fluxes in the y'-direction, the corresponding fluxes in the x'-direction are generally considered negligible in the stagnation region. (See Ho and Probstein (ref. 32).) These fluxes in the x'-direction are assumed to be negligible in the present analysis also. The equations for the thin shock layer are the simplified boundary-layer equations (Navier-Stokes) including the curvature terms for the stagnation region. The equations are considered to be accurate to the order $\left(\frac{\rho'_\infty}{\rho'_s} N_{Re}\right)^{-1}$ (ref. 32), where $N_{Re} = \frac{\rho'_\infty U'_\infty R'_b}{\mu'_s}$, when radiation is not considered.

Stagnation-Streamline Equations

At the stagnation line (x = 0), the conservation equations for the thin shock layer reduce to ordinary differential equations upon expanding the flow variables in the following power series (based on symmetry considerations):

$$\left.\begin{aligned} u &= a(y)x + a_1(y)x^3 + \ldots \\ v &= v(y) + v_1(y)x^2 + \ldots \\ \rho &= \rho(y) + \rho_1(y)x^2 + \ldots \\ H &= H(y) + H_1(y)x^2 + \ldots \\ \alpha_i &= \alpha_i(y) + \alpha_{i1}(y)x^2 + \ldots \end{aligned}\right\} \tag{7}$$

applying the geometry relations (eqs. (6)), and then taking the limit as $x \rightarrow 0$. The limiting forms of the governing equations for the stagnation-line flow become

Continuity:

$$\frac{d\left(\kappa^2 \rho v\right)}{dy} = -2\kappa\rho a \tag{8}$$

x-momentum:

$$-\frac{\kappa}{N_{Re}} \frac{d}{dy}\left(\mu \frac{da}{dy}\right) + \kappa\rho v \frac{da}{dy} + \rho a^2 + K\rho v a = \beta \tag{9}$$

y-momentum:

$$\rho v \frac{dv}{dy} = -\frac{dp}{dy} \tag{10}$$

Energy:

$$\kappa^2 \rho v \frac{dH}{dy} = -\frac{d}{dy}\left[\kappa^2\left(q_{C,y} + q_{D,y} + q_{R,y}\right)\right] \tag{11}$$

Species continuity:

$$\kappa^2 \rho v \frac{d\alpha_i}{dy} = -\frac{d}{dy}\left(\kappa^2 J_{i,y}\right) + \kappa^2 \dot{\omega}_i \tag{12}$$

where

$$a \equiv \left(\frac{du}{dx}\right)_{x=0} \tag{13}$$

$$\beta = \beta(y) = -\left(\frac{\partial^2 p}{\partial x^2}\right)_{x=0} \tag{14}$$

The foregoing conservation equations have been written in nondimensional form from the following set of dimensionless quantities:

$$\left.\begin{array}{lll}
x,y,r = \dfrac{x',y',r'}{R_b'} & K(x) = K'(x)R_b' & \kappa' = \kappa \\[2ex]
u,v,v_i = \dfrac{u',v',v_i'}{U_\infty'} & \rho = \dfrac{\rho'}{\rho_\infty'} & p = \dfrac{p'}{\rho_\infty'(U_\infty')^2} \\[2ex]
h,H = \dfrac{h',H'}{(U_\infty')^2} & q = \dfrac{q'}{\rho_\infty'(U_\infty')^3} & \dot{\omega}_i = \dfrac{\dot{\omega}_i' R_b'}{U_\infty'} \\[2ex]
J_i = \dfrac{J_i'}{\rho_\infty' U_\infty'} & \mu = \dfrac{\mu'}{\mu_s'} & k = \dfrac{k'}{k_s'} \\[2ex]
D_{12} = \dfrac{D_{12}'}{U_\infty' R_b'} & N_{Re} = \dfrac{\rho_\infty' U_\infty' R_b'}{\mu_s'} & N_{Pr} = \dfrac{c_p' \mu'}{k'}
\end{array}\right\} \tag{15}$$

where the subscripts ∞ and s refer to free-stream and shock conditions, respectively.

Restrictions and Assumptions

The governing stagnation-line equations are general equations and are restricted only by the requirements that $\rho_s/N_{Re} << 1$ and the net radiative heat fluxes in the x-direction are comparatively negligible. The following basic restrictions and assumptions are imposed on the governing equations:

(1) The gas is in local thermodynamic and chemical equilibrium.

(2) Diffusion of the chemical species is governed by a binary diffusion model.

(3) Radiative energy transport occurs within a one-dimensional, infinite, planar slab (tangent slab).

In order to uncouple the stagnation-line solution from the remaining subsonic field, it is necessary to assume the relationship between the shock and the body curvatures at $x = 0$. In the results of this analysis, the shock and body are assumed concentric unless otherwise specified. The results of Suttles' analysis for an inviscid, radiating flow field (ref. 31) indicate that the assumption is reasonable.

Preheating of the ambient air upstream of the shock wave due to radiation transport (precursor effects) is neglected. Smith (ref. 34), Hoshizaki and Lasher (ref. 8), and Rigdon et al. (refs. 12 and 27) indicate that precursor effects begin to become significant at velocities around 17 to 18 km/sec and above. Thus, the present solutions, which employ the Rankine-Hugoniot conditions (see Hayes and Probstein (ref. 35)) for the discontinuous jump conditions across the shock, will be restricted to velocities somewhat lower than this.

In the numerical solutions, unless otherwise specified, a Newtonian pressure distribution (ref. 35) is used to evaluate β, the term $\left(\frac{\partial^2 p}{\partial x^2}\right)_{x=0}$ in the x-momentum equation; that is, $\left(\frac{\partial^2 p}{\partial x^2}\right)_{x=0} = -2.0$. It should be noted that Wilson (ref. 14) used a value of -3.0, which leads to a thinner shock layer in his calculations.

The radiation-transport computer code which is used in the radiation computations is RATRAP, developed by Hoshizaki and Wilson (refs. 24 and 28 and appendix A of this paper). RATRAP considers most of the primary radiating chemical species associated with carbon, oxygen, nitrogen, and hydrogen mixtures. The calculations of the detailed thermodynamic and chemical compositions for chemical equilibrium are performed in the computer code FEMP, developed by Browne et al. (ref. 36). FEMP is included by Wilson as an integral part of RATRAP.

In the analysis, it is assumed that the transport properties for air developed by Hansen (ref. 11) apply for both air-to-air injection and injection of ablation products into air. This assumption for the ablation products will be superficially analyzed by perturbations in the pertinent transport property (Prandtl number) to determine its effect. It should be noted that Rigdon et al. (ref. 12) ran two identical cases with the exception of pure-air transport properties in one and the combined transport properties of ablation products and air in the other, and the resulting differences in the radiative heat fluxes to the wall were less than 1 percent.

The continuity and y-momentum equations (eqs. (8) and (10)) are unchanged when the foregoing assumptions are applied. The only perturbation in the x-momentum equation (eq. (9)) is the $\left(\frac{\partial^2 p}{\partial x^2}\right)_{x=0}$, or β, term arising from the Newtonian (or specified) pressure distribution in which $\left(\frac{\partial^2 p}{\partial x^2}\right)_{x=0}$ will be taken to be a constant in y in this analysis.

By applying the binary-diffusion and tangent-slab approximations, the heat-flux terms in the energy equation (eq. (11)) become:

$$q'_{C,y} + q'_{D,y} = -k' \frac{dT'}{dy'} \tag{16}$$

where k' is the "lumped" or "effective" conductivity computed and tabulated by Hansen (ref. 11) for air at temperatures up to 15 000 K and pressures up to 100 atmospheres (1 atm = 101 325 N/m^2).

The radiative-heat-flux equation for the heat flux at a point within a one-dimensional slab is given by Suttles (refs. 31 and 37) and is

$$q'_R(y') = 2\pi \int_0^\infty \left[\int_0^{y'} \alpha_\nu B_\nu E_2\left(\int_{\xi'}^{y'} \alpha_\nu \, d\epsilon' \right) d\xi' - \int_{y'}^{y'_s} \alpha_\nu B_\nu E_2\left(\int_{y'}^{\xi'} \alpha_\nu \, d\epsilon' \right) d\xi' \right] d\nu \tag{17}$$

where $E_2\left(\int_{\xi'}^{y'} \alpha_\nu \, d\epsilon' \right)$ is the exponential defined by

$$E_2(\zeta) = \int_0^1 e^{-\zeta/\mu} \, d\mu$$

and is described by Kourganoff (ref. 38). In equation (17), B_ν is the Planck function, ν is the frequency of radiation, and α_ν is the modified linear absorption coefficient which is a function of temperature, pressure, and the number densities of the chemical species within the slab. The equation is valid for a nongray self-absorbing gas. The absorption coefficients and radiative heat fluxes are computed in the radiation computer code RATRAP developed by Hoshizaki and Wilson (see Wilson (ref. 10)). The radiation model takes into account both continuum and atomic-line radiation exchange in a slab of nonuniform temperature. Details of the radiation model are given in appendix A.

The simplified energy equation can now be written as

$$\kappa^2 \rho' v' \frac{dH'}{dy'} = \frac{d}{dy'}\left(\kappa^2 k' \frac{dT'}{dy'} \right) - \frac{d}{dy'}\left(\kappa^2 q'_{R,y} \right) \tag{18}$$

where $q'_{R,y}$ is given by equation (17). The combined conduction-diffusion heat-flux term can be written in terms of total enthalpy from the following relations for static enthalpy, total enthalpy, and "effective" Prandtl number:

$$\left.\begin{aligned} dh' &= c'_p\, dT' \\ H' &= h' + \frac{(v')^2}{2} \end{aligned}\right\} \tag{19}$$

$$N_{Pr} = \frac{c'_p \mu'}{k'} \tag{20}$$

to yield

$$\kappa^2 \rho' v' \frac{dH'}{dy'} = \frac{d}{dy'}\left[\frac{\kappa^2 \mu'}{N_{Pr}}\left(\frac{dH'}{dy'} - v' \frac{dv'}{dy'}\right)\right] - \frac{d}{dy'}\left(\kappa^2 q'_{R,y}\right) \tag{21}$$

Upon applying the nondimensional relations defined in equations (15) and rearranging equation (21), the dimensionless energy equation becomes

$$\frac{1}{N_{Re}} \frac{d}{dy}\left(\frac{\kappa^2 \mu}{N_{Pr}} \frac{dH}{dy}\right) - \kappa^2 \rho v \frac{dH}{dy} = \frac{1}{N_{Re}} \frac{d}{dy}\left(\frac{\kappa^2 \mu}{N_{Pr}} v \frac{dv}{dy}\right) + \frac{d}{dy}\left(\kappa^2 q_{R,y}\right) \tag{22}$$

The species-continuity equation (12) undergoes considerable modification because of the assumptions of binary diffusion and equilibrium chemistry. The species-continuity equation was given by equation (12) as

$$\kappa^2 \rho v \frac{d\alpha_i}{dy} = -\frac{d}{dy}\left(\kappa^2 J_{i,y}\right) + \kappa^2 \dot{\omega}_i$$

Under the assumption of local chemical equilibrium, the volumetric rate of production of species i is indeterminate. However, the fact that the net rate of production of the mass fractions of the chemical elements is zero can be utilized to yield a tractable solution to the species-continuity equation. If it is assumed that the binary-diffusion law holds for the mass fractions, that is,

$$\bar{J}_i = -\rho D_{12} \frac{d\bar{\alpha}_i}{dy} \tag{23}$$

where the barred quantities refer to elemental mass fractions, the species-continuity and diffusion equations can be combined to yield the elemental-diffusion equation

$$\frac{d}{dy}\left(\kappa^2 \rho D_{12} \frac{d\bar{\alpha}_i}{dy}\right) - \kappa^2 \rho v \frac{d\bar{\alpha}_i}{dy} = 0 \tag{24}$$

The dimensional binary diffusion coefficient is given by Hirschfelder et al. (ref. 39) as

$$D'_{ij} = 0.002628 \left\{ \frac{\left[\dfrac{(T')^3 (M_i + M_j)}{2 M_i M_j}\right]^{1/2}}{p' \sigma'_{ij} \Omega_{ij}^{(1,1)^*}} \right\} \tag{25}$$

where

$$\sigma'_{ij} = \frac{1}{2}\left(\sigma'_i + \sigma'_j\right)$$

$$\Omega_{ij}^{(1,1)^*} = f\left(\frac{T'}{\epsilon'_{ij}/k^*}\right)$$

and

$$\left(\frac{\epsilon'_{ij}}{k^*}\right) = \left[\left(\frac{\epsilon'_1}{k^*}\right)\left(\frac{\epsilon'_2}{k^*}\right)\right]^{1/2}$$

The molecular constants σ'_i and ϵ'_i/k^* are tabulated by Svehla (ref. 40) and are given in table 1 for the chemical species of interest. The reduced collision integral $\Omega_{12}^{(1,1)^*}$ is based on the Lennard-Jones potential and is defined in reference 39 as a function of the nondimensional term T^*_{ij} which is given by

$$T^*_{ij} = \frac{T'}{\left(\epsilon'_{ij}/k^*\right)}$$

For the binary diffusion model, the individual elements of the ablation products and of the air which passes through the shock are considered to diffuse in the same respective manner as the two chemical species (one for the ablation products, the other for the air) used to form the binary diffusion coefficient. Thus, a distinction need not be made between the individual elements but only between the total mass fractions which represent the ablation products and the remaining mass fraction which represents the air products. Since the total mass fraction of all the elements (and, for that matter, the chemical species) must equal unity at any point, then one need solve only one elemental-diffusion equation, which is given by

$$\frac{d}{dy}\left(\kappa^2 \rho D_{12} \frac{d\bar{\alpha}_F}{dy}\right) - \kappa^2 \rho v \frac{d\bar{\alpha}_F}{dy} = 0 \tag{26}$$

where $\bar{\alpha}_F$ is the total mass fraction of the elements of the ablation products. The total mass fraction of the air products $\bar{\alpha}_A$ is then computed by

$$\bar{\alpha}_A = 1 - \bar{\alpha}_F \tag{27}$$

The mass fractions of the individual elements are then calculated by the equations

$$\overline{\alpha}_i = \overline{\alpha}_F \overline{\alpha}_{i,inj} + \overline{\alpha}_A \overline{\alpha}_{i,\infty} \qquad (i = 1, \ldots, M) \tag{28}$$

where $\overline{\alpha}_{i,inj}$ is the specified elemental mass fraction of the ith element of the ablation products injected at the wall and $\overline{\alpha}_{i,\infty}$ is the same ith element that passes through the shock layer. The density and the individual chemical species are then calculated from an equation of state by the free-energy-minimization subroutine FEMP (ref. 36) where

$$\left.\begin{aligned} \rho &= \rho\left(\overline{\alpha}_j, h, p\right) \\ \alpha_i &= \alpha_i\left(\overline{\alpha}_j, h, p\right) \end{aligned}\right\} \tag{29}$$

For analyses of the viscous, radiating stagnation-line flow, the resulting governing equations (8), (9), (10), (22), and (24) are the most general system of equations that are treated in the literature. These are the exact equations for the thin shock layer (for the tangent-slab and binary-diffusion assumptions) which are solved in this analysis for the stagnation line. As previously mentioned, Rigdon et al. (refs. 12 and 27) have applied initial-value techniques for the numerical solution to this system of equations (with the exceptions that they assume constant pressure across the shock layer and neglect the curvature terms) for the massive-blowing problem.

Transformed Equations

Before the solution technique is developed, it is desirable to transform the governing equations by a change in independent variable from y to η, where

$$\eta = \frac{1}{\hat{\delta}} \int_0^y \rho(y)dy \tag{30}$$

where $\hat{\delta}$ is the normalizing parameter given by

$$\hat{\delta} = \int_0^{y_s} \rho(y)dy$$

This transformation has the important effect of fixing the shock boundary at $\eta = 1$. The inclusion of density in the transformation gives, for a fixed nodal spacing in η, a finer resolution on a physical scale y at points near the body and within the boundary layer, where conditions are rapidly changing.

The transformed system of equations become:

Continuity:

$$\frac{d\left(\kappa^2 \rho v\right)}{d\eta} = 2\hat{\delta}\kappa a \tag{31}$$

x-momentum:

$$\frac{\kappa\rho}{N_{Re}\hat{\delta}^2}\frac{d}{d\eta}\left(\mu\rho\frac{da}{d\eta}\right) + \frac{\kappa\rho^2 v}{\hat{\delta}}\frac{da}{d\eta} - \rho a^2 + K\rho v a = -\beta \tag{32}$$

y-momentum:

$$\frac{dp}{d\eta} = -\rho v\frac{dv}{d\eta} \tag{33}$$

Energy:

$$\frac{d}{d\eta}\left(\frac{\kappa^2\rho\mu}{N_{Pr}}\frac{dH}{d\eta}\right) + \hat{\delta}N_{Re}\kappa^2\rho v\frac{dH}{d\eta} = \frac{d}{d\eta}\left(\frac{\kappa^2\mu}{N_{Pr}}\rho v\frac{dv}{d\eta}\right) + \hat{\delta}N_{Re}\frac{d}{d\eta}\left(\kappa^2 q_{R,\eta}\right) \tag{34}$$

Elemental diffusion:

$$\frac{d}{d\eta}\left(\kappa^2\rho^2 D_{12}\frac{d\bar{\alpha}_F}{d\eta}\right) + \hat{\delta}\kappa^2\rho v\frac{d\bar{\alpha}_F}{d\eta} = 0 \tag{35}$$

Equation of state:

$$\rho = \rho\left(\bar{\alpha}_i, h, p\right) \tag{36}$$

Note that the normal velocity v has been redefined as negative in the positive y- or η-direction in equations (31) to (36). This change in no way affects the solution to the equations since the boundary conditions, as will be discussed subsequently, have been appropriately modified to reflect this change. The flow-field coordinate system for the stagnation line in the transformed coordinates is shown in figure 2.

The transformed coordinate η is specified as zero at the body and as unity at the shock. The normalizing parameter $\hat{\delta}$ is an unknown in the problem and is obtained from the solution of the continuity equation (31):

$$\hat{\delta} = \frac{-\left(\kappa^2\rho v\right)_w + \left(\kappa^2\rho v\right)_s}{2\int_0^1 \kappa a\, d\eta} \tag{37}$$

Boundary Conditions

The subsonic flow field in the nose region is described by elliptic equations; consequently, the stagnation-streamline solution is influenced by the flow within the entire subsonic region. However, this influence only enters in the β term, that is, $-\left(\frac{\partial^2 p}{\partial x^2}\right)_{x=0}$ in the x-momentum equation (32), and in the curvature of the shock wave which provides the boundary condition for the tangential velocity gradient at the shock wave. For a shock wave and body which are concentric, the Rankine-Hugoniot relations yield the following relation between $\left(\frac{\partial^2 p}{\partial x^2}\right)_{x=0}$ and the velocity gradient a_s (see ref. 35):

$$\beta = -\left(\frac{\partial^2 p}{\partial x^2}\right)_{x=0} = 2\left(1 - \frac{1}{\rho_s}\right)a_s{}^2 \approx 2a_s{}^2 \tag{38}$$

Newtonian impact theory predicts (ref. 35)

$$\left(\frac{\partial^2 p}{\partial x^2}\right)_{x=0} = -2.0 \tag{39}$$

Thus,

$$a_s = \left(-\frac{1}{2}\frac{\partial^2 p}{\partial x^2}\right)^{1/2} = 1.0$$

With β and a_s specified, the stagnation-streamline problem becomes a two-point boundary-value problem, where conditions are specified at the shock wave and at the body. The boundary conditions necessary to solve the transformed conservation equations for the flow of a viscous, radiating gas with injection of foreign species, where the chemical species are in local thermodynamic equilibrium, are

At the body surface, or wall ($\eta = 0$, $y = 0$):

$$\left.\begin{aligned}
&a = a_w = 0\\
&\rho v = (\rho v)_w\\
&p = p_w \approx p_s + \frac{1}{2}\left(\rho v^2\right)_s\\
&H = H_w\\
&\bar{\alpha}_i = \bar{\alpha}_{i,inj} \ \left(\text{and} \ \ \bar{\alpha}_F = 1\right) \qquad\qquad (i = 1, \ldots, M \text{ elements})
\end{aligned}\right\} \tag{40}$$

where the boundary condition $\bar{\alpha}_F = 1$ applies for conditions of strong blowing.

At the shock wave ($\eta = 1$, $y = y_s$):

$$\left.\begin{aligned}
&a = a_s = 1.0\\
&\rho v = (\rho v)_s = 1.0\\
&p = p_s\\
&H = H_s = H_\infty\\
&\bar{\alpha}_i = \bar{\alpha}_{i,\infty} \ \left(\text{and} \ \ \bar{\alpha}_F = 0\right) \qquad\qquad (i = 1, \ldots, M \text{ elements})
\end{aligned}\right\} \tag{41}$$

where $\overline{\alpha}_{i,inj}$ is the mass fraction of element i which is injected at the wall, and $\overline{\alpha}_{i,\infty}$ is the mass fraction of element i which passes through the shock wave from the free stream. Conditions immediately behind the normal shock are computed from Rankine-Hugoniot relations. Heat fluxes entering the slab boundaries are assumed to be zero; that is, there is no precursor heating of the free stream by the shock layer and no radiation from the body into the shock layer.

Numerical Solution

The finite-difference approximations to the governing equations (31) to (36) and the procedure for the numerical solution to this system of equations are developed in this section. The equations are written in finite-difference form for a network of N equally spaced (in η) nodal points between the body ($n = 1$) and the shock ($n = N$), which are shown in figure 3. For most of the calculations, 21 nodal points are used. The overall numerical solution technique is iteration. Properties and parameters are assumed initially for each nodal point across the shock layer. The governing finite-difference equations are then solved sequentially, with the use of the most recent values of the profile parameters, until satisfactory convergence is obtained at each nodal point.

Finite-difference approximations.- Either two- or three-point finite-difference formulas are used to differentiate and integrate the governing differential equations numerically. Whenever possible, three-point central differences are employed since they are accurate (at a particular nodal point) to order $(\Delta\eta)^2$, where $\Delta\eta$ is the distance between points; whereas two-point differences are accurate only to order $\Delta\eta$. (See, e.g., ref. 30 or 41.) Two-point windward differences (with the flow) are employed for the convective terms in the elemental-diffusion and energy equations where dictated by stability requirements (i.e., profile solutions which are well behaved across the shock layer). The stability study of these two equations is presented in appendix B.

The finite-difference formulas that are employed to approximate the derivatives are given below. (See, e.g., ref. 30 or 41 for the development.) The formulas are valid for equally spaced increments in $\Delta\eta$. The central-difference formulas are

$$\left(\frac{df}{d\eta}\right)_n = \frac{-f_{n-1} + f_{n+1}}{2\,\Delta\eta} \tag{42a}$$

$$\left(\frac{d^2f}{d\eta^2}\right)_n = \frac{f_{n-1} - 2f_n + f_{n+1}}{(\Delta\eta)^2} \tag{42b}$$

$$\left[\frac{d}{d\eta}(cf)\right]_n = \frac{-c_nf_{n-1} - \left(c_{n-1} - c_{n+1}\right)f_n + c_nf_{n+1}}{2\,\Delta\eta} \tag{42c}$$

$$\left[\frac{d}{d\eta}\left(c\,\frac{df}{d\eta}\right)\right]_n = \frac{\left(c_{n-1} + c_n\right)f_{n-1} - \left(c_{n-1} + 2c_n + c_{n+1}\right)f_n + \left(c_n + c_{n+1}\right)f_{n+1}}{2(\Delta\eta)^2} \tag{42d}$$

where c and f are arbitrary functions. In the development of equation (42d), it was assumed that c varies linearly between nodal points.

The windward-difference formulas are either forward or backward differences, depending on the direction of the flow. If the mass flux ρv is positive (toward the body), forward differences are taken for the convective terms; if ρv is negative, backward differences are taken. The formulas are

If $(\rho v)_n > 0$,

$$\left(\rho v\,\frac{df}{d\eta}\right)_n = (\rho v)_n\,\frac{f_{n+1} - f_n}{\Delta\eta} \tag{43}$$

If $(\rho v)_n < 0$,

$$\left(\rho v\,\frac{df}{d\eta}\right)_n = (\rho v)_n\,\frac{f_n - f_{n-1}}{\Delta\eta} \tag{44}$$

Numerical integration is performed by the Simpson's rule approximation (ref. 41) using three points at a time along the profiles. The finite-difference equations used in performing the quadrature over the interval from η_n to η_{n+1} and over the full interval from η_n to η_{n+2} are

$$\left.\begin{aligned}&\int_{\eta_n}^{\eta_{n+1}} f(\eta)d\eta = \frac{\Delta\eta}{12}\left(5f_n + 8f_{n+1} - f_{n+2}\right)\\ &\text{and}\\ &\int_{\eta_n}^{\eta_{n+2}} f(\eta)d\eta = \frac{\Delta\eta}{3}\left(f_n + 4f_{n+1} + f_{n+2}\right)\end{aligned}\right\} \tag{45}$$

Initial profiles.- For the general case, the following profiles are initially assumed:

$$\rho v(\eta) = (\rho v)_w + \left[(\rho v)_s - (\rho v)_w\right]\eta^2 \tag{46a}$$

$$p(\eta) = p_s + \frac{1}{2}\left(\rho v^2\right)_s\left(1 - \eta^2\right) \tag{46b}$$

$$a(\eta) = a_s\eta \tag{46c}$$

$$h(\eta) = h_w + \left(h_s - h_w\right)\eta \tag{46d}$$

$$\overline{\alpha}_F(\eta) = \left(\overline{\alpha}_F\right)_w(1 - \eta) \tag{46e}$$

$$\rho(\eta) = \rho\left[\overline{\alpha}_i(\eta),p(\eta),h(\eta)\right] \tag{46f}$$

The density is computed in subroutine FEMP for a gas mixture in chemical equilibrium. All other quantities appearing on the right-hand side of the initial-profile equations are either available from the input boundary conditions or they are computed from Rankine-Hugoniot relations for the normal shock.

An initial value for the transformed shock displacement $\hat{\delta}$ is also required. The physical shock displacement distance for no blowing is correlated by Inouye (ref. 42) to be

$$\frac{y'_s}{R'_b} \approx 0.78 \frac{\rho'_\infty}{\rho'_s}$$

Since $\frac{y'_s}{R'_b} = \hat{\delta}\rho'_\infty \int_0^1 \frac{d\eta}{\rho'}$, then for a constant shock-layer density of ρ'_s,

$$\hat{\delta} \approx 0.78$$

For moderate blowing,

$$\hat{\delta} \approx 1 \tag{47}$$

which is the initial value assumed in this analysis.

This completes the statement of the problem of determining the initial profiles for the general case. The appropriate boundary conditions and initial profiles for special cases of interest, such as no blowing or air-to-air injection, are covered in the subsequent discussion of these special cases.

Solution procedure and finite-difference equations.- With the assumed initial profiles and parameters (eqs. (46) and (47)), the conservation equations are solved by successive iteration. The coupled equations are solved in the following sequence: continuity, y-momentum, elemental continuity, x-momentum, energy, and equation of state. The most recently computed values of the profile parameters and $\hat{\delta}$ are used in the computations. The density distribution is necessary to solve the governing differential equations. After these equations have been solved, updated values of density are computed from the equation of state and compared with the previous density values at each nodal point. The entire sequence through the governing equations is repeated with the new density distribution until two successive passes yield nearly identical (within 1 or 2 percent) density values at corresponding nodal points. The flow diagram which illustrates the solution procedure is shown in figure 4.

With the distribution for the tangential velocity gradient and the scale factor $\kappa(\eta)$, the continuity equation (31) is numerically integrated by Simpson's rule (eq. (45)) to give the updated shock displacement distance $\hat{\delta}$:

$$\hat{\delta} = \frac{-(\rho v)_w + \left(\kappa^2 \rho v\right)_s}{2\int_0^1 \kappa a \, d\eta} \tag{48}$$

and the mass-flux distribution $\rho v(\eta)$:

$$\kappa^2 \rho v(\eta) = 2\hat{\delta}\int_0^\eta \kappa a \, d\eta + (\rho v)_w \tag{49}$$

The velocity profile, which is required in the solution of the y-momentum equation, is computed from the previous density distribution $\rho(\eta)$ and the updated mass-flux distribution $\rho v(\eta)$, namely,

$$v(\eta) = \frac{\rho v(\eta)}{\rho(\eta)} \tag{50}$$

The y-momentum equation (33) is numerically integrated by Simpson's rule (eq. (45)) to give the pressure distribution $p(\eta)$:

$$p(\eta) = \int_\eta^1 \rho v \frac{dv}{d\eta} \, d\eta + p_s \tag{51}$$

The profiles of $\rho v(\eta)$ and $v(\eta)$ are tabulated from the continuity-equation solution, and a central-difference numerical differentiation scheme (eq. (42a)) gives $\frac{dv(\eta)}{d\eta}$ at the $N - 2$ points within the shock layer. The values of $\frac{dv(\eta)}{d\eta}$ at the body and the shock boundaries are obtained from two-point forward- and backward-difference approximations, respectively.

The elemental-diffusion equation (35) is cast in finite-difference form by using the central-difference formula (eq. (42d)) for the second-derivative diffusion term and the windward-difference equations (eqs. (43) and (44)) for the first-derivative convective term. The resulting equations are

For $n = 1$,

$$\left(\overline{\alpha}_F\right)_1 = 1 \tag{52a}$$

For $n = 2, \ldots, N - 1$,

$$\left[\left(\kappa^2\rho^2 D_{12}\right)_{n-1} + \left(\kappa^2\rho^2 D_{12}\right)_n - 2\hat{\delta}(\Delta\eta)\left(\kappa^2\rho v\right)_n(1 - S)\right]\left(\overline{\alpha}_F\right)_{n-1} - \left[\left(\kappa^2\rho^2 D_{12}\right)_{n-1}\right.$$

$$\left. + 2\left(\kappa^2\rho^2 D_{12}\right)_n + \left(\kappa^2\rho^2 D_{12}\right)_{n+1} + 2\hat{\delta}(\Delta\eta)\left(\kappa^2\rho v\right)_n(1 - 2S)\right]\left(\overline{\alpha}_F\right)_n$$

$$+ \left[\left(\kappa^2\rho^2 D_{12}\right)_n + \left(\kappa^2\rho^2 D_{12}\right)_{n+1} + 2\hat{\delta}(\Delta\eta)\left(\kappa^2\rho v\right)_n S\right]\left(\overline{\alpha}_F\right)_{n+1} = 0 \tag{52b}$$

For $n = N$,

$$\left(\overline{\alpha}_F\right)_N = 0 \tag{52c}$$

where

$$S = 0 \quad \text{if} \quad (\rho v)_n < 0$$

and

$$S = 1 \quad \text{if} \quad (\rho v)_n \geqq 0$$

The formulation results in a banded (tridiagonal) matrix equation of the form

$$\begin{bmatrix} B_1 & C_1 & 0 & & \cdots & & 0 \\ A_2 & B_2 & C_2 & & \cdots & & 0 \\ 0 & A_3 & B_3 & C_3 & \cdots & & 0 \\ \vdots & & & & & & \\ 0 & \cdots & & A_{N-1} & & B_{N-1} & C_{N-1} \\ 0 & \cdots & & 0 & & A_N & B_N \end{bmatrix} \begin{bmatrix} \left(\overline{\alpha}_F\right)_1 \\ \left(\overline{\alpha}_F\right)_2 \\ \left(\overline{\alpha}_F\right)_3 \\ \vdots \\ \left(\overline{\alpha}_F\right)_{N-1} \\ \left(\overline{\alpha}_F\right)_N \end{bmatrix} = \begin{bmatrix} D_1 \\ D_2 \\ D_3 \\ \vdots \\ D_{N-1} \\ D_N \end{bmatrix} \tag{53}$$

where A_n, B_n, and C_n are the coefficients of the $\left(\overline{\alpha}_F\right)_{n-1}$, $\left(\overline{\alpha}_F\right)_n$, and $\left(\overline{\alpha}_F\right)_{n+1}$ terms, respectively, and D_n are the terms appearing on the right-hand side in equations (52). At the wall boundary $n = 1$, the coefficients are $B_1 = 1$, $C_1 = 0$, and $D_1 = 1$. At the shock boundary $n = N$, the coefficients are $A_N = 0$, $B_N = 1$, and $D_N = 0$. The system of equations is easily solved by Potters' method, which is a form of Gaussian elimination that is efficient for solving a banded matrix system of equations. (See refs. 43 and 30.) The solution to equations (52) yields the distribution of the total mass fraction of the ablation products at N nodal points subject to the constraint that $0 \leqq \left(\overline{\alpha}_F\right)_n \leqq 1$. This constraint was imposed only during the intermediate iterations and was not necessary for the final solution. The mass fractions of the individual air and ablation-product elements are then computed from equations (27) and (28).

The transport properties μ and N_{Pr} required in the solutions to the x-momentum and energy equations are obtained from a tabular lookup as functions of the temperature, calculated in the FEMP subroutine, and the pressure, obtained in the solution of the y-momentum equation.

The x-momentum equation (32) is next solved. The equation is cast in finite-difference form by using the central-difference expressions given in equations (42) to approximate the first- and second-order derivatives. Since the equation is nonlinear in the velocity gradient a, an iterative procedure is required for its solution. A quasi-linearization approach (see ref. 44) is employed to generate the solution by a rapidly converging iteration.

The x-momentum equation is quasi-linearized by the following technique: At a given nodal point, let

$$\begin{aligned}\left[a^{(i)}\right]^2 &= \left[a^{(i-1)} + a^{(i)} - a^{(i-1)}\right]^2 \\ &= 2a^{(i-1)}a^{(i)} - \left[a^{(i-1)}\right]^2 + \left[a^{(i)} - a^{(i-1)}\right]^2 \qquad (54)\end{aligned}$$

where the superscripts i and i-1 refer to the values of $a(\eta)$ at the iterations i and i-1, respectively. Upon assuming that

$$\lim_{i\to\infty}\left[a^{(i)} - a^{(i-1)}\right]^2 \to 0 \qquad (55)$$

and x-momentum equation becomes linear in $a^{(i)}(\eta)$, where

$$\left[a^{(i)}\right]^2 \approx 2a^{(i-1)}a^{(i)} - \left[a^{(i-1)}\right]^2 \quad \text{as} \quad i \to \infty \qquad (56)$$

Combining the finite-difference formulas for the derivatives (eqs. (42)) with equation (56) yields the finite-difference form of the x-momentum equation:

For $n = 1$,

$$a_1^{(i)} = 0 \tag{57a}$$

For $n = 2, \ldots, N - 1$,

$$\begin{aligned}
&\left\{\frac{\left(\kappa\rho^2 v\right)_n}{2\hat{\delta}(\Delta\eta)} - \frac{(\kappa\rho)_n\left[(\rho\mu)_{n-1} + (\rho\mu)_n\right]}{2\hat{\delta}^2 N_{Re}(\Delta\eta)^2}\right\} a_{n-1}^{(i)} + \left\{2\left[\rho a^{(i-1)}\right]_n\right. \\
&\quad \left. - (\kappa\rho v)_n + \frac{(\kappa\rho)_n\left[(\rho\mu)_{n-1} + 2(\rho\mu)_n + (\rho\mu)_{n+1}\right]}{2\hat{\delta}^2 N_{Re}(\Delta\eta)^2}\right\} a_n^{(i)} \\
&\quad - \left\{\frac{\left(\kappa\rho^2 v\right)_n}{2\hat{\delta}(\Delta\eta)} + \frac{(\kappa\rho)_n\left[(\rho\mu)_n + (\rho\mu)_{n+1}\right]}{2\hat{\delta}^2 N_{Re}(\Delta\eta)^2}\right\} a_{n+1}^{(i)} = \beta + \left\{\rho\left[a^{(i-1)}\right]^2\right\}_n
\end{aligned} \tag{57b}$$

For $n = N$,

$$a_N^{(i)} = a_s \tag{57c}$$

The subscript n refers to the nth nodal point in the shock layer and the superscript i refers to the ith iterative value of a.

For a linear iteration on the velocity gradient a, let

$$a_n^{(i)} = a_n^{(i-1)} + \epsilon_n \tag{58}$$

where ϵ_n is the error in the ith iteration at the nth nodal point. Substituting equation (58) for $a_n^{(i)}$ into equation (57b) yields a system of equations of the form

$$A_n\epsilon_{n-1} + B_n\epsilon_n + C_n\epsilon_{n+1} = \overline{D}_n \qquad (n = 2, \ldots, N - 1) \tag{59}$$

where A_n, B_n, and C_n are the coefficients of the terms $a_{n-1}^{(i)}$, $a_n^{(i)}$, and $a_{n+1}^{(i)}$, respectively, of equation (57b) for $n = 2, \ldots, N - 1$. The term $\overline{D}_n$ is given by

$$\overline{D}_n = \beta + \left\{\rho\left[a^{(i-1)}\right]^2\right\}_n - A_n a_{n-1}^{(i-1)} - B_n a_n^{(i-1)} - C_n a_{n+1}^{(i-1)} \tag{60}$$

for $n = 2, \ldots, N - 1$. Since the boundary conditions are specified at the body and at the shock, then the equations at the boundaries become

$$\left.\begin{aligned} &\epsilon_1 = 0 &&(\text{or } A_1 = C_1 = D_1 = 0 \text{ and } B_1 = 1) \\ &\epsilon_N = 0 &&(\text{or } A_N = C_N = D_N = 0 \text{ and } B_N = 1) \end{aligned}\right\} \tag{61}$$

The system of equations (59) and (61) may be written as a tridiagonal matrix equation, which is solved by Potters' method. The velocity gradient a_n is updated by equation (58) and the process repeated until

$$\left|\epsilon_n\right| \leqq \tau \qquad (\text{all } n)$$

In this study, this assigned convergence interval τ is 0.01.

The total-enthalpy distribution is obtained from the tridiagonal-matrix solution to the energy equation (34) in a single pass. As previously discussed, the total-enthalpy derivative for the combined convective and diffusive heat-flux terms is included explicitly in the matrix solution for the H_n terms, whereas the radiative-flux term is computed by using the enthalpy profile of the previous iteration and the updated profiles of pressure and elemental mass fraction from the solutions for the y-momentum and species-diffusion equations, respectively. Consistent with the treatment of the elemental-diffusion equation, the windward-difference equations (eqs. (43) and (44)) are used to approximate the convective term in the energy equation. Three-point central-difference formulas are applied to the remaining derivatives to yield the following finite-difference form of the energy equation:

For $n = 1$,

$$H_1 = H_w \tag{62a}$$

For $n = 2, \ldots, N - 1$,

$$\begin{aligned} &\left\{\frac{1}{2(\Delta\eta)^2}\left[\left(\frac{\kappa^2\rho\mu}{N_{Pr}}\right)_{n-1} + \left(\frac{\kappa^2\rho\mu}{N_{Pr}}\right)_n\right] - \frac{\hat{\delta}N_{Re}}{\Delta\eta}\left(\kappa^2\rho v\right)_n(1 - S)\right\} H_{n-1} - \left\{\frac{1}{2(\Delta\eta)^2}\left[\left(\frac{\kappa^2\rho\mu}{N_{Pr}}\right)_{n-1}\right.\right. \\ &\left.\left. + 2\left(\frac{\kappa^2\rho\mu}{N_{Pr}}\right)_n + \left(\frac{\kappa^2\rho\mu}{N_{Pr}}\right)_{n+1}\right] - \frac{\hat{\delta}N_{Re}}{\Delta\eta}\left(\kappa^2\rho\mu\right)_n(1 - 2S)\right\} H_n + \left\{\frac{1}{2(\Delta\eta)^2}\left[\left(\frac{\kappa^2\rho\mu}{N_{Pr}}\right)_n + \left(\frac{\kappa^2\rho\mu}{N_{Pr}}\right)_{n+1}\right]\right. \\ &\left. + \frac{\hat{\delta}N_{Re}}{\Delta\eta}\left(\kappa^2\rho v\right)_n S\right\} H_{n+1} = \left[\frac{d}{d\eta}\left(\frac{\kappa^2\mu}{N_{Pr}}\,\rho v\,\frac{dv}{d\eta}\right)\right]_n + \hat{\delta}N_{Re}\left[\frac{d}{d\eta}\left(\kappa^2 q_{R,\eta}\right)\right]_n \end{aligned} \tag{62b}$$

For $n = N$,

$$H_N = H_\infty \tag{62c}$$

where

$$S = 0 \quad \text{if} \quad (\rho v)_n < 0$$

and

$$S = 1 \quad \text{if} \quad (\rho v)_n \geqq 0$$

The derivative terms appearing on the right-hand side of equation (62b) are evaluated by the central-differences formulas (eqs. (42)).

The density distribution which was required in the solution to the governing differential equations can now be updated by the equation of state

$$\rho_n = \rho_n\left[\left(\overline{\alpha}_i\right)_n, p_n, h_n\right] \tag{63}$$

at each nodal point. The updated values of ρ_n provide the mechanism for iterating the governing equations. Upon setting ρ_n equal to either the newly computed values $\rho_n^{(i)}$ or some fraction of the old values of density $\rho_n^{(i-1)}$ plus some fraction of the new values $\rho_n^{(i)}$ (in order to speed convergence of the flow-field solution), the entire procedure, beginning with the continuity equation, can be repeated until

$$\frac{\left|\rho_n^{(i)} - \rho_n^{(i-1)}\right|}{\rho_n^{(i)}} \leqq \epsilon \qquad (\text{all} \quad n) \tag{64}$$

The interval of convergence ϵ used in this analysis is 0.02 or less.

Salient features of the implicit finite-difference algorithm.- The implicit-finite difference algorithm developed in the previous section is quite simple, yet sufficiently flexible to treat the problem of viscous, radiating shock layers.

With the two- and three-point difference approximations for equally spaced increments, the governing equations for the thin shock layer can be made amenable to numerical solution without making unduly restrictive assumptions for the purpose of yielding analytically-tractable solutions. The tridiagonal-matrix system of equations which results can be efficiently solved by Potters' method, which requires only about 3n computations, as contrasted with the $(n)^2$ computations required for inversion of a full matrix.

Simple linear and quadratic profiles can be initially assumed as functions of the boundary conditions. Or, one may take advantage of prior knowledge of the solution behavior and begin with improved estimates of the profile parameters (i.e., read in the parameter values at each nodal point).

No singularities appear in the governing finite-difference equations since division by ρv is not required in the present formulation of the problem. In the region where ρv (or v) approaches zero, the diffusion terms become important in the elemental-diffusion equation (eqs. (52)). Likewise, the viscous terms predominate in the x-momentum and energy equations (eqs. (57) and (62)) near $\rho v = 0$.

The method is an implicit scheme in which the unknown quantities at point n are calculated as functions of conditions at surrounding points as well as conditions at the point itself. This is in contrast with explicit schemes in which the unknown quantities at a point are evaluated solely as a function of conditions at a former point (such as the function and its derivative being evaluated at the (n-1)th point and then extrapolated to the nth point to determine the unknown function). For a given step size, implicit schemes are generally stable (bounded), whereas explicit schemes may or may not be stable.

In the present approach to the two-point boundary-value problem, the boundary conditions are specified at the shock wave and at the body. Since the matrix system of equations (for a particular governing equation) is completely coupled across the entire shock layer (e.g., note the appearance of $\left(\overline{\alpha}_F\right)_n$ in the (n-1)th, nth, and (n+1)th elemental-diffusion equations (eqs. (52)) and the known boundary conditions are included in the system of equations, then the computed distributions between each endpoint are bounded and are monotonic in behavior (with the exception of the pressure, which reaches a maximum at the stagnation point). Thus, the analyst has near-maximum information about the behavior and levels of the unknowns which are to be computed as well as a high degree of assurance that the computer run will not be aborted because of overflow (numbers larger than the computer will accept).

Perhaps one of the biggest advantages of the present approach over initial-value methods resides in the fact that only a limited number of unknown quantities need to be evaluated in order, first, to satisfy the governing differential equations and, second, to provide the necessary inputs for the radiative-flux computations. In the present method, the only unknowns are the properties themselves (ρv, p, etc.) at each nodal point about which one has maximum information as to the bounds on the values and the general behavior of the properties across the shock layer. In contrast, consider the computations which must be performed in an initial-value treatment of the problem (such as Runge-Kutta forward integration). In the initial-value approach for the solution of a single governing equation, the unknown property and also its derivative must be computed. Generally, little information is available as to the behavior of the derivative across the shock layer. As a consequence, the function or derivative changes from point to point are generally closely controlled, by restricting the step size, to maintain stability as the calculations proceed downstream.

RESULTS AND DISCUSSION

In this section the numerical results obtained from the solution to the governing equations developed in the previous section are presented and discussed. The solutions which were obtained in the various phases in the development of the method are presented in the sequence of their development, beginning with the constant-density solutions and continuing through the solutions for the viscous, radiating shock layer with injection of ablation products included. Results are compared with results from existing approaches to the solution of the equations for the radiating flow field.

All numerical solutions were generated on a Control Data Corporation 6600 digital computer.

Constant-Density Solutions

The results of the constant-density study are presented in this section. The convergence behavior of the solution for the reduced system of equations that describe the flow of a constant-density gas is examined. Selected solutions are shown for inviscid and viscous flows. Results are presented for a range of blowing rates and Reynolds numbers.

The overall solution to the governing equations is by iteration until satisfactory convergence is obtained on the density. For a constant-density assumption (and a viscosity and Reynolds number specification required for the viscous-flow solution), the continuity, x-momentum, and y-momentum equations can be solved independently of the energy and diffusion equations. Naturally, the density is not iterated; however, the remaining system of equations (continuity and x- and y-momentum) are still coupled, and in the present approach, an iterative scheme is required for their solution, as indicated by figure 4. The equations are solved "one at a time" by a method of successive approximations until the computed values of ρv, a, and p for two consecutive iterations are within a specified accuracy at each nodal point. The constant-density solutions thus serve a twofold purpose. First, the solutions provide a fundamental means of studying the convergence behavior of the coupled system of equations for a wide variety of blowing rates and Reynolds numbers and thus permit an assessment of the adequacy of the successive-approximation iterative scheme. Second, the solutions provide an indication as to the nodal-spacing requirements for the formulation of the implicit finite-difference equations.

Several cases were run for a range of typical blowing rates $\left((\rho v)_w = 0 \text{ to } -0.2\right)$, Reynolds numbers $\left(N_{Re} = 1 \text{ to } 10^5\right)$, and nodal spacings (N = 11 to 101) for a constant density of 20 and a viscosity of 1.0. All solutions required about three or four iterations and a total computer time of 2 to 4 seconds. No discernible differences were observed in the computed profiles of ρv, p, and a or the values of $\hat{\delta}$ for $N = 11$ and $N = 101$.

It was observed that the computer times were a function of the number of nodal points (the 2- and 4-second run times were for $N = 11$ and $N = 101$, respectively), and increasing the blowing rate or Reynolds number had little or no effect on the computer run times.

The convergence behavior of a typical constant-density solution is shown in figure 5, where the successive solutions to the continuity and x-momentum equations are plotted. The solution is for a constant density of 20, a constant viscosity of 1.0, a typical Reynolds number of 10^5, and a blowing rate at the wall of -0.2. Twenty-one nodal points were used in the computations. Initial linear profiles for $\rho v(\eta)$ were assumed. The accuracy criteria were that the computed values of $\rho v(\eta)$, $p(\eta)$, and $a(\eta)$ for two consecutive iterations be within 0.01 at each nodal point $\left(\text{e.g.}, \left|(\rho v)_n^{(i)} - (\rho v)_n^{(i-1)}\right| \leqq 0.01 \text{ for all } n\right)$. These accuracy criteria were maintained throughout the entire course of the present study of viscous, radiating flows. As indicated by the key in figure 5, the solution converged in four iterations which required about 3 seconds of computer time.

Three constant-density solutions for no blowing are shown in figure 6: an inviscid case and two viscous cases for Reynolds numbers of 1 and 10^5. The case for $N_{Re} = 10^5$ is typical of the Reynolds number of interest, whereas the case for $N_{Re} = 1$ is actually outside the limits of applicability of the thin-shock-layer equations and is shown merely to demonstrate that the present approach yields solutions over the entire range of Reynolds numbers.

The effect of the boundary layer and its extent can be seen in figure 6(a). For inviscid flow, there is no boundary layer and a nonzero velocity gradient exists at the wall. This gradient, from equation (32), is given by $a_1 = \sqrt{\beta/\rho_1}$. For $N_{Re} = 10^5$, most of the shock layer is inviscid with only a thin boundary layer present near the wall (to $\eta \approx 0.03$), where the velocity gradient slope in y (i.e., $da/d\eta$) is a maximum; whereas for $N_{Re} = 1$, the entire shock layer is viscous and no abrupt changes in $da/d\eta$ are observed. The plot in figure 6(b) indicates that there is little difference in the mass-flux distributions for the inviscid case and for the viscous case with $N_{Re} = 10^5$. Also shown in the figure are the transformed shock-layer thicknesses $\hat{\delta}$ for the three cases. In the inviscid case, the stagnation-line analysis yielded a value for $\hat{\delta}$ of 0.796, which is close to the value correlated by Inouye ($\hat{\delta} = 0.78$) from inviscid analyses for the entire subsonic flow field surrounding a spherical body (ref. 42). For $N_{Re} = 10^5$, the transformed shock-layer thickness $\hat{\delta}$ is about 3 percent greater than that for the inviscid case, whereas for $N_{Re} = 1$, $\hat{\delta}$ increased about 33 percent.

The influence of the blowing rate on the velocity gradient and the shock-layer thickness y_s for a constant density is shown in figure 7 where a is plotted in the physical coordinate system. The figure indicates that the inner flow region from the body to the stagnation point $\left(y_s - (y)_{\rho v=0} \approx 0.041\right)$ is drastically modified as a result of blowing but that the inviscid outer flow is virtually unaffected by the blowing rate. For the constant-density model, the shock wave simply moves outward from the body as the blowing rate increases, while the character of the inviscid outer flow is independent of the blowing rate.

The constant-density results demonstrate that for a wide range of blowing rates and Reynolds numbers, the solution to the flow equations converges in a minimum number of iterations, the nodal-spacing requirements are indeed moderate, and the computational times are reasonably short. With this information, the behavior of the overall solution with the variable-density iteration can now be examined.

Nonradiating Air Solutions

The overall convergence of the flow solution for a variable density is examined in this section for equilibrium air without radiation. Solutions for both nonblowing and the blowing of air into air are presented. The air model consists of elemental mass fractions of 0.78 nitrogen and 0.22 oxygen.

The development of stability criteria is difficult even for the simplest of equations. For the coupled system of nonlinear equations which are solved in this study, it becomes necessary to rely on the experimental data obtained from the numerical solution in order to obtain information about the overall stability and convergence behavior of the solution. The results of the information are reflected in the logic presented in the flow diagram for the overall solution procedure shown in figure 4. It should be emphasized that figure 4 represents the results of the experimental stability study which is used in all subsequent studies. The numerical results which led to this particular iterative procedure for the variable-density solutions are discussed below. The solutions are for a nose radius R_b' of 3.43 m and the following free-stream conditions unless otherwise noted:

$$U_\infty' = 14.6 \text{ km/sec}$$

$$p_\infty' = 1.6 \times 10^{-4} \text{ atm}$$

$$\rho_\infty' = 2.38 \times 10^{-7} \text{ g/cm}^3$$

It was observed in the numerical solution that major oscillations occurred in the enthalpy and the density, particularly in the viscous region of the flow, as the iterative procedure progressed in time. These enthalpy oscillations are shown in figure 8, which is a plot of the calculated enthalpies at the first three nodal points adjacent to the wall and within the shock layer (note that $H_1 = H_w = 0.1$ and is constant) versus iteration number, where one iteration represents one complete pass through the governing equations. From the figure it can be seen that the amplitudes of the oscillations generally decrease with η, and although it is not shown here, it was observed that after about five iterations the enthalpy values had converged beyond $\eta \approx 0.3$. However, the solutions near the wall did not converge but merely continued to oscillate even after 30 iterations.

The density profiles exhibited an oscillatory behavior similar to that of the enthalpy profiles but in an inverse fashion (i.e., an overprediction of the enthalpy led to an underprediction of the density). This is because there is a strong inverse coupling between the density and the enthalpy in the equation of state. The equation of state for air has been correlated by G. Louis Smith (ref. 45) in the form $p \propto \rho^a h^b$, where a and b are positive exponents. Since p is nearly constant, then an overprediction of the enthalpy obtained in the energy equation is a corresponding underprediction of the density from the equation of state and vice versa. It is possible to get into a resonant computing mode in which the density and the enthalpy oscillate back and forth and can be slowly convergent or even divergent.

From the results it was not clear that the solution was divergent; however, it was apparent that if it was converging near the wall, it was prohibitively slow.

Since the calculations appear to be oscillating about the solution, then by proper damping of the calculated quantities it is possible to speed convergence. Fox (ref. 46) has discussed the method of underrelaxation, whereby the quantities which are highly oscillatory are weighted, or damped, before they are used in subsequent calculations. It was found that by weighting the static enthalpy and the density profiles by a certain percentage of their former values and their newly calculated values, rapid convergence of the overall solution could be obtained. The weighted values of the static enthalpy and the density at each nodal point are computed from the following relations:

$$h_n = d_h h_n^{(i-1)} + \left(1 - d_h\right) h_n^{(i)}$$

and

$$\rho_n = d_\rho \rho_n^{(i-1)} + \left(1 - d_\rho\right) \rho_n^{(i)}$$

The convergence behavior of the solution for damping factors of 0.5 and 0.9 is shown in figure 9. Plotted in this figure are the total enthalpy and density values computed at nodal point 2. Both solutions converged; however, it is apparent that while overdamping will insure convergence of an otherwise oscillatory solution, it can be unduly time consuming. For damping factors around 0.2 to 0.3, certain solutions would converge but required more iterations than for damping factors of 0.5. For most of the cases examined, both with and without blowing, the damping factors of 0.5 appeared to be near optimum in terms of generating a converged solution in a minimum number of iterations. It was also observed that for the largest blowing rate (-0.2) considered in this analysis, damping factors of 0.7 speeded convergence of the solution by about a factor of 2 over the convergence time for damping factors of 0.5. Because of the sensitivity of the computer run times to the damping factors, and since no attempt was made in the present study to optimize the damping factors for a particular solution beyond that which was just discussed, subsequent discussions of computer time relate closely to damping factors of 0.5. With a thorough study of damping-factor requirements for optimum solutions, run times may be improved significantly.

In order to obtain an indication of the stability of the variable-density solution for various blowing rates, three blowing rates, 0, -0.1, and -0.2, were examined. The same free-stream conditions given previously and a wall enthalpy value of 0.1 were specified. Twenty-one nodal points were used across the shock layer. All solutions converged to an absolute density accuracy of 0.01 for damping factors of 0.5. It was observed that the number of iterations of the governing equations, and consequently the run times, increased with increasing blowing rate. For $(\rho v)_w = 0$, -0.1, and -0.2, the number of iterations required to obtain convergence were 11, 16, and 21, respectively, and the corresponding computer times were 1.5, 2.5, and 3.5 minutes, respectively. The computer run times are well within reason for computations of the fully viscous shock layer with equilibrium-air chemistry.

The results obtained for $(\rho v)_w = 0$ and -0.1 are shown in figure 10. On a physical scale the boundary layer for $(\rho v)_w = 0$ occupies about 5 percent of the shock layer, and the combined inner layer and boundary layer for $(\rho v)_w = -0.1$ occupies about 20 percent. The results for $(\rho v)_w = -0.2$ are not shown in the figure. The solution for $(\rho v)_w = -0.2$ converged; however, in the inviscid outer region the enthalpy profiles were extremely irregular when a central-difference form of the convective term in the energy equation was used. Enthalpy values ranging from 0.45 up to about 0.7 (the latter value being greater than the free-stream total enthalpy) were observed. To a similar degree, irregularities in the density profile and minor inconsistencies in the velocity-gradient profile were observed.

It was observed much later in the study, when the solution to the elemental-diffusion equation was required for the study of ablation-products injection, that the energy equation and the elemental-diffusion equations are similar and have coefficients on the derivative terms which under further dimensional analysis reduce to about the same order of magnitude. As discussed in appendix B, the elemental-diffusion equation can be unstable unless the nodal spacing is made prohibitively small $\left(\Delta\eta \approx 10^{-4}\right)$, and a windward-difference formulation is required to obtain meaningful $\bar{\alpha}_i$ profiles. As a consequence of the stability study of the elemental-diffusion equation, a windward-difference form of the energy equation was also used for the radiating cases.

Radiating Air Solutions

The solutions for the viscous, radiating shock layer, including air-to-air injection, are discussed in this section. The present results are compared with results from existing approaches.

General results from the present analysis.- The results obtained for $(\rho v)_w = 0$, -0.1, and -0.2 are shown in figure 11 for a nose radius of 3.048 m and the following free-stream conditions:

$$U'_\infty = 15.25 \text{ km/sec}$$

$$\rho'_\infty = 2.72 \times 10^{-7} \text{ g/cm}^3$$

$$p'_\infty = 1.95 \times 10^{-4} \text{ atm}$$

A wall enthalpy of 0.028, which corresponds to a wall temperature of 3600 K, was specified. This temperature is close to the steady-state ablation temperature predicted by Smith et al. (ref. 13). Twenty-one nodal points were used for all computations except the radiative-flux computations, where 11 points were used to avoid excessive computer time. The intermediate values of the radiative heat fluxes required in the solution of the energy equation were obtained by linear interpolation. Typical total computer times ranged from about 30 minutes for the solution of the problem without blowing to about 70 minutes for the problem with a blowing rate $(\rho v)_w$ of -0.2.

A comparison of the radiating solutions shown in figure 11(a) with the nonradiating solutions shown in figure 10(a) for slightly different free-stream and wall enthalpies shows that the physical shock-displacement distance significantly decreases when radiation is taken into account. However, the mass-flux distributions were only slightly altered in the η-coordinate system. The significant decrease in y_s when radiation is included is due largely to the nonadiabatic effects in the outer inviscid region which result in higher values of density (by almost a factor of 2 as shown by comparing figures 10(e) and 11(e)) and, to a somewhat lesser extent, the adjustment of the inner flow to the wall boundary conditions. On a physical scale the outer inviscid region occupies about 95, 75, and 60 percent of the total shock layer for blowing rates of 0, -0.1, and -0.2, respectively.

The radiative heat-flux distributions across the shock layer are shown in figure 11(f). Positive heat-flux values indicate net radiative heat transfer away from the body; negative values indicate net transfer toward the body. The nondimensional heat fluxes at the wall are -0.0434 for $(\rho v)_w = 0$, -0.0390 for $(\rho v)_w = -0.1$, and -0.0369 for $(\rho v)_w = -0.2$. These values correspond to dimensional values $q'_{R,w}$ of -4150, -3740, and -3490 watts/cm^2, respectively. Thus for air-to-air injection at $(\rho v)_w = -0.1$ and -0.2, the radiative heating rates are reduced 10 and 16 percent, respectively, below the rates for no blowing. The absolute values of heat flux for both blowing rates decrease slightly in the inner region in the direction of the body; however, the results indicate that the inner air layer is only moderately effective in absorbing the incident radiation from the high-temperature outer layer.

It is observed in figure 11(f) that the radiative heat fluxes reach a minimum near the stagnation point, which is expected on the basis of an examination of the governing differential equations. Note that if the flow is inviscid, the minimum in the radiative heat flux occurs exactly at the stagnation point. This feature provides an important self-test of the overall accuracy of the present method, that is, the ability of the method to generate thermodynamic properties which, as inputs in the computations of radiative heat flux, are sufficiently accurate to yield the minimum in the fluxes near the stagnation point.

More interesting and important checks on the adequacy of the present method for the stagnation-line solution can be made by comparison with solutions to the entire subsonic flow field and by comparison with existing stagnation-line solutions. The first exercise serves not only as a check on the accuracy of the solution but also as a check of the fundamental assumption that the stagnation-line solution can be decoupled from the entire region of influence.

Comparisons of no-blowing results with existing solutions.- Shown in figure 12 is a comparison of the enthalpy profiles generated in the present approach with the stagnation-line enthalpy profiles obtained by Suttles (ref. 31) from a solution by a one-strip method of integral relations and with those obtained by Falanga and Sullivan (ref. 47) from an inverse-method solution.

The solutions are for no blowing, a nose radius of 3.427 meters, and the following free-stream conditions:

$$U'_\infty = 14.55 \text{ km/sec}$$

$$\rho'_\infty = 2.377 \times 10^{-7} \text{ g/cm}^3$$

$$p'_\infty = 1.6 \times 10^{-4} \text{ atm}$$

Both of the reference solutions are extracted from complete solutions to the entire radiating subsonic flow field. The present solution is for viscous flow, whereas the reference cases are for inviscid flows; however, the comparisons are still meaningful since for no blowing the boundary layer occupies only a small percentage of the shock layer. The RATRAP computer code (ref. 10) was used in all three studies. The enthalpy profile from the present solution compares favorably with that from the inverse solution in the inviscid region for both N = 11 and N = 21 points (with radiative flux calculations at

11 points). The enthalpy profile computed with $N = 11$ agrees well enough with the enthalpy profile computed with $N = 21$ that the difference is not discernible in figure 12.

A complete summary of the calculated radiative heat fluxes at the wall is given in table 2 for the cases examined in the present study. Also shown in the table are comparisons with existing sources. Although the inverse solution is considered more accurate than the integral-relations solution in defining shock-layer profiles, it is interesting to note that the radiative heat fluxes at the wall predicted by the three methods fall within 3 percent of each other.

Comparisons of air-to-air injection results with existing solutions.- The viscous radiating solutions for air-to-air injection with $(\rho v)_w = -0.1$ are compared in figures 13 and 14 for a nose radius of 3.048 meters and the following free-stream conditions:

$$U'_\infty = 15.25 \text{ km/sec}$$

$$\rho'_\infty = 2.72 \times 10^{-7} \text{ g/cm}^3$$

$$p'_\infty = 1.95 \times 10^{-4} \text{ atm}$$

The wall enthalpy is 0.028, which corresponds to a wall temperature of 3600 K.

Figure 13 shows results across the entire shock layer for conditions identical with those given above. Results from the present analysis are compared with those from Rigdon et al. (ref. 12) and Smith et al. (ref. 13) and with unpublished results obtained by K. H. Wilson of Lockheed Missiles & Space Company from his method given in reference 14. In general, for air-to-air injection, the flow-field results from all approaches are in fairly good agreement although there are notable detailed exceptions in the flow-field structure which are discussed below. Also, the wall radiative heat fluxes computed by Wilson, Smith et al., and the present analysis are within 5 percent, whereas the results of Rigdon et al. are about 30 percent higher. This disagreement is attributed primarily to the differences in the radiation model employed in the first three approaches (RATRAP) and that employed by Rigdon et al. (SPECS).

Although the radiative heat fluxes predicted by Wilson are in good agreement with the present method, there was a notable 10-percent difference in the shock-layer thickness predicted by Wilson and by the other three approaches. The possible sources of this difference are associated with the solution of the x-momentum equation and are discussed below.

Tangential velocity gradient: For all the solutions, there is fairly good agreement in the tangential velocity gradient in the inviscid outer region and, in general, somewhat poorer agreement near the body as shown in figure 13(a). Near the body the velocity gradient from the present method is close to that obtained by Rigdon et al. (ref. 12).

The major differences near the body in the present solution and in the unpublished results of Wilson are due to differences in the computed inner layer and boundary-layer thickness, as shown in figure 14(a).

A possible source of the discrepancy between Wilson's solution for the inner region and the present results is the pressure-gradient coefficient $\left(\frac{\partial^2 p}{\partial x^2}\right)_{x=0}$ assumed. The higher the pressure coefficient, the more rapidly the oncoming flow sweeps around the body, and thus, the smaller the standoff distance. A coefficient of -3.0 is assumed by Wilson, whereas the value of -2.0 is assumed by Rigdon et al. and in the present analysis. Smith et al. use a value of -2.5 which has been correlated by Inouye (ref. 42) on the basis of inverse flow-field solutions.

A case was run to examine the effect of the pressure coefficient. The results are shown in figure 15. The pressure-gradient coefficient was set to -3.0, and the shock was considered to remain concentric. Thus, the velocity gradient behind the shock became, by equation (38), $a_s = \sqrt{\beta/2} = 1.22$. The results indicated a decrease in shock-layer thickness of 17 percent, which agrees more closely with Wilson's shock-layer thickness. However, most of the adjustment occurred in the outer inviscid region (by virtue of the higher velocity gradients in this region). As shown in figure 15, there was no significant change in the extent of the inner region.

Two assumptions are made by Wilson (ref. 14) which are not necessary in the present method. First, because of numerical stability problems, Wilson treats the inner region as inviscid and begins his fully viscous calculations near the interface between the inner region and the boundary layer. A case was run with the assumption that the first five nodal points, up to $y/y_s \approx 0.04$, were inviscid. This was accomplished by setting $\mu = 0$ at these points. There were no discernible differences in the fully viscous and the inviscid-viscous solutions. This indicates that the assumption of an inviscid inner region is valid for the massive-blowing problem.

The second assumption made by Wilson (ref. 14) in his solution to the governing equations is that the product of density and viscosity is constant across the shock layer and is given by $\rho\mu = (\rho\mu)_w$. Since the value $\rho\mu$ within the boundary layer for the comparison case examined was about one-half the value at the wall, it was decided to examine this assumption. Two cases were run for $(\rho v)_w = 0$ and -0.1 in which the density-viscosity products appearing in the x-momentum equations and the energy equation were set equal to $(\rho\mu)_w$ at each nodal point. The results of the constant $\rho\mu$ cases and the corresponding variable $\rho\mu$ cases were nearly identical. This is shown in figure 16. The results tend to indicate that although viscosity is important in the boundary layer, it need not be too well defined in the computations since the boundary layer is actually a thin transition region which adjusts to the outer and inner flow regions.

Again, in figure 13(a), the results from the integral solution of Smith et al. (ref. 13) for the total shock-layer thickness agree fairly well with the present results; however, their inviscid inner-layer thickness agrees more closely with Wilson's unpublished calculations, as is seen in figure 14(a).

Also shown in figure 14(a) are the results obtained by Wilson and Hoshizaki (ref. 28) from their integral solution approach. The comparisons indicate that the integral method, which was sufficient for radiation studies without blowing, is not adequate for the strong-blowing conditions.

Total enthalpy: The total-enthalpy results across the shock layer are compared in figure 13(b). With the exception of the differences in the shock-displacement distances which have been noted, the present results compare favorably with the unpublished results of Wilson. The enthalpy results of Smith et al. (ref. 13) are fairly good overall. Their method is based on a one-strip integral-relations solution for the outer inviscid flow coupled with an integral solution for the boundary layer and inner inviscid region. It is not expected to yield the detailed flow-field structures obtainable from the other approaches (i.e., Wilson (ref. 14), Rigdon et al. (ref. 12), and the present method).

Temperature: The temperature results obtained from the four approaches agree fairly well in the outer inviscid region, but the agreement is somewhat poorer in the boundary layer and near the wall, as shown in figure 13(c). Since the radiative heat fluxes are strong functions of temperature, the results near the wall are compared in more detail in figure 14(b). The present results compare favorably with the unpublished results of Wilson.

The results of the simplified method of Smith et al. (ref. 13) shown in figure 14(b) indicate a nearly constant temperature in the inviscid inner region, whereas all other solutions indicate an appreciable drop in temperature going toward the body, because of radiation exchange. It is unfortunate that because of differences in the radiation models, a more direct comparison cannot be made with Rigdon et al. (ref. 12), who also solve the fully coupled equations for the viscous, radiating shock layer. However, it is apparent from their temperature profile that the radiation model has a strong influence on the resulting temperature and predictions of radiative heat fluxes.

Radiative heat flux: The radiative heat fluxes are shown in figure 13(d). The present results indicate that the inviscid inner air layer is relatively ineffective in reducing the radiation to the wall, and as a consequence, the wall heat fluxes of Wilson and of Smith et al. (ref. 13), who predict thinner inner layers, agree well with the present results.

A summary of the predicted heat fluxes at the wall for the various air-to-air injection rates is given in table 2(a).

It is interesting to note that the radiative heat fluxes at the wall converged much more rapidly than the detailed thermodynamic properties across the shock layer. For example, in figure 17 the heat flux at the wall for $(\rho v)_w = -0.1$ converged within ±2 percent of its final value after only five iterations, whereas the density values in the inner region ($\eta = 0.2$ and 0.4) were about 50 percent below their final value. This indicates that the radiative heat fluxes at the wall for air-to-air injection may not be as sensitive to the thermodynamic properties in the inner region as previously expected. If only the gross quantity of the heat flux at the wall is of interest, then the density-convergence criterion of 1 or 2 percent could be relaxed considerably to provide substantial savings in computational time for studies with air-to-air injection.

As previously noted, the air in the inner region is not too effective in absorbing the incident radiation from the high-temperature outer layer. However, since certain chemical species of ablators are strong absorbers and emitters, the flux to the wall may be sensitive to the relative amounts of these species. If this is the case, then a detailed definition of properties across the shock layer is desired. Thus, the density-convergence criterion of 2 percent was retained in the subsequent ablation study.

Solutions of Radiating Flow Field With Ablation Products

The solutions to the fully coupled, viscous, radiating flow field with injection of ablation products are presented in this section. As a result of the stability study (appendix B) it was decided to retain the windward-difference approximation for this analysis. The results of the present analysis are compared with existing solutions. The validity of assuming a binary diffusion model is also investigated in this section.

The heat-shield material is considered to be a carbon-phenolic ablator composed of 90 to 95 percent carbon with the remaining elemental mass fractions consisting of nitrogen, oxygen, and hydrogen. Exact values of the elemental mass fractions of each of the constituents are specified for the particular cases presented.

Check on assumption of binary diffusion model.- The binary diffusion coefficients were computed on the basis of the dominant species present. For the ablator, the dominant species is atomic carbon, and for air, it is atomic nitrogen; hence, the binary diffusion coefficient for diffusion of atomic carbon and atomic nitrogen was used in the computations.

However, to obtain an indication of the validity of the assumption, two cases were run at identical conditions with the exception that diffusion of atomic carbon and atomic nitrogen was used in one solution in calculating the diffusion coefficient and diffusion of atomic hydrogen and atomic nitrogen was used in the other solution. A comparison of ablator mass-fraction profiles obtained from solution of the elemental-diffusion equation with the two assumptions is shown in figure 18 for the conditions noted. The two profiles show that the results differ in the mixing region and its extent, with the ablator elements extending farther into the shock layer for the hydrogen-nitrogen diffusion coefficient. This is to be expected since D_{H-N} is almost an order of magnitude larger than D_{C-N}, as shown in the figure.

A detailed analysis of the heat-flux distributions for the two cases indicated a maximum difference in the radiative heat fluxes of 3 percent, which occurred in the outer inviscid mixing region ($\eta = 0.7$), as shown in figure 19. At the wall, the nondimensional heat fluxes differed by less than 1 percent (-0.02892 for D_{H-N} and -0.02917 for D_{C-N}). The shock-layer thicknesses y_s were 0.04173 and 0.04168 for D_{H-N} and D_{C-N}, respectively. Thus, it appears that for the conditions examined in this study, the assumption of a binary diffusion model is valid.

General results from the present analysis.- The results obtained for $(\rho v)_w = 0$, -0.1, and -0.2 are shown in figure 20 for a nose radius of 3.048 m and the following free-stream conditions:

$$U'_\infty = 15.25 \text{ km/sec}$$

$$\rho'_\infty = 2.72 \times 10^{-7} \text{ g/cm}^3$$

$$p'_\infty = 1.95 \times 10^{-4} \text{ atm}$$

A wall enthalpy of -0.049, which corresponds to a wall temperature of 3600 K, was specified for the cases with injection of carbon-phenolic ablation products with the following elemental mass fractions:

$$\bar{\alpha}_C = 0.9207$$

$$\bar{\alpha}_N = 0.0086$$

$$\bar{\alpha}_O = 0.0491$$

$$\bar{\alpha}_H = 0.0216$$

For the no-blowing case, air is adjacent to the wall, and an enthalpy of 0.028 corresponds to the wall temperature of 3600 K.

In general, the profiles and parameters are much the same as those for air injection with the exceptions of the enthalpy profiles for $(\rho v)_w = -0.2$ and the radiative heat fluxes.

Even with the windward-difference form of the energy equation, the enthalpy profile for a blowing rate $(\rho v)_w$ of -0.2 was irregular near the stagnation point. This solution was near convergence when the calculations were terminated on the computer. Apparently, this blowing rate is near the stability limit for the technique employed herein for the solution to the governing equations. As can be seen in figure 20(f), the density and temperature profiles, which are used in the computations of radiative heat flux, are much better behaved than the enthalpy profiles.

It can be seen from the radiative-heat-flux profiles of figure 20(g) that the flux out of the shock (at $\eta = 1.0$) increased with increasing ablator mass injection, whereas for air-to-air injection the flux at the shock was nearly insensitive to the blowing rate. (See fig. 11(f).) The heat fluxes at the wall, which are of primary interest, decreased with blowing rate for the carbon-phenolic ablator; the reductions were 34 and 39 percent of the no-blowing radiative heat flux for $(\rho v)_w = -0.1$ and -0.2, respectively. Thus, the ablation products are considerably more effective than air in reducing the heat flux to the wall.

It is not clear whether the large negative heat flux near the stagnation point for $(\rho v)_w = -0.2$ is real or a result of the uncertainty in the calculations of the thermodynamic properties. This case is compared with the solution of Rigdon et al. (ref. 12) in the following section.

Comparisons with existing solutions.- Two carbon-phenolic injection cases were run for comparison: one at a blowing rate of -0.076 for comparison with the results of Smith et al. (ref. 13) and Chin (ref. 2), and one at a blowing rate of -0.2 for comparison with the results of Rigdon et al. (ref. 12). The pertinent free-stream and wall conditions are noted in figures 21 and 22 for these corresponding cases. In general, the results for the thermodynamic and flow properties are in reasonable agreement, but there are noticeable exceptions relating to the heat-flux computations which are discussed below.

It should be noted that the close agreement of the wall heat-flux prediction with Chin's computations (ref. 2) may be fortuitous. Chin's earlier radiation model is sufficiently different from RATRAP to make any quantitative comparison meaningless. This is evident from table 2, where it is observed that the predictions of no-blowing radiative heat flux from Chin and from the present method differ by 20 percent.

The comparison of interest for this case is with the results of Smith et al. (ref. 13). It is noted in figure 21(e) that the present solution predicts a wall heat flux about 30 percent lower than that of Smith et al. An important conclusion made in reference 13 is that the radiation to the wall is not attenuated as much as previously predicted by Chin and by Rigdon et al. (ref. 12). This was attributed to the presence of large percentages of CN, which is a strong emitter, in the mixing region. A comparison of the mole fractions of the major chemical species is shown in figure 21(d). The comparisons are good considering the differences in the temperature distributions; however, it is noted that the peak mole fraction for CN predicted by the present method is only about one-half of that predicted by Smith et al. This discrepancy in the level of CN occurs in the region where Smith et al. employ a cubic fit to the elemental-diffusion equation in order to join the wall products in the inner shear layer with the air composition beyond the boundary layer. It thus appears that contrary to the results of the air-to-air injection study, which did not require a very accurate resolution of properties near the wall, the study with ablation-products injection indicates that these properties must be well defined near the wall to generate accurate predictions of wall radiative heat flux.

The comparison with Rigdon et al. (ref. 12) indicates reasonably good agreement in the radiative heat-flux profiles (fig. 22(a)), although there are significant differences in the radiation models employed. The predicted shock-layer thicknesses are within about 5 percent. A slight waviness is noted in the ρv profile of Rigdon et al. (fig. 22(a)) near the stagnation point $\left(y/y_s = 0.3\right)$. In all the cases calculated by the present method, the ρv profile was smooth in this region. It is not apparent whether this irregularity predicted by Rigdon et al. is real or related to the numerical procedure used for integrating out in both directions from the stagnation point. It is noted that their solution also exhibits an irregularity in the temperature profile near the stagnation point as does the present solution.

Summary of Wall Radiative Heat Fluxes

A summary of the wall radiative heat fluxes calculated by the present method for the various conditions examined in this study and corresponding predictions from previous investigations are given in table 2 for comparison. With the exception of the no-blowing results of Suttles (ref. 31) and the air-injection case of Wilson (unpublished), the present method predicts heating rates slightly to considerably lower than those calculated by previous investigators.

These results are also summarized in figure 23, which illustrates the effectiveness of the carbon-phenolic ablator products in reducing the wall radiative heat fluxes. As can be seen from the figure, there is general agreement of all sources that air injection is moderately effective in reducing the heat transfer to the wall and, with the exception of the results of Smith et al. (ref. 13), that the ablation products of the carbon-phenolic heat shield are highly effective in reducing the fluxes.

As can also be seen from figure 23 and table 2, there is no consistent agreement in any of the sources when both the no-blowing and blowing results are considered. For sources which use different radiation-transport models (Rigdon et al. (ref. 12) and Chin (ref. 2)), this disagreement is due, at least in part, to the differences in the radiation models. For sources which use the same model (Smith et al. and the present method), this disagreement is attributed to differences in the temperature distributions near the wall. The data available were insufficient to evaluate fully the unpublished results of Wilson, with the exception of the assessment of the validity of the assumptions required in his analysis. These assumptions have been previously discussed and shown to be valid for air-to-air injection with $(\rho v)_w = -0.1$.

For air-to-air injection, the present results indicate a 10-percent reduction in the no-blowing wall radiative heat flux for $(\rho v)_w = -0.1$ and a 16-percent reduction for $(\rho v)_w = -0.2$. For injection of carbon-phenolic ablation products at corresponding blowing rates, the reduction is 34 and 39 percent, respectively. Since ablation rates are typically expected to be about 0.1 (see Smith et al. (ref. 13)), then the 34-percent reduction in the radiative heat flux represents a significant savings in heat-shield weight.

CONCLUDING REMARKS

An implicit finite-difference scheme is developed for the solution of the fully coupled equations for the viscous, radiating stagnation streamline with the effects of strong blowing included. Solutions are presented for both air-to-air injection and ablation-products injection at rates up to 20 percent of the free-stream mass-flow rate. The free-stream conditions examined are typical of interplanetary return conditions into earth's atmosphere near the point of peak radiative heating in the entry trajectory. A detailed radiative-transport computer code (RATRAP) which accounts for both continuum and line radiation exchange processes is utilized in the study.

With a minimum number of assumptions for the initially unknown parameters and profile distributions, convergent solutions to the full stagnation-line equations are rapidly obtained by a method of successive approximations. No singularities exist in this formulation of the finite-difference equations. Damping of selected profiles is required to aid convergence of the massive-blowing cases; however, even for these cases, no "patching" of the viscous and inviscid regions is required. The results demonstrate that windward differencing of the convective term in the elemental-diffusion equation is required for a stable solution to this equation. Although the central-difference approximation to the energy equation yields satisfactory solutions when radiation is included, the results are considerably improved for a blowing rate of 20 percent of the free-stream rate when the convective term is windward differenced in this equation also.

Comparisons are made with currently existing solutions to the equations for the radiating shock layer. The present method predicts lower wall radiative heat fluxes for carbon-phenolic ablation than those predicted by previous investigators.

The results indicate that the ablation products are highly effective in blocking the incident radiation from the high-temperature outer layer of the shock. For blowing rates of 0.1 and 0.2, typical reductions in radiative heat flux at the wall range from 34 to 39 percent of the values for no blowing.

For air injection, the inner air layer is shown to be relatively ineffective in blocking the incident radiation; hence, the thermodynamic properties need not be as well defined for air injection as for ablation-products injection.

The validity of assuming a binary diffusion model was examined in the present analysis, and although a study with a multicomponent diffusion model may remain meaningful for conditions and ablators other than those examined in the present study, the results indicate that the multicomponent diffusion model is not required.

Langley Research Center,
National Aeronautics and Space Administration,
Hampton, Va., July 28, 1972.

APPENDIX A

RADIATION MODEL

The RATRAP radiative-transport model developed by Wilson (ref. 10) has been discussed in great detail by Wilson (ref. 10), Suttles (refs. 37 and 31), and Wilson and Hoshizaki (ref. 28). A summary of Suttles' discussion on the development of the governing radiative-transport equation employed by RATRAP and some details of the radiation model are given in this appendix.

The RATRAP code, which includes the detailed line radiative calculations (sometimes referred to as RATRAP II, since it has been upgraded by its originators, see Wilson and Hoshizaki (ref. 28)), is written for the calculation of the radiative heat flux at any point within a planar (tangent) slab in which the thermodynamic properties vary in only the direction normal to the slab. Local thermodynamic and chemical equilibrium is assumed. A distribution of two thermodynamic variables plus the elemental mass fractions for gaseous mixtures of carbon, nitrogen, oxygen, and hydrogen is required for the radiation computations.

In order to evaluate equation (17) for the radiative heat flux, it is necessary to calculate the spectral linear absorption coefficients α_ν, which are functions of the thermodynamic properties (p and T) and the number densities of the chemical species. Twenty chemical species are considered in the thermodynamic calculations. They are C_2, N_2, O_2, H_2, C, N, O, H, CO, CN, C_2H, C_3H, C_4H, HCN, C_2H_2, C^-, C^+, N^+, O^+, and H^+.

The total spectral absorption coefficient is separated into continuum and line contributions in the RATRAP calculations. The continuum spectral absorption processes considered are the free-free transitions (acceleration of free electrons in the vicinity of atoms and ions) of C, C^+, N, N^+, O, O^+ and the free-bound and bound-free transitions (deionization and ionization, respectively, of the H atoms and positively ionized particles). Molecular bands are also included in the continuum calculations. These molecule contributions and frequency intervals from Wilson and Hoshizaki (ref. 28) are tabulated below.

Molecule contribution	Photon energy range $\hbar\nu$ for significant absorption, eV
H_2 Werner	$11 \leq \hbar\nu \leq 15.494$
Photoionization	$15.494 \leq \hbar\nu \leq 25$
C_2 Swan	$1.8 \leq \hbar\nu \leq 6.0$
Fox-Herzberg	$1.8 \leq \hbar\nu \leq 5.35$
Mulliken	$5.35 \leq \hbar\nu \leq 6.0$
Freymark	$1.8 \leq \hbar\nu \leq 6.0$
CN violet	$2.0 \leq \hbar\nu \leq 6.0$
CO 4th positive	$7 \leq \hbar\nu \leq 10$
N_2 Birge-Hopfield	$11 \leq \hbar\nu \leq 14.2$
O_2 Schumann-Runge	$7 \leq \hbar\nu \leq 9.2$

For the calculation of the continuum contribution to the heat flux, the absorption coefficients for the individual species are weighted with their respective number densities and approximated by curve fits over frequency ranges. The heat-flux equation (17) is subsequently evaluated by numerically integrating over y and over the frequency, with 11 values of y and 31 values of frequency used.

The atomic-line radiation component arises as a result of the many bound electronic transitions which occur in the atomic nitrogen and oxygen species (line radiation from carbon and hydrogen species is not included in RATRAP). This component is obtained by first grouping certain line contributions within various frequency intervals. The net line radiation is then calculated by summing the contributions from these line groups. Eighteen line groups, with a total of 65 lines, are used in RATRAP.

The total radiative heat flux at each point is obtained by adding the continuum and line radiation contributions.

APPENDIX B

STABILITY STUDY OF THE ELEMENTAL-DIFFUSION AND ENERGY EQUATIONS

The solution to the elemental-diffusion equation is required in the analysis of the shock layer with ablation-products injection. Use of the central-difference form of the diffusion equation results in a numerical instability. This numerical instability is a strong oscillation across the shock layer in the computed elemental profiles. This instability is eliminated by windward differencing of the convective term in the diffusion equation. This appendix presents a stability analysis of the two formulations of the diffusion equation and also the energy equation, which is analogous to the diffusion equation, with an additional term for radiation.

The properties vary rapidly across the shock layer. In order to obtain some insight into the stability of the diffusion equation and the associated nodal-spacing requirements, the elemental-diffusion equation (35) is simplified by assuming $\kappa^2\rho^2 D_{12}$ and $\hat{\delta}\kappa^2\rho v$ to be constant, so that equation (35) simplifies to

$$\frac{d^2\overline{\alpha}}{d\eta^2} + \frac{\hat{\delta}v}{\rho D_{12}}\frac{d\overline{\alpha}}{d\eta} = 0 \tag{B1}$$

Equation (B1) is cast in finite-difference form by using central differences:

$$\frac{\overline{\alpha}_{n+1} - 2\overline{\alpha}_n + \overline{\alpha}_{n-1}}{(\Delta\eta)^2} + \frac{\hat{\delta}v}{\rho D_{12}}\frac{\overline{\alpha}_{n+1} - \overline{\alpha}_{n-1}}{2\,\Delta\eta} = 0 \tag{B2}$$

For $\frac{\hat{\delta}v\,\Delta\eta}{2\rho D_{12}}$ = Constant, this equation may be solved by assuming the solution

$$\overline{\alpha}_n = C\lambda^n \tag{B3}$$

Substitution of equation (B3) into equation (B2) and simplification results in the characteristic equation for λ:

$$\left(1 + \frac{\hat{\delta}v\,\Delta\eta}{2\rho D_{12}}\right)\lambda^2 - 2\lambda + \left(1 - \frac{\hat{\delta}v\,\Delta\eta}{2\rho D_{12}}\right) = 0 \tag{B4}$$

The solutions for λ are

$$\left.\begin{aligned} \lambda_1 &= 1 \\ \lambda_2 &= \frac{1 - \dfrac{\hat{\delta}v\,\Delta\eta}{2\rho D_{12}}}{1 + \dfrac{\hat{\delta}v\,\Delta\eta}{2\rho D_{12}}} \end{aligned}\right\} \tag{B5}$$

The λ_1 solution corresponds to a constant error across the shock layer and, as such, is removed by the boundary conditions. The λ_2 solution is an oscillation if $\lambda_2 < 0$, which implies that $\left|\frac{\hat{\delta} v \, \Delta\eta}{2\rho D_{12}}\right| > 1$. If $\lambda_2 > 0$, this contribution has a monotonic variation across the shock layer and is thus eliminated by the boundary conditions. The condition for eliminating the undesirable oscillation is thus

$$\left|\frac{\rho v \hat{\delta} \, \Delta\eta}{2\rho^2 D_{12}}\right| < 1 \tag{B6}$$

The nodal-spacing requirement for stability can be established by noting that

$$\hat{\delta} = O\left[1\right]$$

and

$$\rho v = O\left[1\right]$$

In this paper, a typical value of ρ is 20, and a typical value of D_{12} is 10^{-6}, so that

$$\Delta\eta < \frac{2\rho^2 D_{12}}{\rho v \hat{\delta}} = O\left[0.8 \times 10^{-3}\right]$$

This nodal spacing corresponds to approximately 1250 nodal points.

A case was run in which 1001 nodal points were used for the solution of the elemental-diffusion equation, with the same 21 points used for the other equations. Although some improvement was noted in the solution, the instability was not eliminated.

The numerical results which substantiate this stability analysis are shown in figure 24. The computed mass fractions for a diffusion coefficient of 10^{-6} are shown in figure 24(a) for a nodal spacing of 0.05. The solution is clearly unstable. The results obtained when the coefficient was increased to 1.25×10^{-4} and $\Delta\eta$ was set to 0.1 (which accomplishes the same stability effect as decreasing the nodal spacing to 4×10^{-4}) is shown in figure 24(b). The sharp oscillations have vanished, but $\overline{\alpha}_F$ still exceeds the value of 1.0. The case was rerun for a nodal spacing of 0.02 with no noticeable improvement. Only when D_{12} was raised to 10^{-3} did $\overline{\alpha}_F$ monotonically decrease from 1.0 at the wall to 0 at the shock.

Since the central-difference form of the elemental-diffusion equation was inadequate, a windward-difference form for the convective term was employed. It has been shown that windward differencing of the convective term stabilizes certain fluid-flow computations. (See, e.g., ref. 48 or ref. 49.)

Equation (B1), when written in finite-difference form with windward differencing of the convective term, becomes

$$\frac{\bar{\alpha}_{n+1} - 2\bar{\alpha}_n + \bar{\alpha}_{n-1}}{(\Delta\eta)^2} + \frac{\hat{\delta} v}{\rho D_{12}} \frac{\bar{\alpha}_{n+1} - \bar{\alpha}_n}{\Delta\eta} = 0 \tag{B7}$$

In equation (B7), it is assumed that v is positive, so that a fluid particle would flow from the (n+1)th node to the nth node. If v is negative, the appropriate windward-difference form is

$$\frac{\bar{\alpha}_{n+1} - 2\bar{\alpha}_n + \bar{\alpha}_{n-1}}{(\Delta\eta)^2} + \frac{\hat{\delta} v}{\rho D_{12}} \frac{\bar{\alpha}_n - \bar{\alpha}_{n-1}}{\Delta\eta} = 0 \tag{B8}$$

As before, a solution form (B3) is assumed, and results in the characteristic equation for λ:

$$\left(1 + \frac{\rho v \hat{\delta}\, \Delta\eta}{\rho^2 D_{12}}\right)\lambda^2 - \left(2 \pm \frac{\rho v \hat{\delta}\, \Delta\eta}{\rho^2 D_{12}}\right)\lambda + 1 = 0 \tag{B9}$$

The plus sign corresponds to positive v when equation (B7) is used, and the minus sign corresponds to negative v when equation (B8) is used. The solutions for λ are

$$\left.\begin{aligned} \lambda_1 &= 1 \\ \lambda_2 &= \frac{1}{1 \pm \dfrac{\rho v \hat{\delta}\, \Delta\eta}{\rho^2 D_{12}}} \end{aligned}\right\} \tag{B10}$$

Because both roots of λ are positive, there are no oscillations in the solution when windward differencing of the convective term is employed.

A physical explanation given for using windward differencing of the convective term is that if fluid is flowing downstream, the upstream cell influences the downstream cell more than the downstream cell influences the upstream cell. The mathematical reason for windward differencing is that higher order harmonics (ref. 48) that are introduced into the solution because of finite-difference approximations to the differential equations decay exponentially, whereas for central-difference formulations these higher order disturbances can be exponentially amplified.

The results obtained for both central- and windward-difference forms of the diffusion equation are shown in figure 25. The computations were for a viscous, radiating shock layer, and a binary diffusion coefficient for atomic hydrogen and atomic nitrogen was assumed. The windward-difference formulation yields a stable solution in which $\bar{\alpha}_F$ monotonically decreases across the shock layer.

A check case was run to establish the effect on the $\bar{\alpha}_F$ profiles of the damping that is introduced by the windward-difference formulation. This damping, which is a form of artifical viscosity, tends to smooth, or smear out, the gradients more than is natural. Both central- and windward-difference solutions were obtained for diffusion coefficients which yield stable solutions for central-difference approximations. The results from these two formulations, shown in figure 26, indicate that the windward-difference formulation does not introduce any noticeable artificial viscosity for this case.

When constant density and constant transport properties are assumed, the energy and the elemental-diffusion equations (eqs. (34) and (35)), respectively, can be written as (where the convective term on the right-hand side of the energy equation has been neglected)

$$\rho v \frac{dH}{d\eta} = -\frac{\rho\mu}{\hat{\delta} N_{Re} N_{Pr}} \frac{d^2H}{d\eta^2}$$

and

$$\rho v \frac{d\overline{\alpha}_F}{d\eta} = -\frac{\rho^2 D_{12}}{\hat{\delta}} \frac{d^2\overline{\alpha}_F}{d\eta^2} = -\frac{\rho\mu}{\hat{\delta} N_{Re} N_{Sc}} \frac{d^2\overline{\alpha}_F}{d\eta^2}$$

where N_{Sc}, the Schmidt number, is given by

$$N_{Sc} \equiv \frac{\mu'}{\rho' D'_{12}}$$

Since the Prandtl and Schmidt numbers are typically of order unity, then the energy equation and the momentum equation are controlled by the same stability requirements as the elemental-diffusion equation. When radiation becomes a significant contributor to energy transport, it acts as an additional mode of conduction. Thus, in central-difference form, radiation increases the stability of the energy equation beyond that of the elemental-diffusion equation, so that a well-behaved diffusion solution assures a well-behaved energy solution.

As a result of this analysis, the convective term in the energy equation $\left(\rho v \frac{dH}{d\eta}\right)$ was recast in windward-difference form and the nonradiating equilibrium-air solution for $(\rho v)_w = -0.2$ was rerun. The profiles of enthalpy, density, and velocity gradient became smooth. The results of the solution for the x-momentum and energy equations are plotted in figure 27 and compared with the previous central-difference solutions.

A significant change in the shock layer thickness also occurred when the windward-difference form of the energy equation was used to improve the profiles. The shock-layer thickness y_s was reduced by about 12 percent from 0.0703 to 0.0622 in going from central- to windward-difference form. It was found that this reduction in y_s was due primarily to the large blowing rate which introduced the strong oscillations in the profiles for the central-difference formulation. The nonradiating cases for $(\rho v)_w = 0$ and $(\rho v)_w = -0.1$ were rerun with the improved formulation of the energy equation. There was no change in y_s for $(\rho v)_w = 0$, and there was a 3-percent reduction in y_s for $(\rho v)_w = -0.1$.

The strong oscillations in the enthalpy profiles were not present in the radiating solutions. However, the $(\rho v)_w = -0.1$ case for $U_\infty' = 15.25$ km/sec was rerun to determine the effect of the windward-difference approximation in energy equations. The radiative flux at the wall was unchanged and the shock standoff distance increased by only 2 percent.

As a result of this stability study it was decided to use the windward-difference approximations to the convective terms in the energy and elemental-diffusion equations for the analysis with radiation and injection of ablation products.

REFERENCES

1. Walberg, G. D.; and Sullivan, E. M.: Ablative Heat Shields for Planetary Entries – A Technology Review. Space Simulation, J. C. Richmond, ed., NBS Spec. Publ. 336, Oct. 1970, pp. 751-812.
2. Chin, Jin H.: Radiation Transport for Stagnation Flows Including the Effect of Lines and Ablation Layer. AIAA Paper No. 68-664, June 1968.
3. Libby, Paul A.; and Sepri, Paavo: Stagnation Point Flow With Complex Composition. Phys. Fluids, vol. 11, no. 8, Aug. 1968, pp. 1621-1627.
4. Libby, Paul A.: Numerical Analysis of Stagnation Point Flows With Massive Blowing. AIAA J., vol. 8, no. 11, Nov. 1970, pp. 2095-2096.
5. Kassoy, David R.: On Laminar Boundary Layer Blowoff. SIAM J. Appl. Math., vol. 18, no. 1, Jan. 1970, pp. 29-40.
6. Libby, Paul A.: The Homogeneous Boundary Layer at an Axisymmetric Stagnation Point With Large Rates of Injection. J. Aerosp. Sci., vol. 29, no. 1, Jan. 1962, pp. 48-60.
7. Kubota, Toshi; and Fernandez, Frank L.: Boundary-Layer Flows With Large Injection and Heat Transfer. AIAA J., vol. 6, no. 1, Jan. 1968, pp. 22-28.
8. Hoshizaki, H.; and Lasher, L. E.: Convective and Radiative Heat Transfer to an Ablating Body. AIAA J., vol. 6, no. 8, Aug. 1968, pp. 1441-1449.
9. Blottner, F. G.: Viscous Shock Layer at the Stagnation Point With Nonequilibrium Air Chemistry. AIAA J., vol. 7, no. 12, Dec. 1969, pp. 2281-2288.
10. Wilson, K. H.: RATRAP – A Radiation Transport Code. 6-77-67-12, Lockheed Missiles & Space Co., Mar. 14, 1967.
11. Hansen, C. Frederick: Approximations for the Thermodynamic and Transport Properties of High-Temperature Air. NASA TR R-50, 1959. (Supersedes NACA TN 4150.)
12. Rigdon, W. S.; Dirling, R. B., Jr.; and Thomas, M.: Stagnation Point Heat Transfer During Hypervelocity Atmospheric Entry. NASA CR-1462, 1970.
13. Smith, G. Louis; Suttles, John T.; Sullivan, Edward M.; and Graves, Randolph A., Jr.: Viscous Radiating Flow Field on an Ablating Body. AIAA Paper No. 70-218, Jan. 1970.
14. Wilson, K. H.: Massive Blowing Effects on Viscous, Radiating, Stagnation-Point Flow. AIAA Paper No. 70-203, Jan. 1970.

15. Anderson, John D., Jr.: An Engineering Survey of Radiating Shock Layers. AIAA J., vol. 7, no. 9, Sept. 1969, pp. 1665-1675.

16. Garrett, Lloyd Bernard: An Implicit Finite Difference Solution to the Viscous-Radiating Shock Layer With Strong Blowing. Ph. D. Thesis, North Carolina State Univ. at Raleigh, 1971.

17. Goulard, R.; Boughner, R. E.; Burns, R. K.; and Nelson, H. F.: Radiating Flows During Entry Into Planetary Atmospheres. IAF Paper RE70, Amer. Inst. Aeronaut. Astronaut., Oct. 1968.

18. Thomas, M.: The Spectral Linear Absorption Coefficients of Gases – Computer Program SPECS (H189). DAC-59135, Missile & Space Syst. Div., Douglas Aircraft Co., Inc., Dec. 1966. (Revised May 1967.)

19. Nicolet, W. E.: User's Manual for the Generalized Radiation Transfer Code (RAD/EQUIL). Rep. No. UM-69-9 (Contract NAS1-9399), Aerotherm Corp., Oct. 1, 1969. (Available as NASA CR-116353.)

20. Nicolet, William E.: Advanced Methods for Calculating Radiation Transport in Ablation-Product Contaminated Boundary Layers. NASA CR-1656, 1970.

21. Coleman, W. D.; Hearne, L. F.; Lefferdo, J. M.; and Vojvodich, N. S.: A Study of the Effects of Environmental and Ablator Performance Uncertainties on Heat Shielding Requirements for Blunt and Slender Hyperbolic Entry Vehicles. AIAA Paper No. 68-154, Jan. 1968.

22. Suttles, John T.: Comparison of the Radiative Flux Profiles and Spectral Detail From Three Detailed Nongray Radiation Models at Conditions Representative of Hypervelocity Earth Entry. NASA TM X-2447, 1972.

23. Wick, Bradford H.: Radiative Heating of Vehicles Entering the Earth's Atmosphere. The High Temperature Aspects of Hypersonic Flow, Wilbur C. Nelson, ed., AGARDograph 68, The MacMillan Co., 1964, pp. 607-627.

24. Hoshizaki, H.; and Wilson, K. H.: Viscous, Radiating Shock Layer About a Blunt Body. AIAA J., vol. 3, no. 9, Sept. 1965, pp. 1614-1622.

25. Howe, John T.; and Viegas, John R.: Solutions of the Ionized Radiating Shock Layer, Including Reabsorption and Foreign Species Effects, and Stagnation Region Heat Transfer. NASA TR R-159, 1963.

26. Hoshizaki, H.; and Wilson, K. H.: Convective and Radiative Heat Transfer During Superorbital Entry. AIAA J., vol. 5, no. 1, Jan. 1967, pp. 25-35.

27. Rigdon, W. S.; Dirling, R. B., Jr.; and Thomas, M.: Radiative and Convective Heating During Atmospheric Entry. NASA CR-1170, 1968.

28. Wilson, K. H.; and Hoshizaki, H.: Effect of Ablation Product Absorption and Line Transitions on Shock Layer Radiative Transport. NASA CR-1264, 1969.

29. Chou, Y. S.; and Blake, L. H.: Thin Radiating Shock Layer About a Blunt Body. NASA CR-1547, 1970.

30. Conte, S. D.: Elementary Numerical Analysis. McGraw-Hill Book Co., Inc., c.1965.

31. Suttles, John T.: A Method of Integral Relations Solution for Radiating, Nonadiabatic, Inviscid Flow Over a Blunt Body. NASA TN D-5480, 1969.

32. Ho, Hung-Ta; and Probstein, Ronald F.: The Compressible Viscous Layer in Rarefied Hypersonic Flow. Rarefied Gas Dynamics, L. Talbot, ed., Academic Press, 1961, pp. 525-552.

33. Scala, Sinclaire M.: The Equations of Motion in a Multicomponent Chemically Reacting Gas. Doc. No. R585D205 (Contract No. AF 04(645)-24), Missile Space Vehicle Dep., Gen. Elec. Co., Dec. 20, 1957. (Available from DDC as AD 600 491.)

34. Smith, G. Louis: Radiation Induced Precursor Flow Field Ahead of a Reentering Body. AIAA Paper No. 68-667, June 1968.

35. Hayes, Wallace D.; and Probstein, Ronald F.: Hypersonic Flow Theory. Academic Press, Inc., 1959.

36. Browne, H. N.; Williams, Mary M.; and Cruise, D. R.: The Theoretical Computation of Equilibrium Compositions, Thermodynamic Properties and Performance Characteristics of Propellant Systems. NAVWEPS Rep. 7043, U.S. Navy, June 8, 1960.

37. Suttles, John Timothy: A Method of Integral Relations Solution to the Non-Adiabatic Radiation Problem for an Inviscid Blunt-Body Flow Field. M.S. Thesis, Virginia Polytech. Inst., Mar. 1968.

38. Kourganoff, V.: Basic Methods in Transfer Problems – Radiative Equilibrium and Neutron Diffusion. Dover Publ., Inc., c.1963.

39. Hirschfelder, Joseph O.; Curtiss, Charles F.; and Bird, R. Byron: Molecular Theory of Gases and Liquids. John Wiley & Sons, Inc., c.1954. (Reprinted with corrections 1964.)

40. Svehla, Roger A.: Estimated Viscosities and Thermal Conductivities of Gases at High Temperatures. NASA TR R-132, 1962.

41. Crandall, Stephen H.: Engineering Analysis. McGraw-Hill Book Co., Inc., 1956.

42. Inouye, Mamoru: Blunt Body Solutions for Spheres and Ellipsoids in Equilibrium Gas Mixtures. NASA TN D-2780, 1965.

43. Potters, M. L.: A Matrix Method for the Solution of a Linear Second Order Difference Equation in Two Variables. MR 19 Math. Centrum (Amsterdam), 1955. (Reviewed by J. M. Hedgepeth in Appl. Mech. Rev., vol. 9, no. 3, Mar. 1956, p. 93.)

44. Bellman, Richard E.; and Kalaba, Robert E.: Quasilinearization and Nonlinear Boundary-Value Problems. Amer. Elsevier Pub. Co., Inc., 1965.

45. Garrett, L. Bernard; Suttles, John T.; and Perkins, John N. (With appendix C by G. Louis Smith and L. Bernard Garrett): A Modified Method of Integral Relations Approach to the Blunt-Body Equilibrium Air Flow Field, Including Comparisons With Inverse Solutions. NASA TN D-5434, 1969.

46. Fox, L.: The Numerical Solution of Two-Point Boundary Problems in Ordinary Differential Equations. Clarendon Press (Oxford), 1957.

47. Falanga, Ralph A.; and Sullivan, Edward M.: An Inverse-Method Solution for Radiating, Nonadiabatic, Equilibrium Inviscid Flow Over a Blunt Body. NASA TN D-5907, 1970.

48. Richtmyer, Robert D.: Difference Methods for Initial-Value Problems. Interscience Publ., Inc., 1957.

49. Larkin, B. K.: Heat Flow to a Confined Fluid in Zero Gravity. AIAA Paper No. 67-337, Apr. 1967.

TABLE 1.- MOLECULAR CONSTANTS FOR DIFFUSION COEFFICIENT

Species	Molecular constants		
	ϵ'_i/k^*, K	σ'_i, Å	M_i, g/g mole
C	30.6	3.385	12.01
N	71.4	3.298	14.01
H	37.0	2.708	1.008

TABLE 2.- SUMMARY OF WALL RADIATIVE HEAT FLUXES

(a) Air injection

$(\rho v)_w$	Source	$q'_{R,w}$, watts/cm^2
U'_∞ = 14.55 km/sec; $\rho'_\infty = 2.377 \times 10^{-7}$ g/cm^3; $p'_\infty = 1.6 \times 10^{-4}$ atm; R'_b = 3.427 m		
0	Suttles (ref. 31)	-2860
	Falanga and Sullivan (ref. 47)	-3000
	Present analysis	-2950
U'_∞ = 15.25 km/sec; $\rho'_\infty = 2.72 \times 10^{-7}$ g/cm^3; $p'_\infty = 1.95 \times 10^{-4}$ atm; R'_b = 3.048 m		
0	Rigdon et al. (ref. 12)	-5990
	Smith et al. (ref. 13)	-4170
	Present analysis	-4150
-0.1	Rigdon et al. (ref. 12)	-5130
	Smith et al. (ref. 13)	-3991
	Wilson (unpublished)	-3660
	Present analysis	-3740
-0.2	Rigdon et al. (ref. 12)	-4630
	Present analysis	-3490

(b) Carbon-phenolic injection

$(\rho v)_w$	Source	$q'_{R,w}$, watts/cm^2
U'_∞ = 15.25 km/sec; $\rho'_\infty = 1.77 \times 10^{-7}$ g/cm^3; $p'_\infty = 1.21 \times 10^{-4}$ atm; R'_b = 2.56 m		
0	Chin (ref. 2)	-3030
	Smith et al. (ref. 13)	-2795
	Present analysis	-2540
-0.076	Chin (ref. 2)	-1642
	Smith et al. (ref. 13)	-2188
	Present analysis	-1620
U'_∞ = 15.25 km/sec; $\rho'_\infty = 2.72 \times 10^{-7}$ g/cm^3; $p'_\infty = 1.95 \times 10^{-4}$ atm; R'_b = 3.048 m		
0	Rigdon et al. (ref. 12)	-5990
	Smith et al. (ref. 13)	-4170
	Present analysis	-4150
-0.1	Present analysis	-2790
-0.2	Rigdon et al. (ref. 12)	-2670
	Smith et al. (ref. 13)	-3246
	Present analysis	-2560

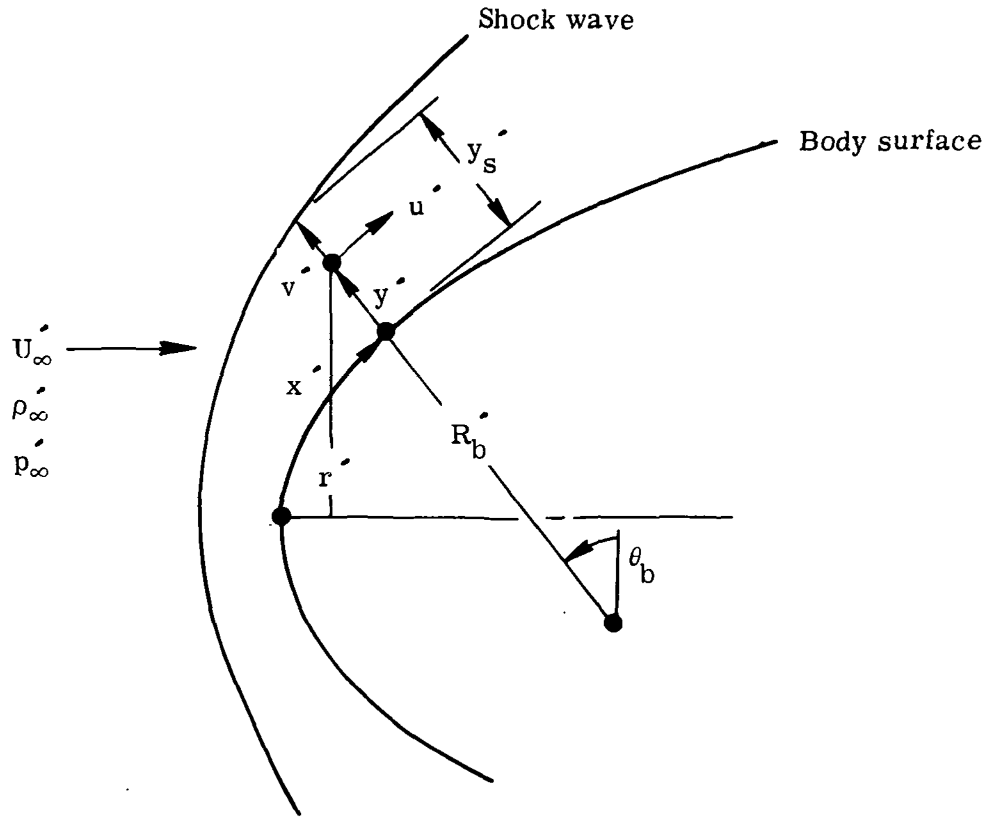

Figure 1.- Flow-field coordinate system.

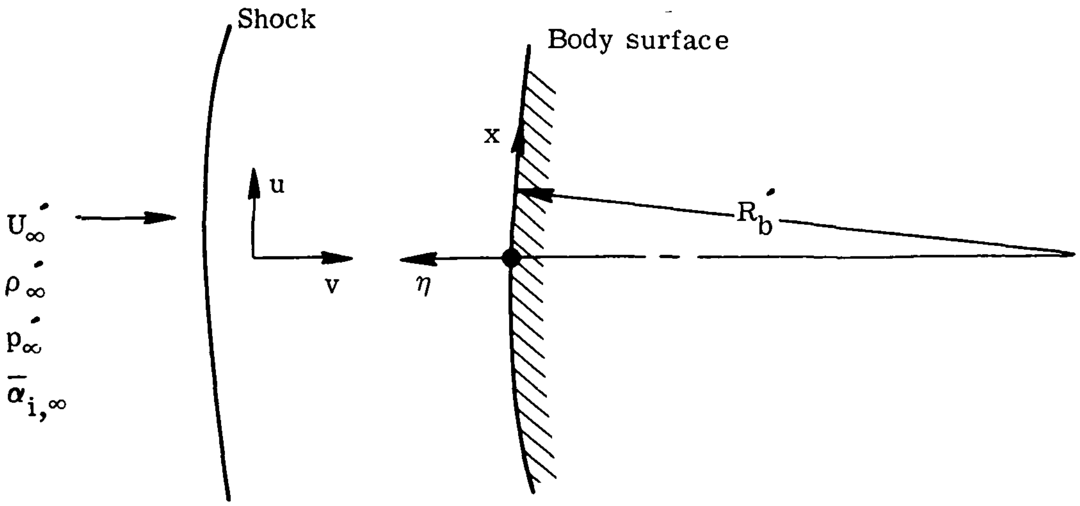

Figure 2.- Flow-field coordinate system in the transformed coordinates.

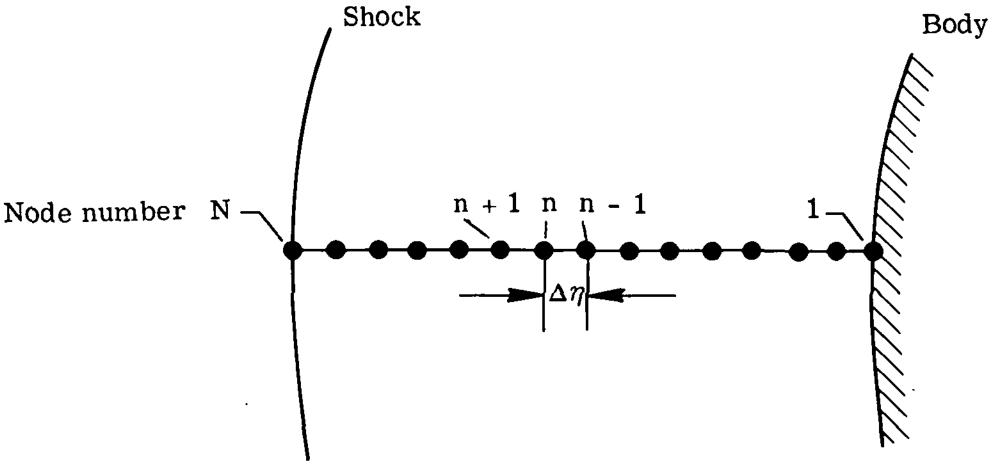

Figure 3.- Finite-difference network. (Nodal points are equally spaced in η.)

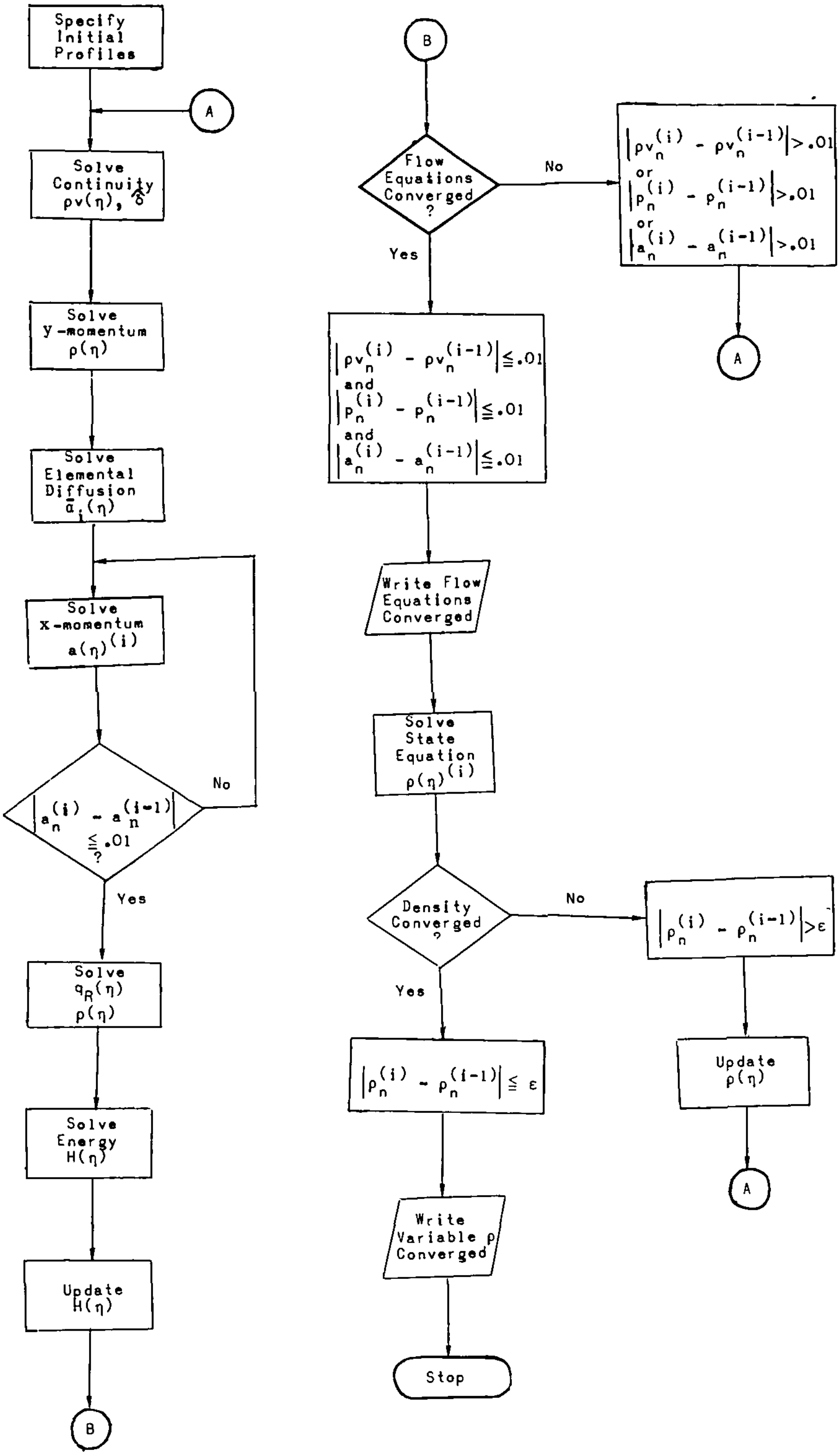

Figure 4.- Flow diagram of the overall solution procedure.

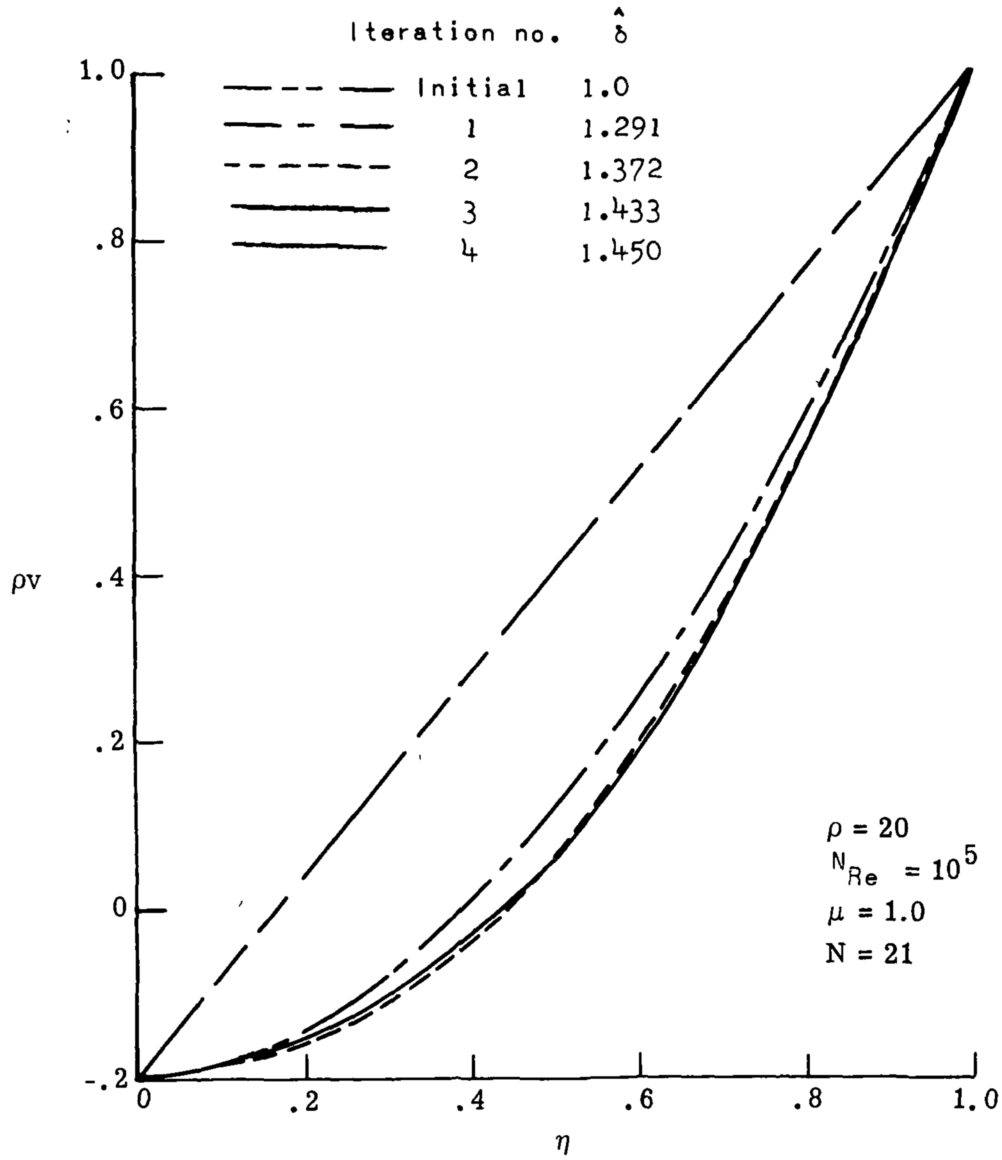

(a) Continuity equation ρv.

Figure 5.- Convergence behavior of a typical constant-density solution.

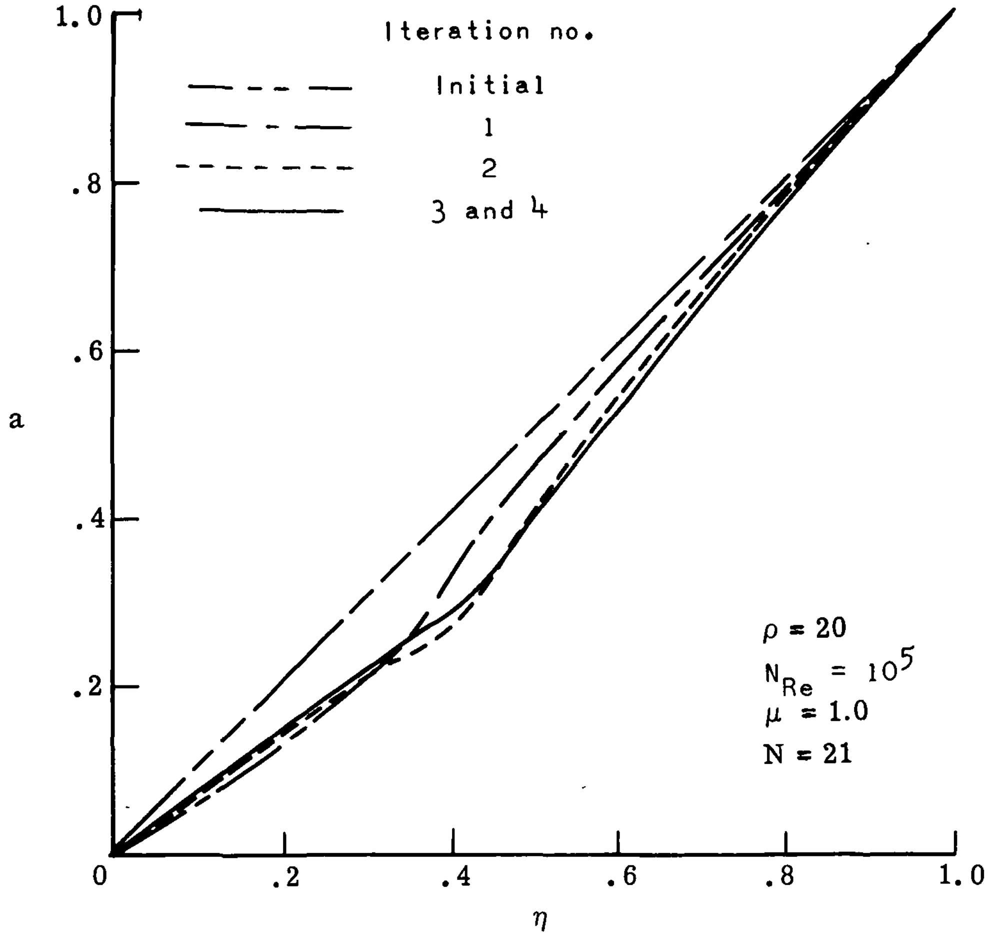

(b) x-momentum equation a.

Figure 5.- Concluded.

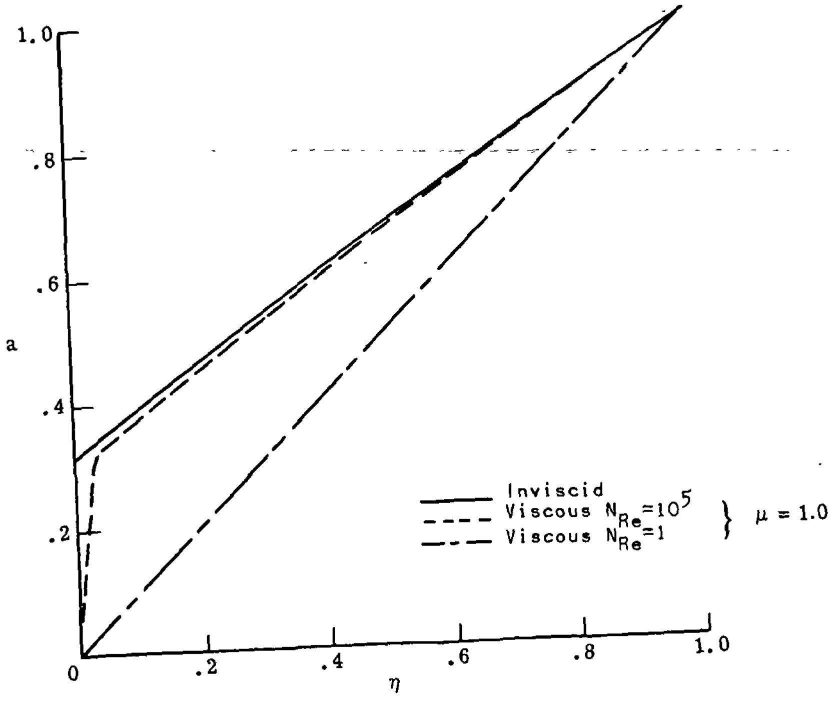

(a) Velocity-gradient distributions.

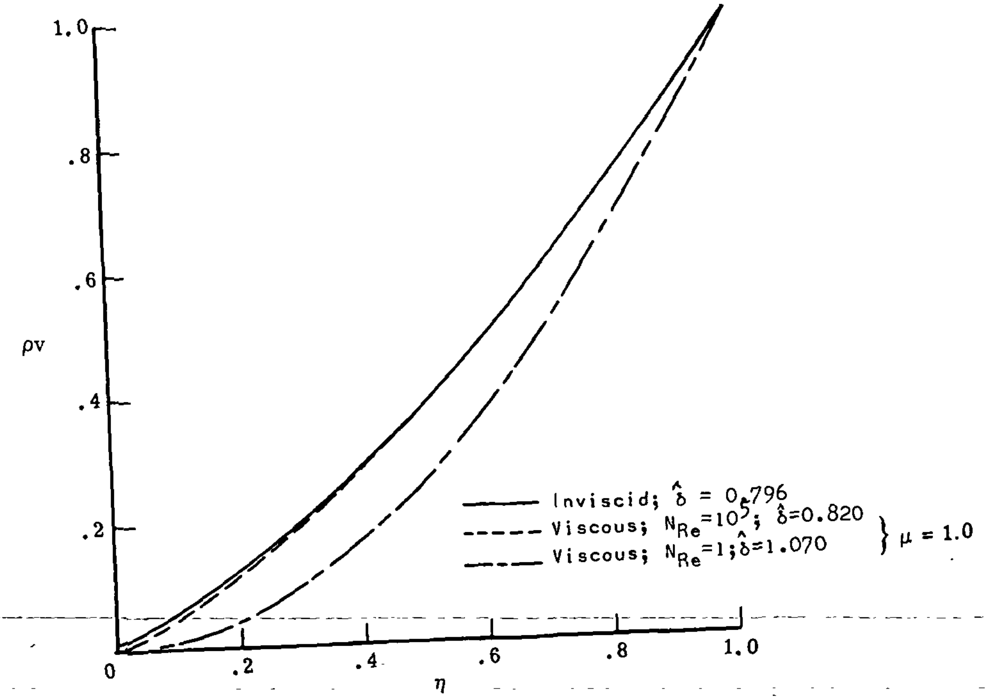

(b) Mass-flux distributions.

Figure 6.- Constant-density solutions for inviscid and viscous flows without blowing. $\rho = 20$.

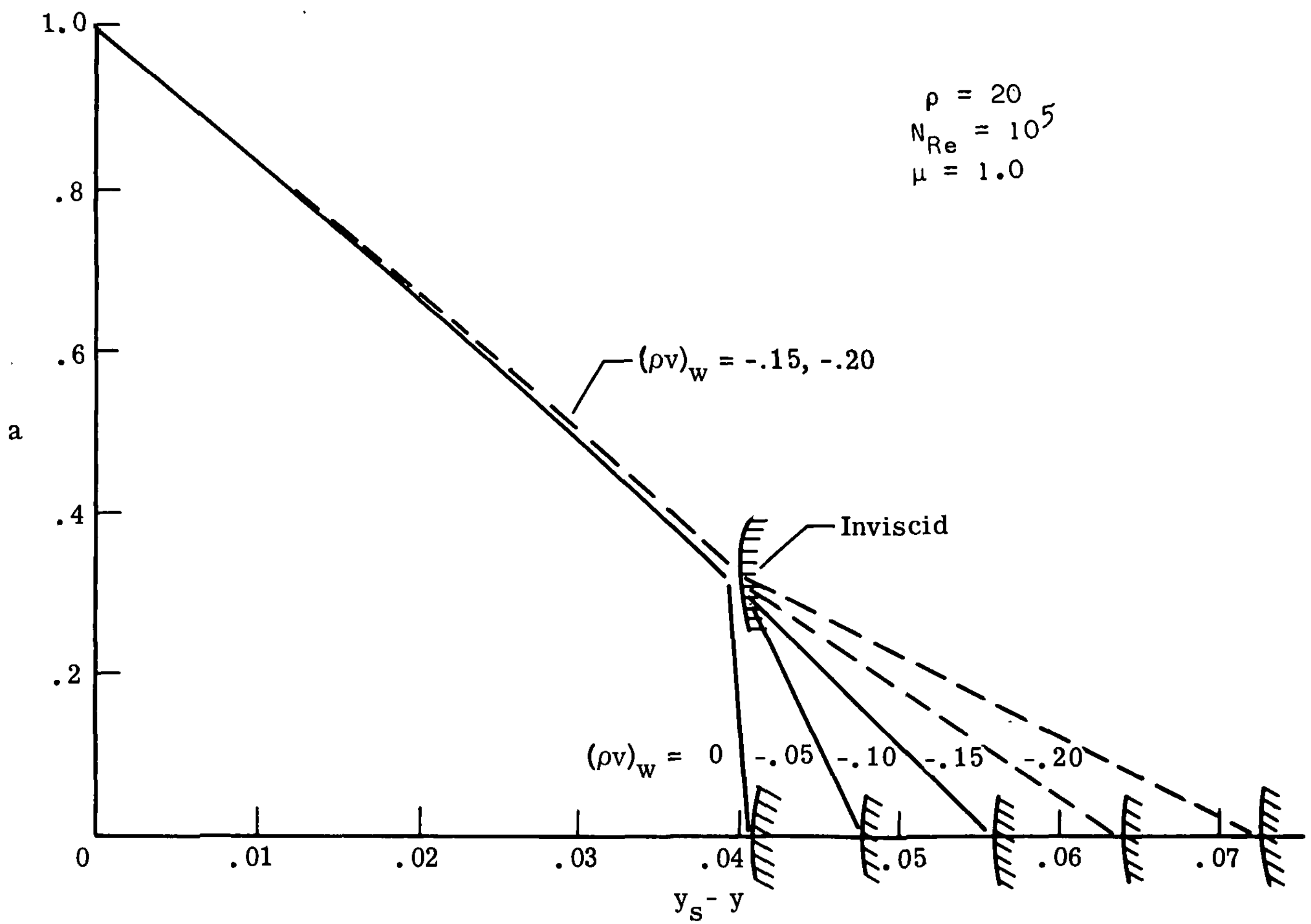

Figure 7.- Influence of blowing rate on velocity gradient for the constant-density solutions.

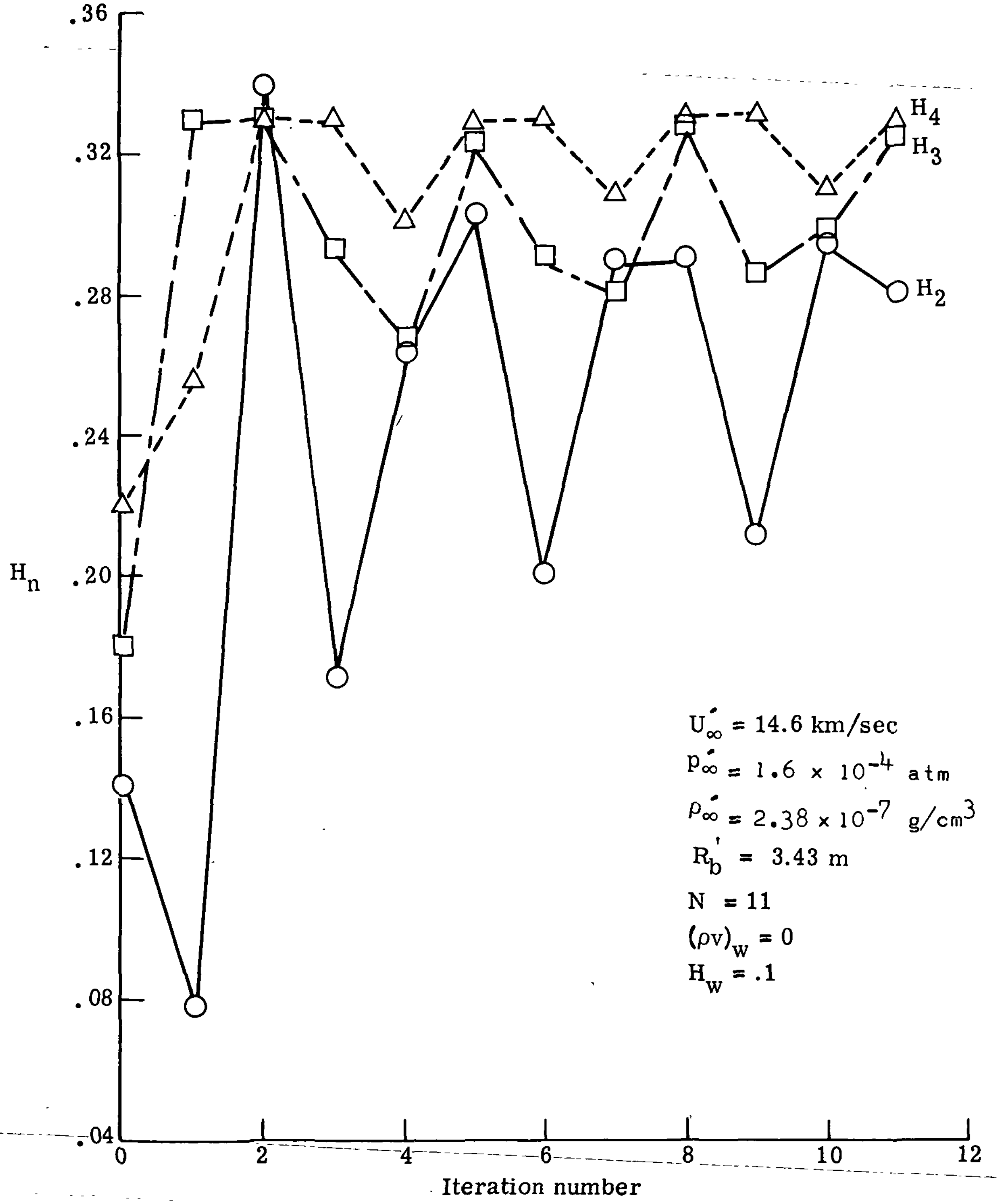

Figure 8.- Convergence behavior of the variable-density solution. Equilibrium air without radiation.

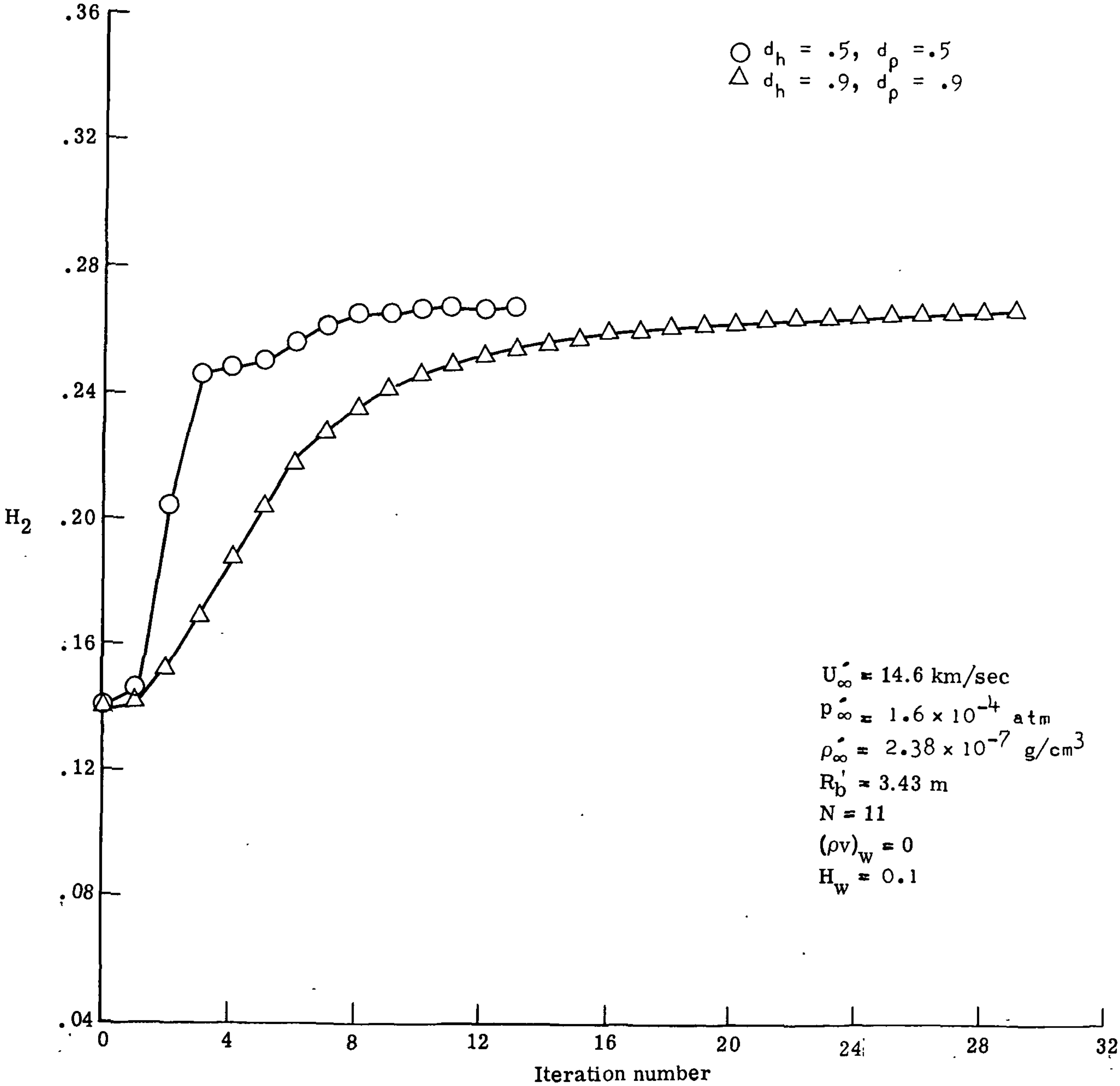

(a) Enthalpy.

Figure 9.- Effect of profile damping on the convergence of the variable-density solution. Equilibrium air without radiation.

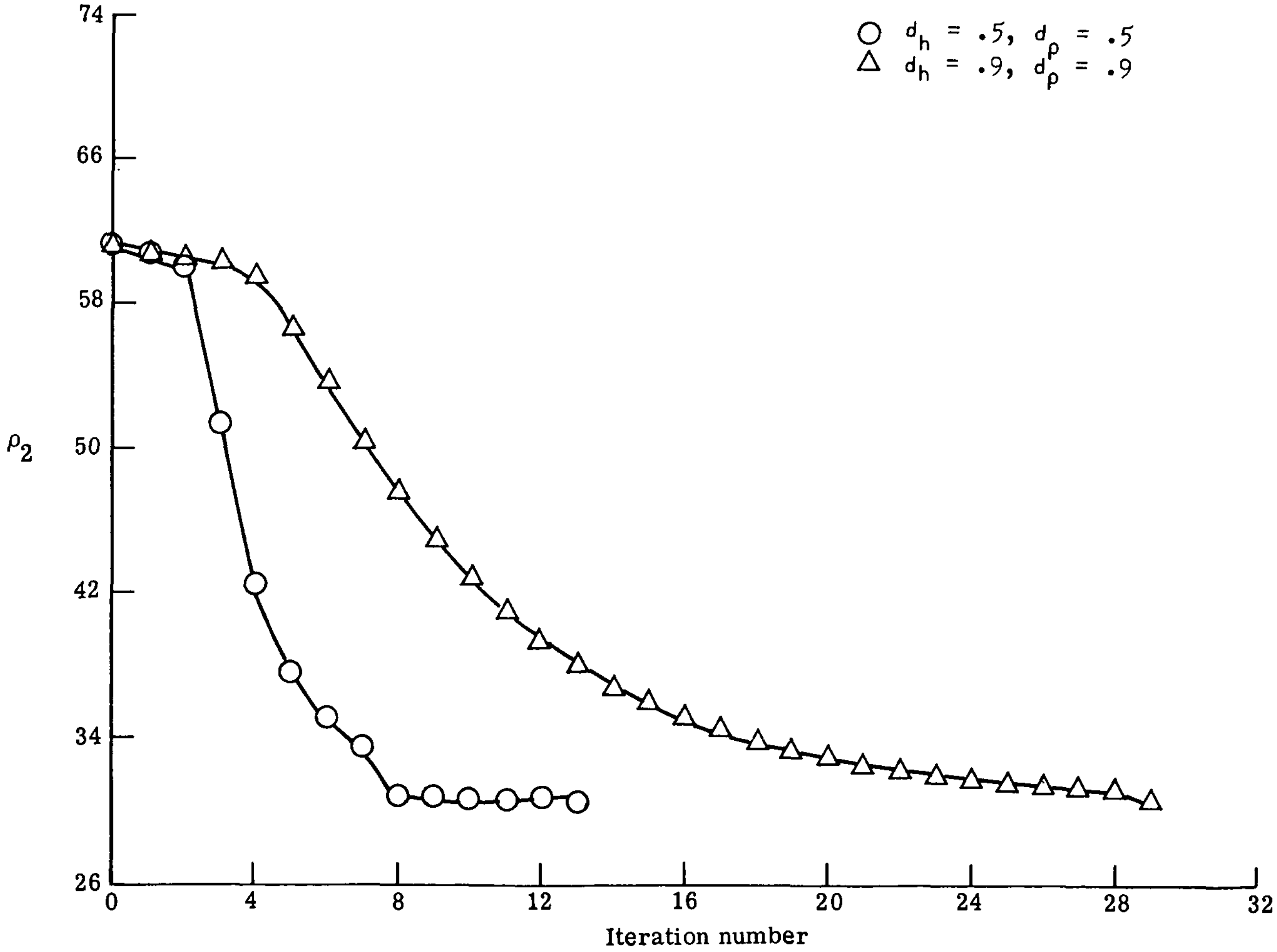

(b) Density.

Figure 9.- Concluded.

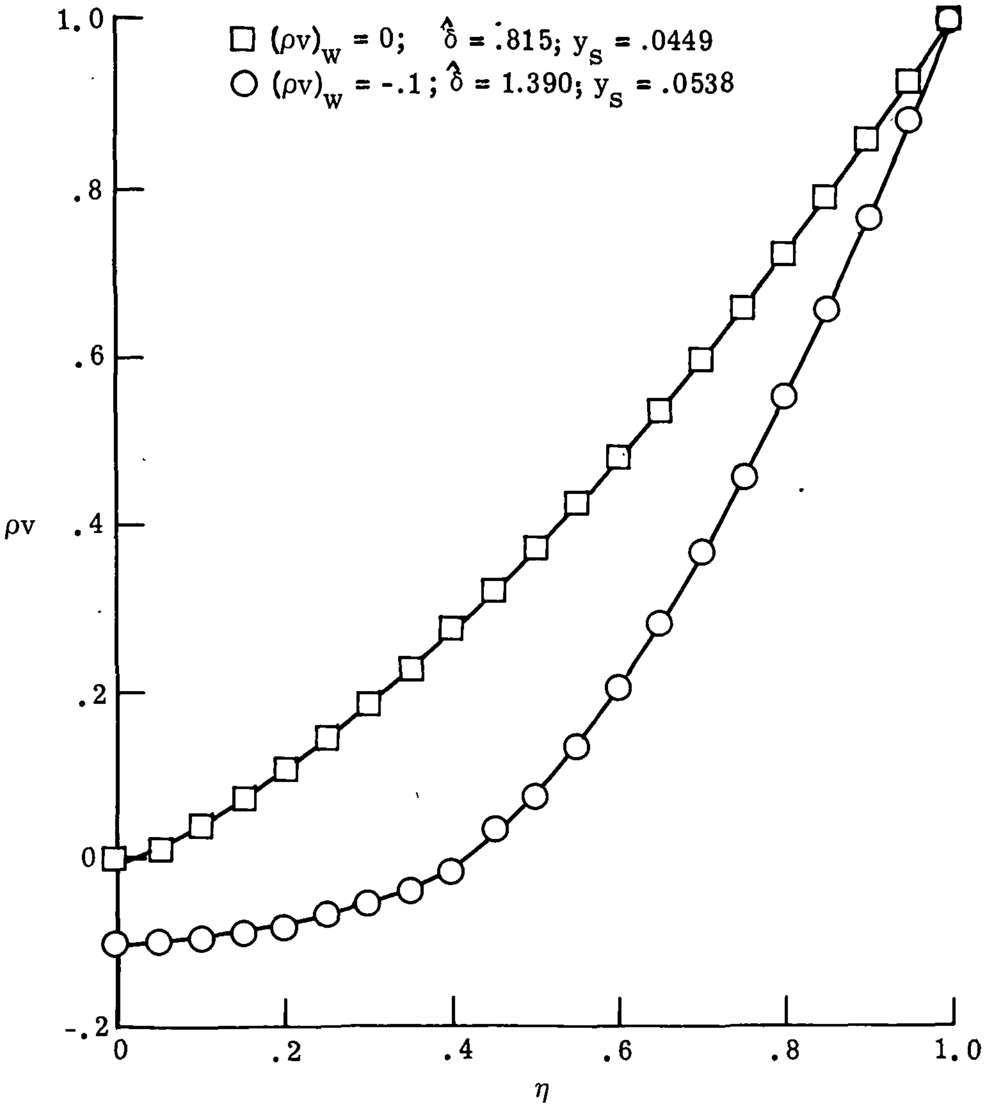

(a) Continuity equation.

Figure 10.- Equilibrium-air solutions without radiation.

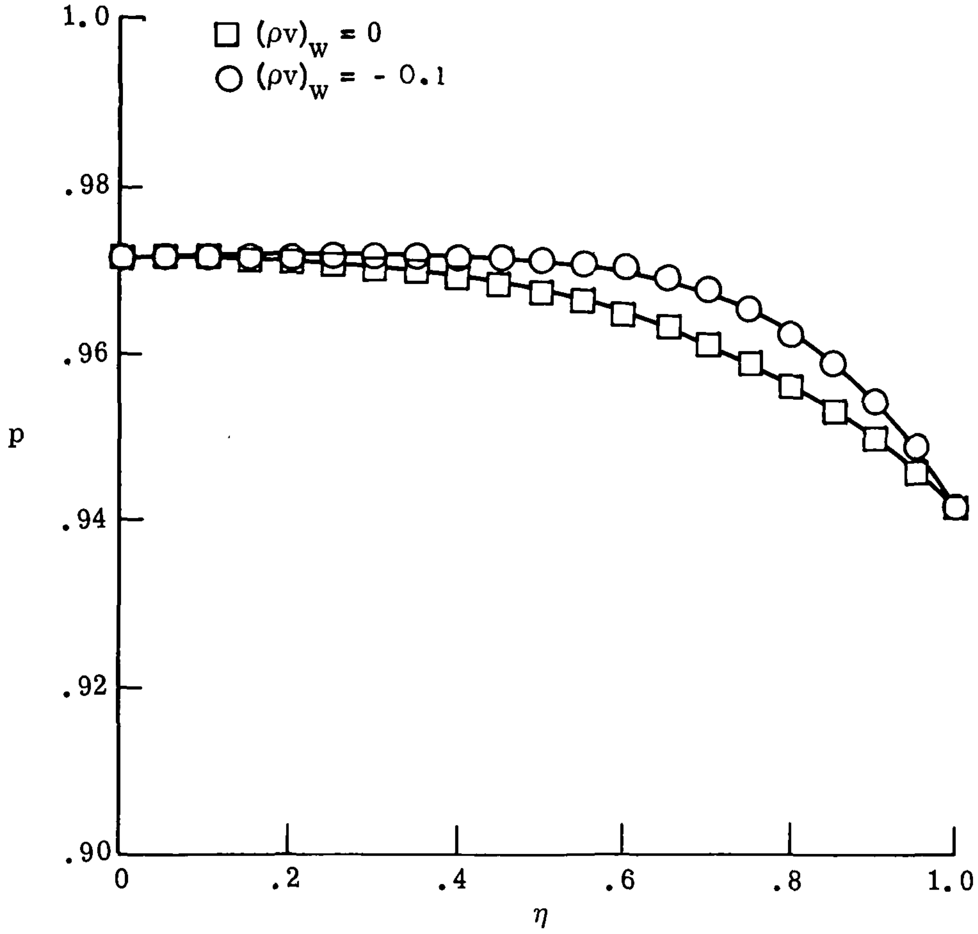

(b) y-momentum equation.

Figure 10.- Continued.

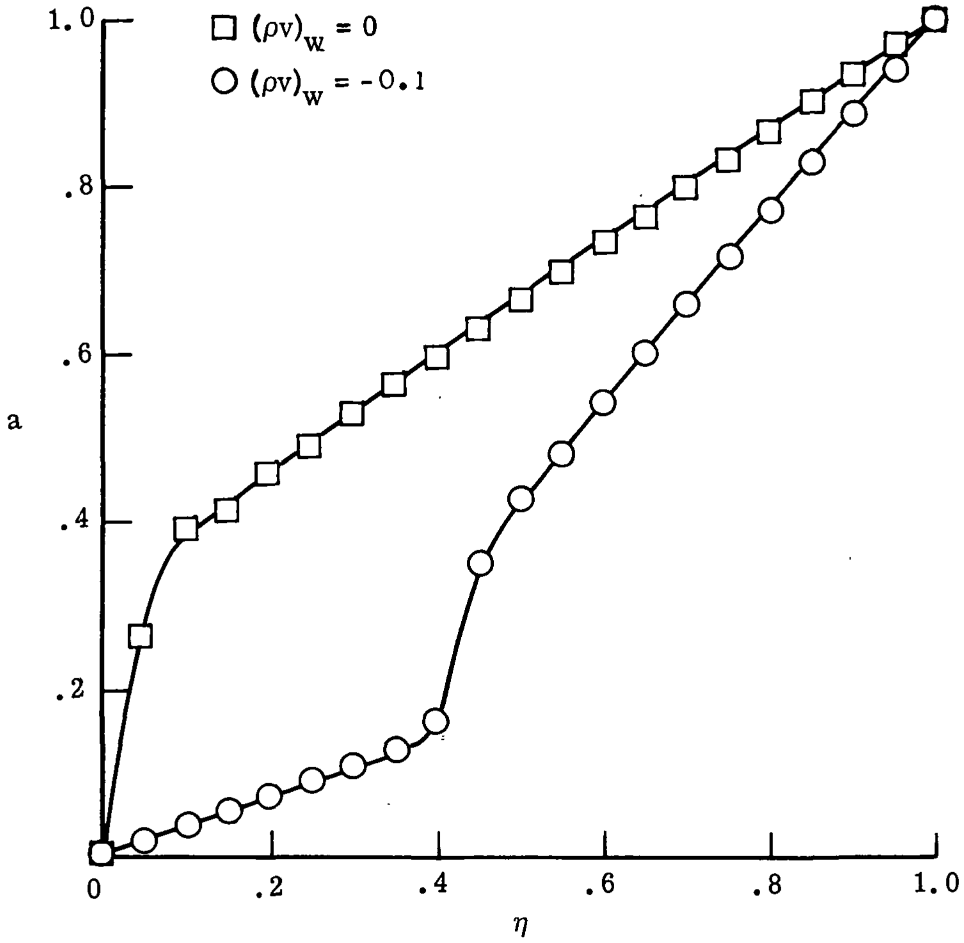

(c) x-momentum equation.

Figure 10.- Continued.

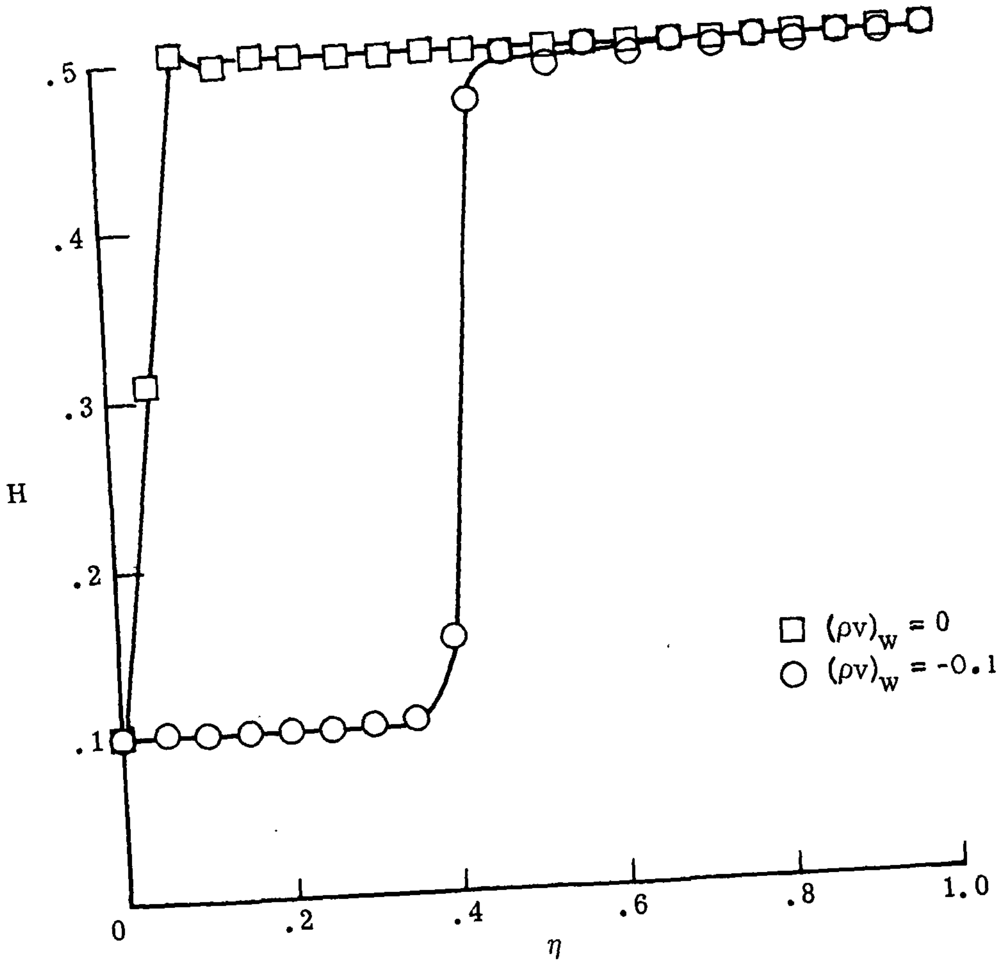

(d) Energy equation.

Figure 10.- Continued.

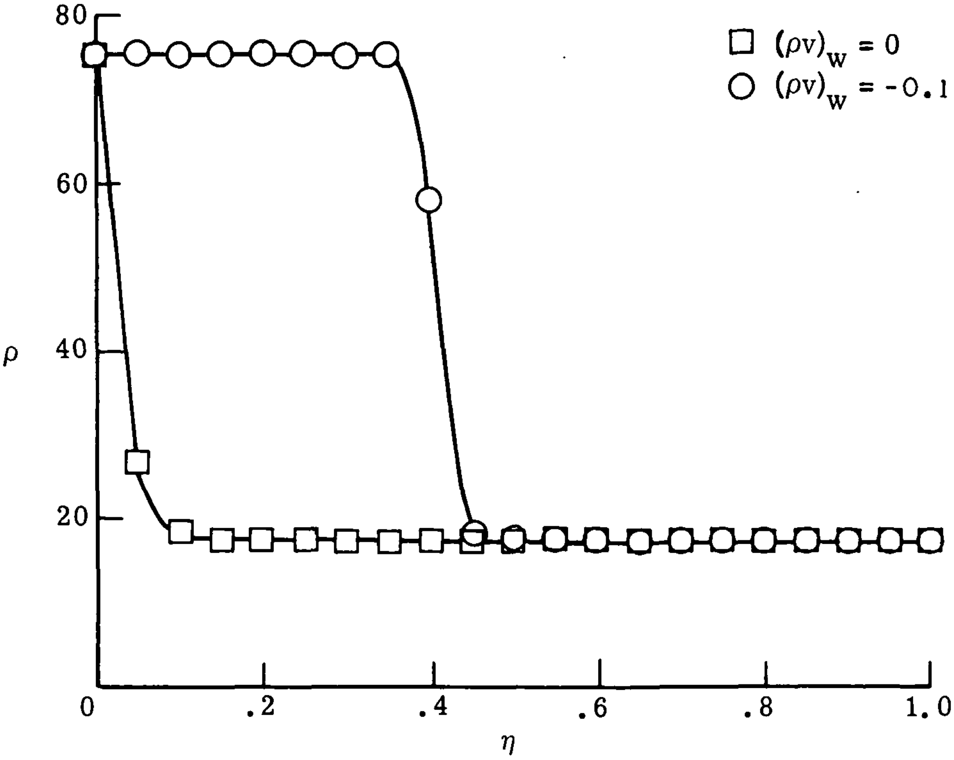

(e) Equation of state.

Figure 10.- Concluded.

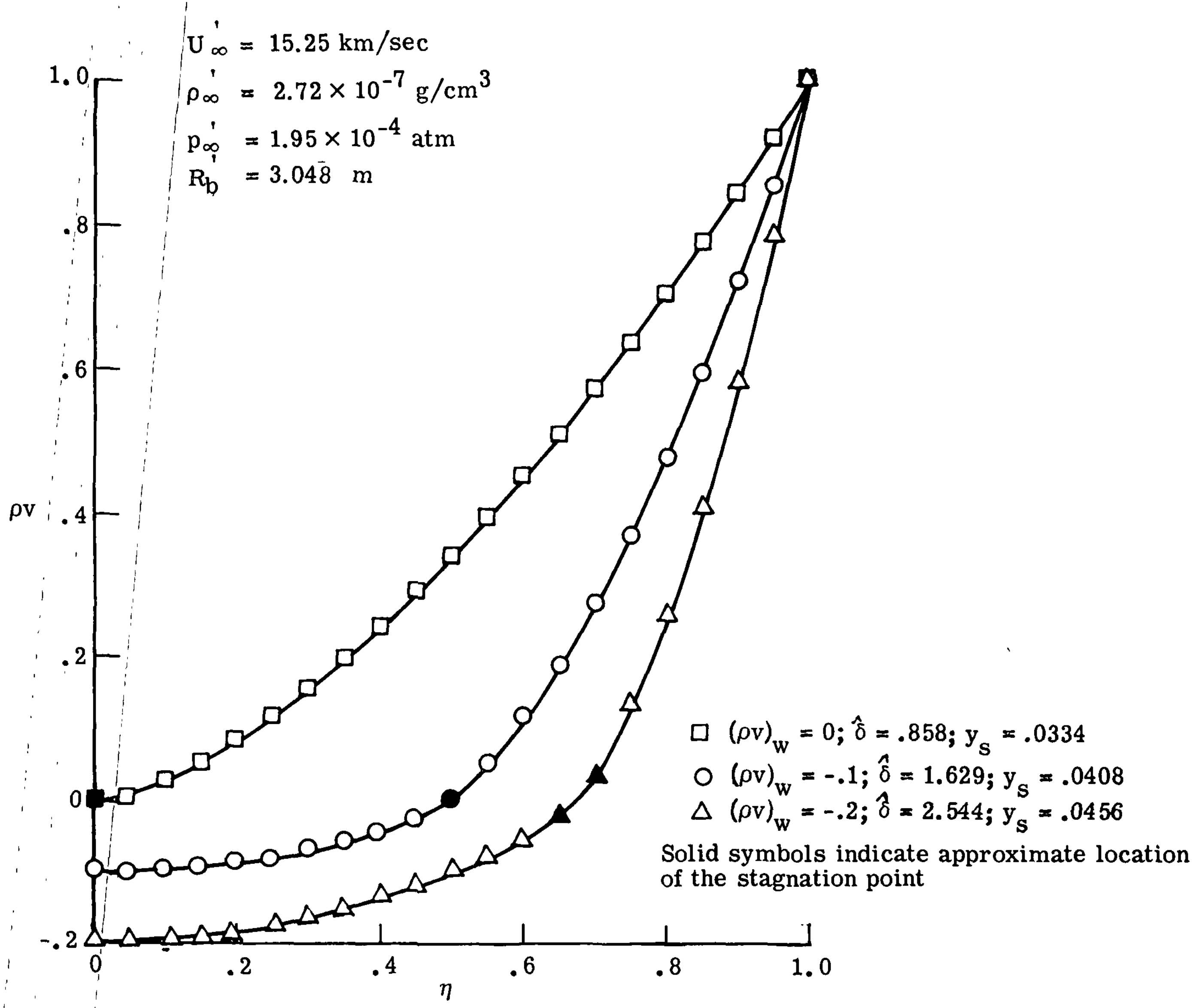

(a) Continuity equation.

Figure 11.- Equilibrium-air solutions with radiation included.

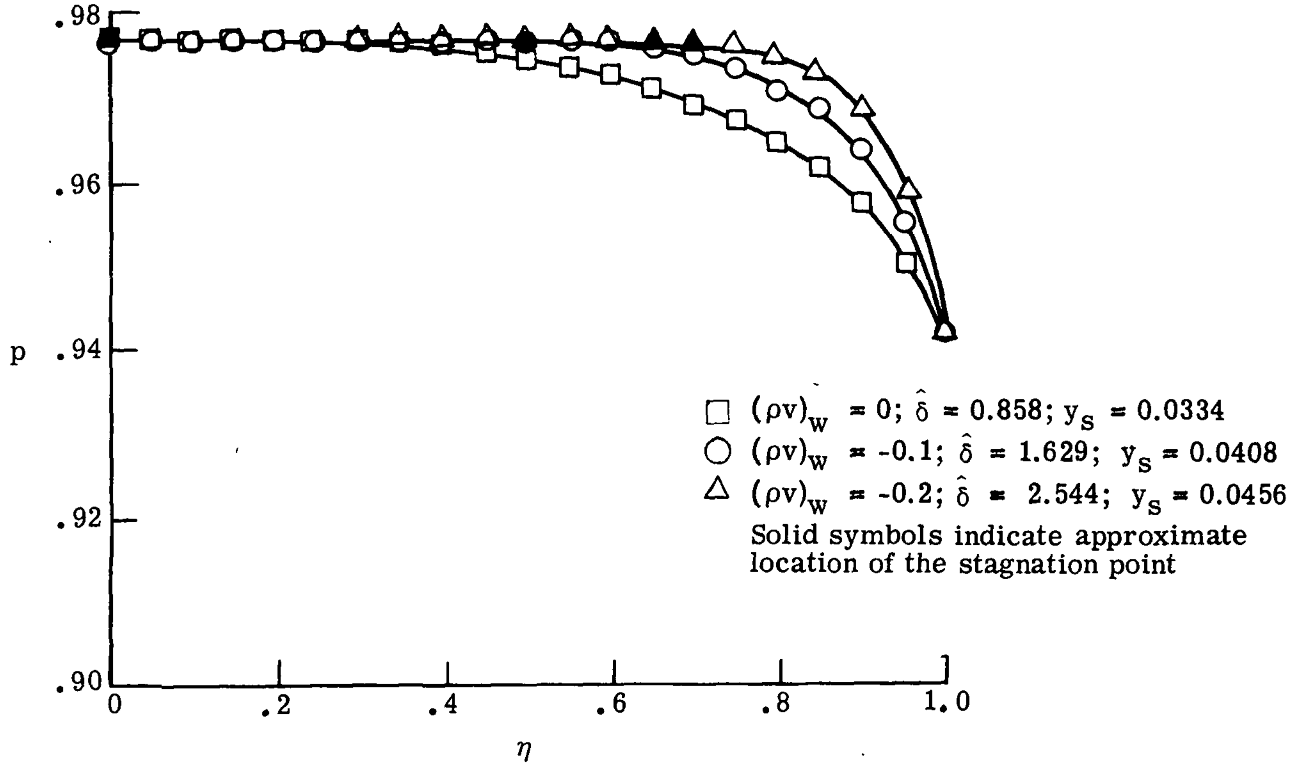

(b) y-momentum equations.

Figure 11.- Continued.

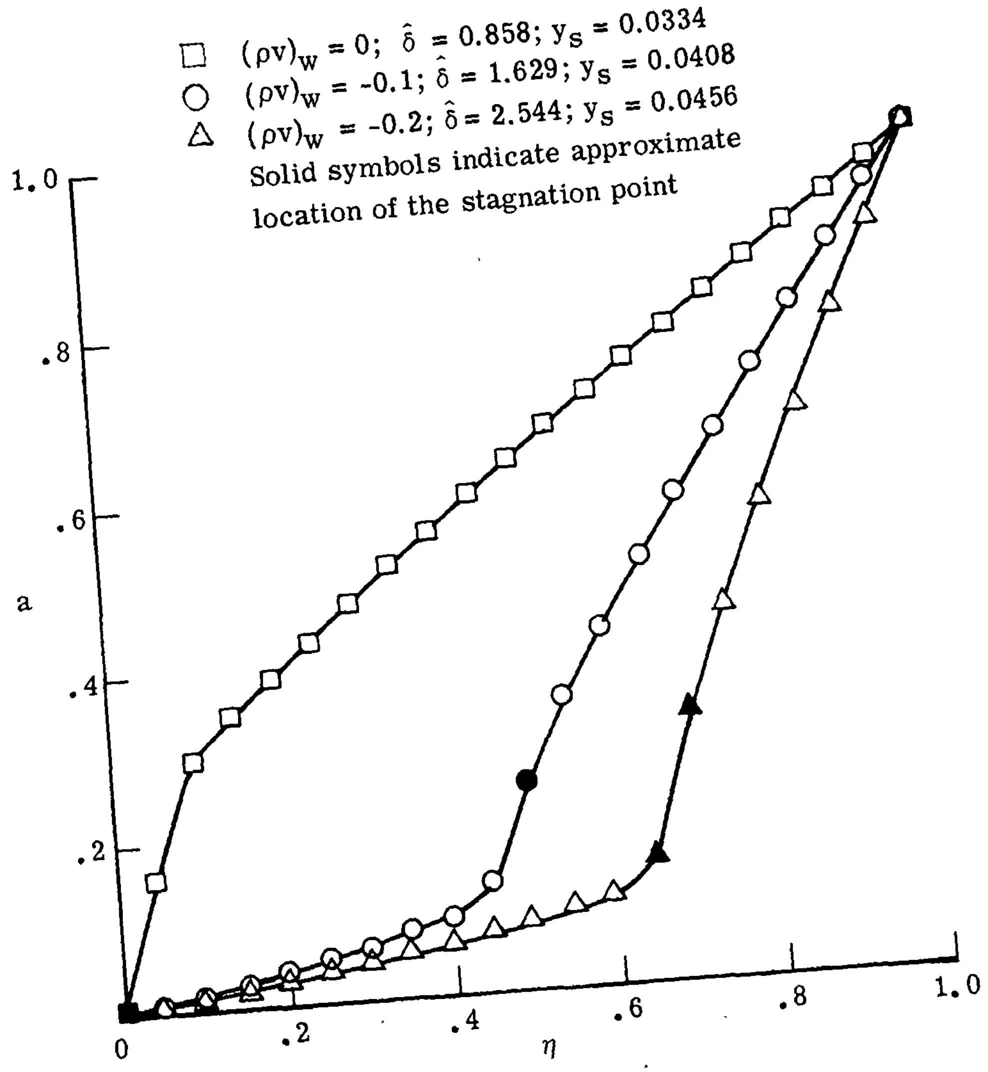

(c) x-momentum equation.

Figure 11.- Continued.

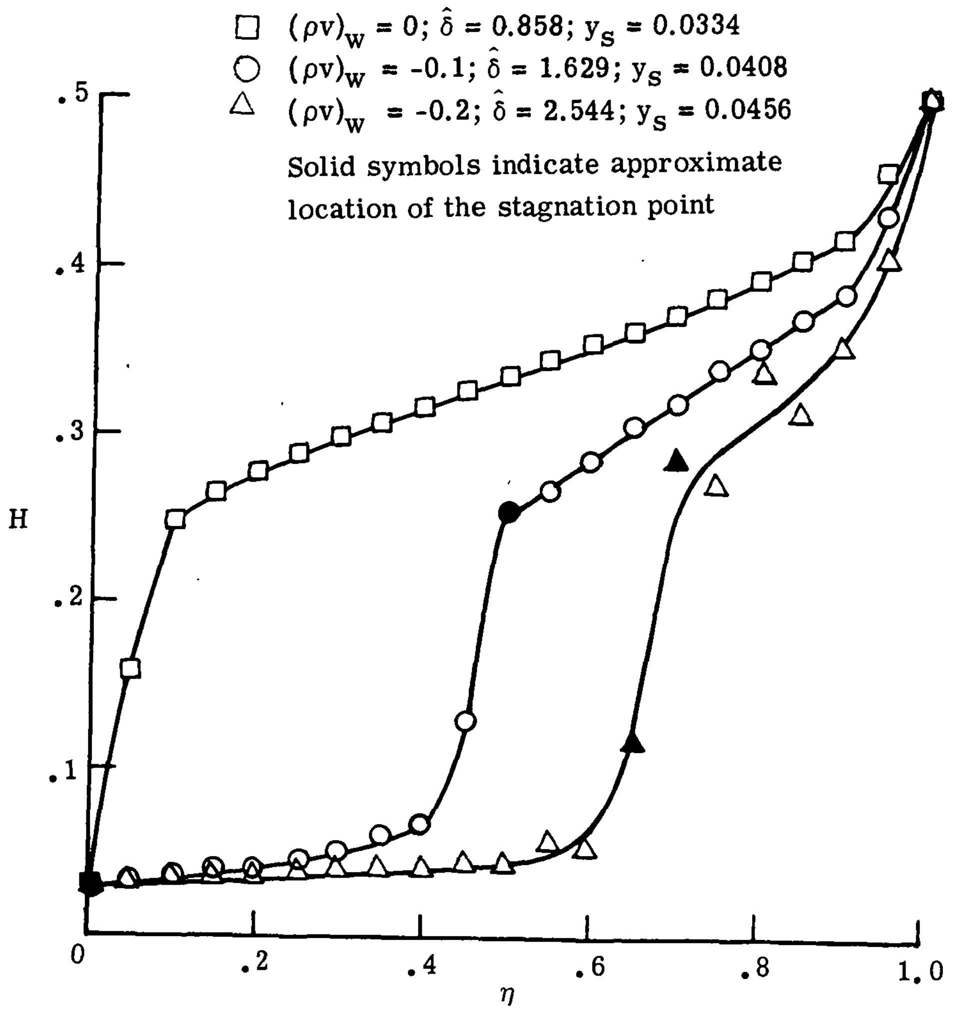

(d) Energy equation. (Central-difference form of convective term in energy equation used to generate these solutions.)

Figure 11.- Continued.

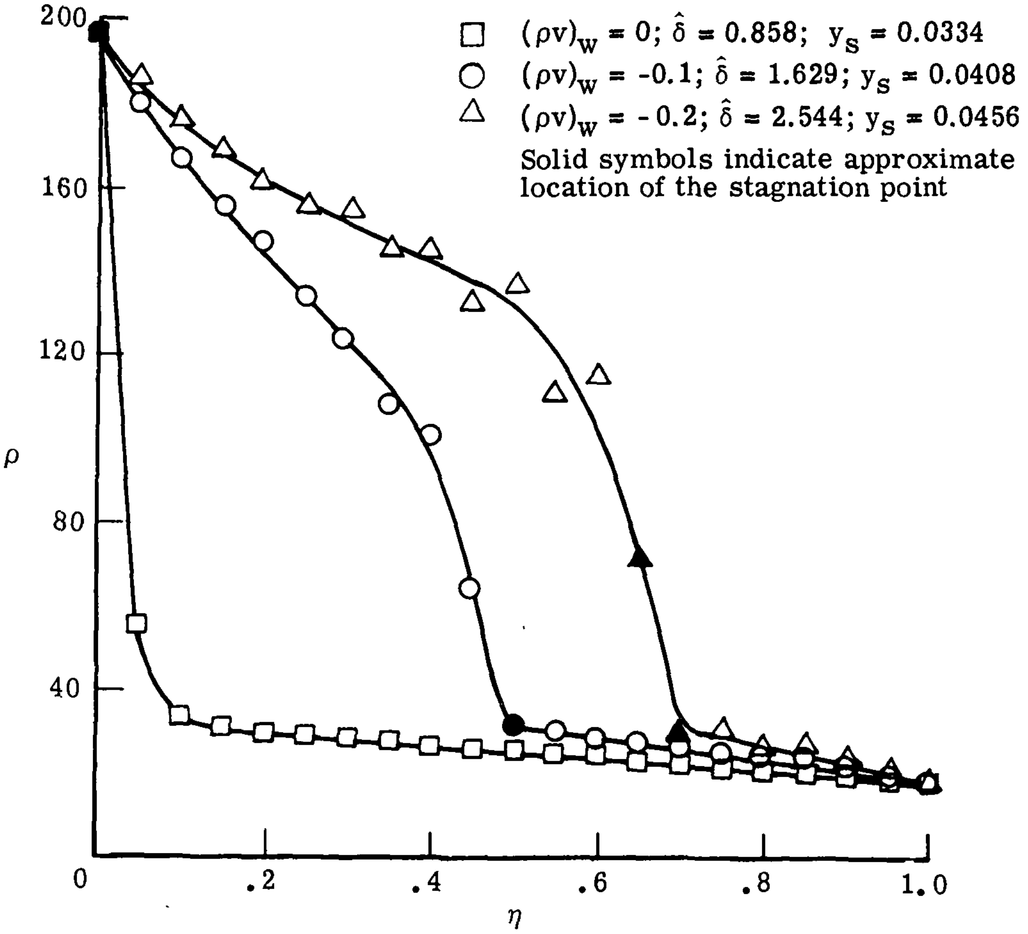

(e) Equation of state.

Figure 11.- Continued.

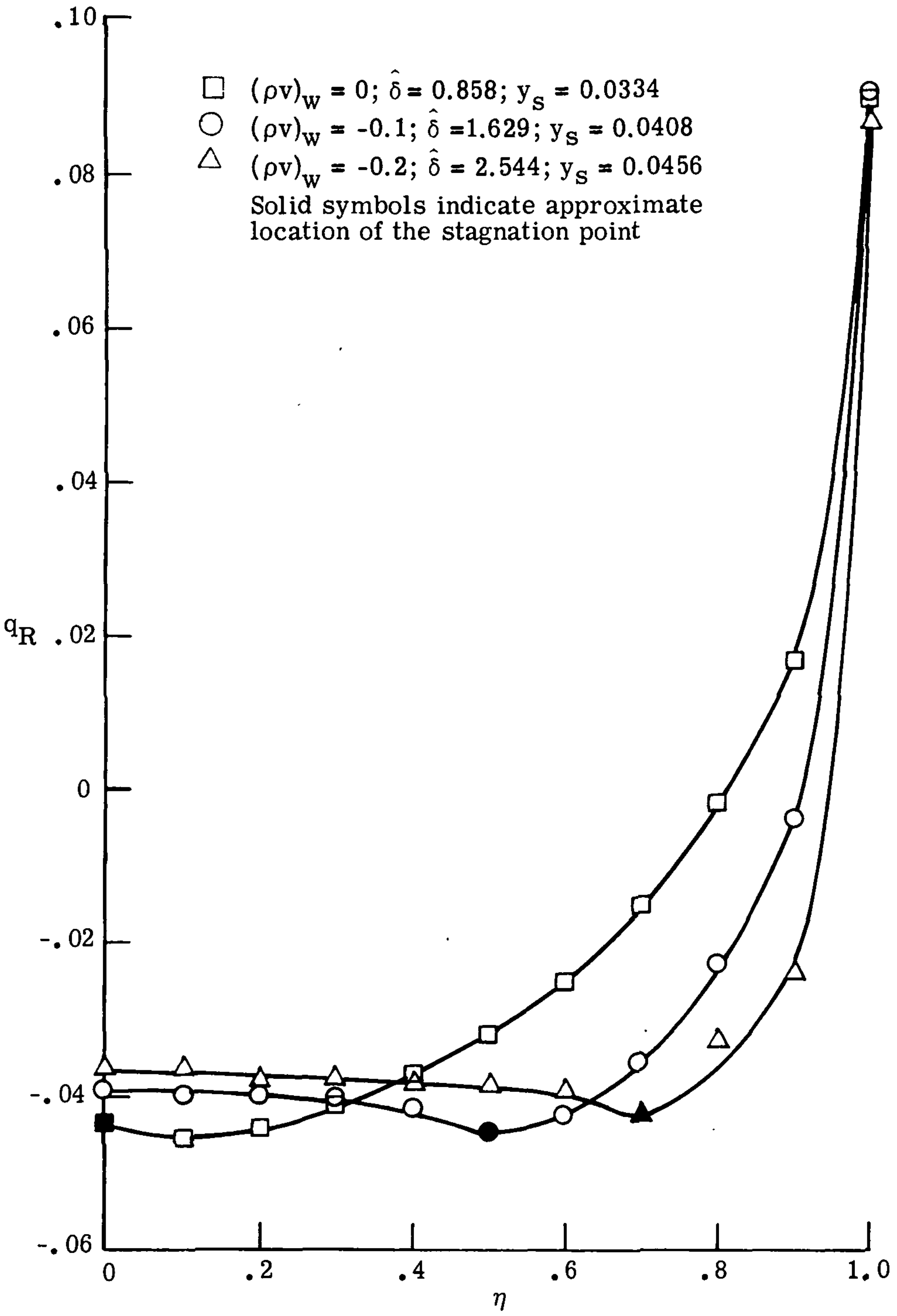

(f) Radiative heat flux.

Figure 11.- Concluded.

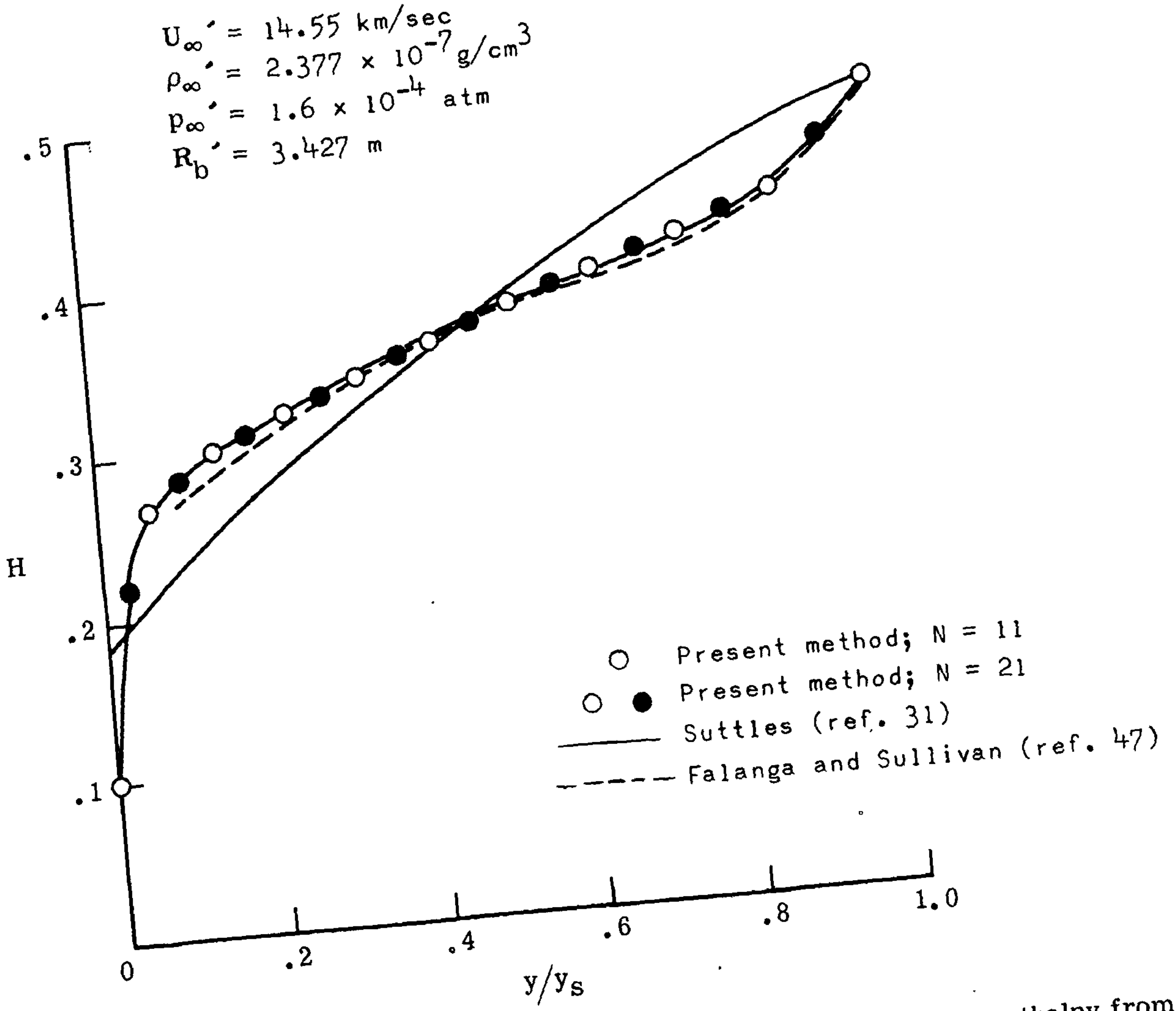

Figure 12.- Comparison of enthalpy profile along stagnation line with enthalpy from solutions for entire subsonic flow field. Equilibrium air with radiation and without blowing.

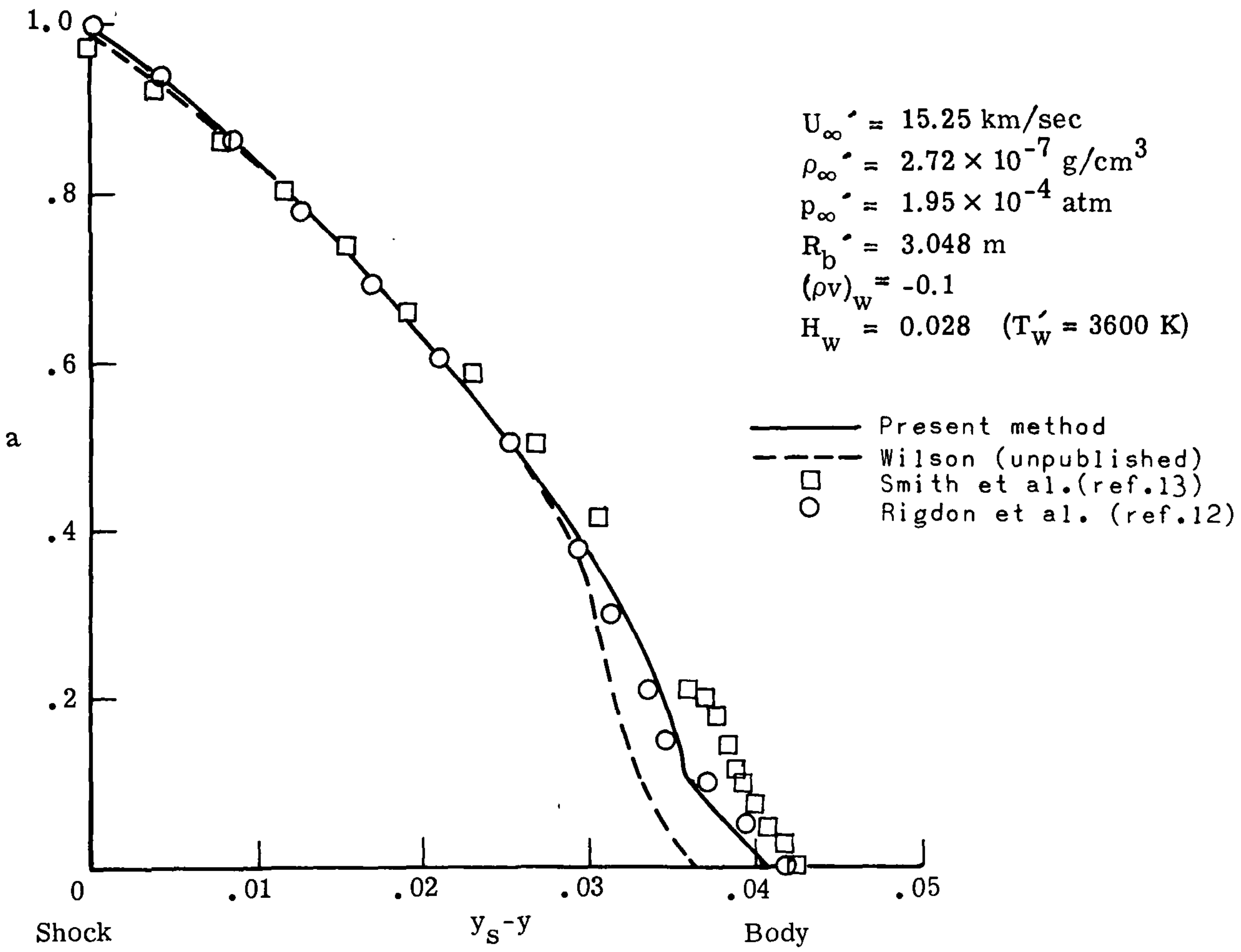

(a) Tangential velocity gradient.

Figure 13.- Comparison of equilibrium-air solutions for radiation and air-to-air injection.

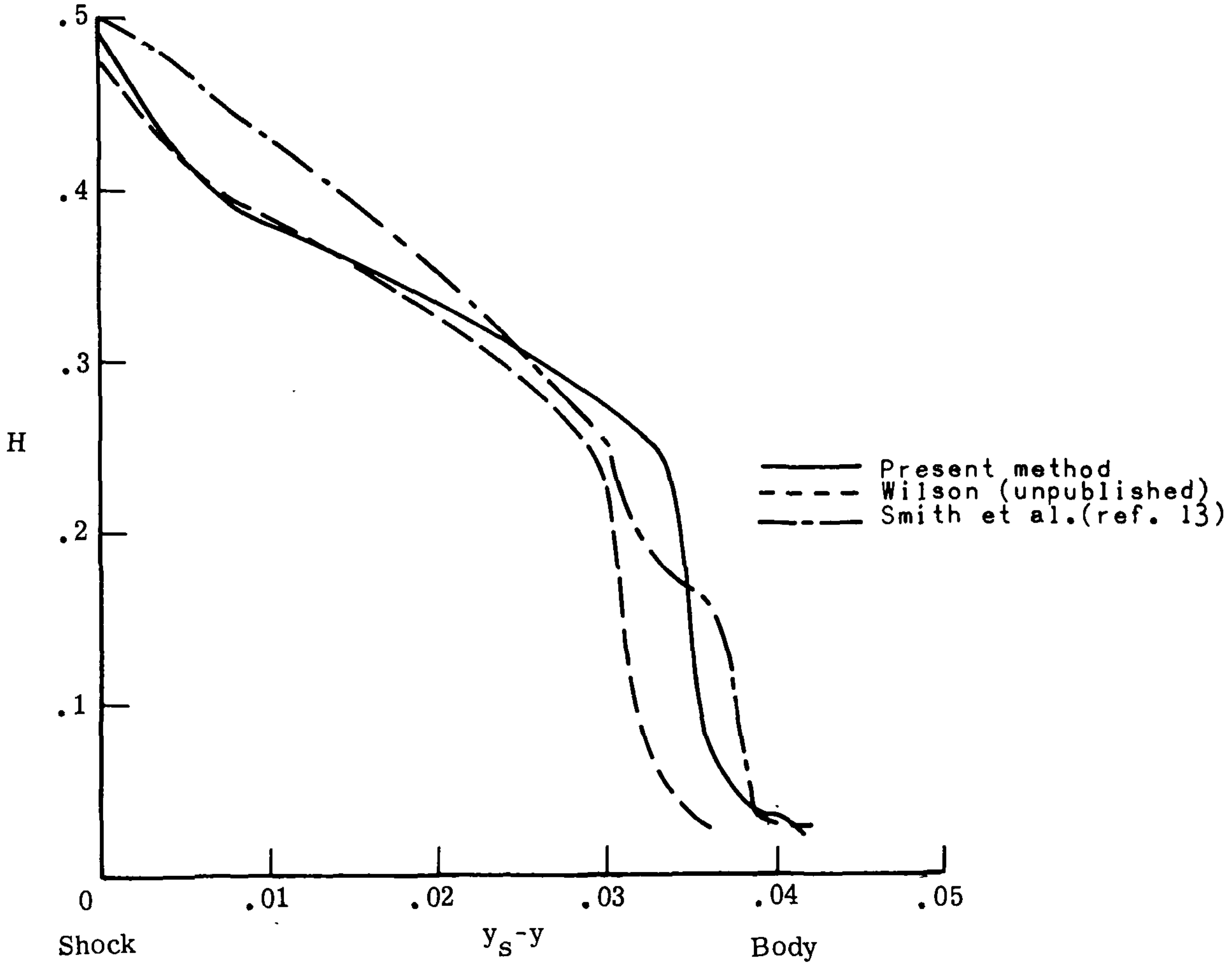

(b) Total enthalpy.

Figure 13.- Continued.

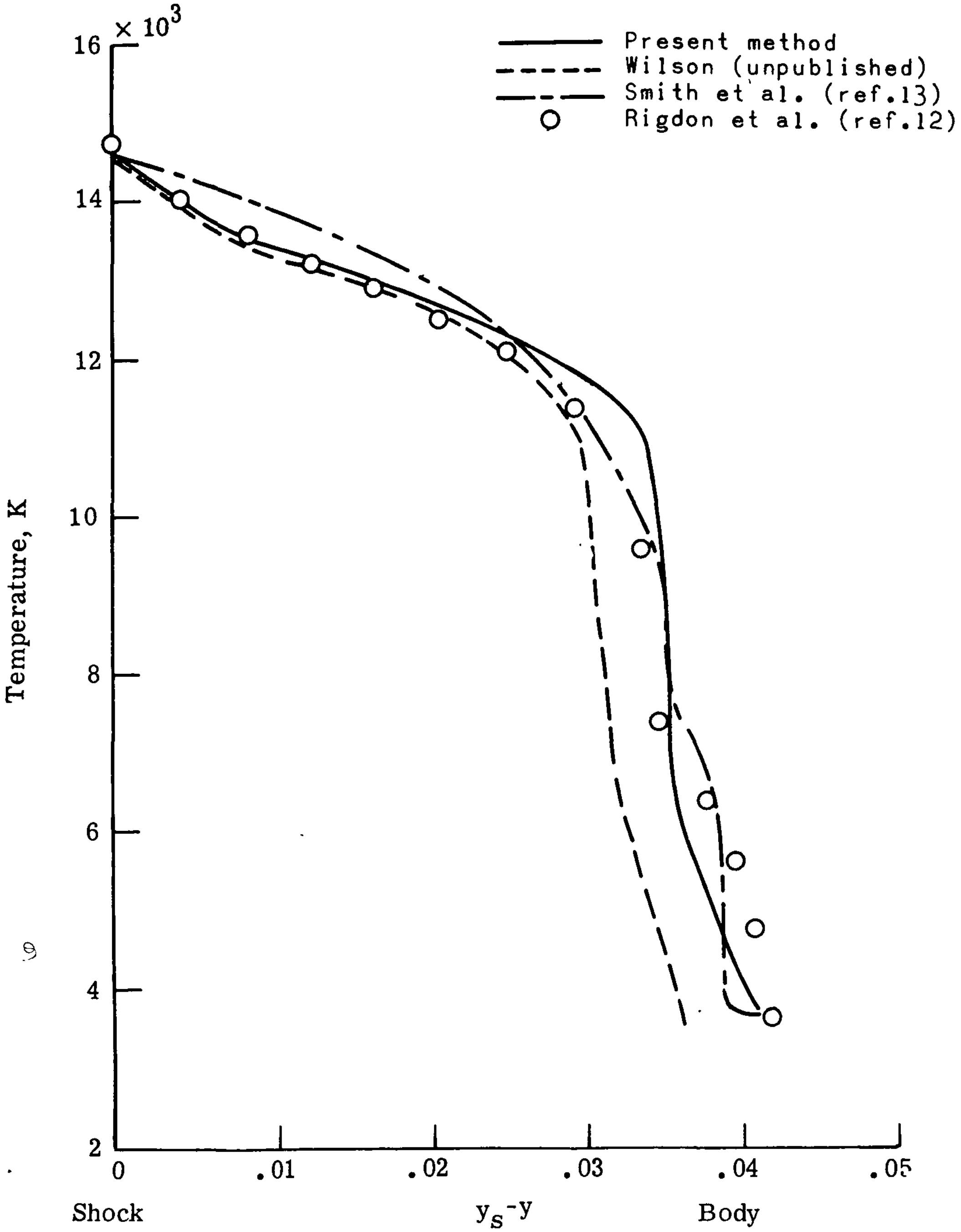

(c) Temperature.

Figure 13.- Continued.

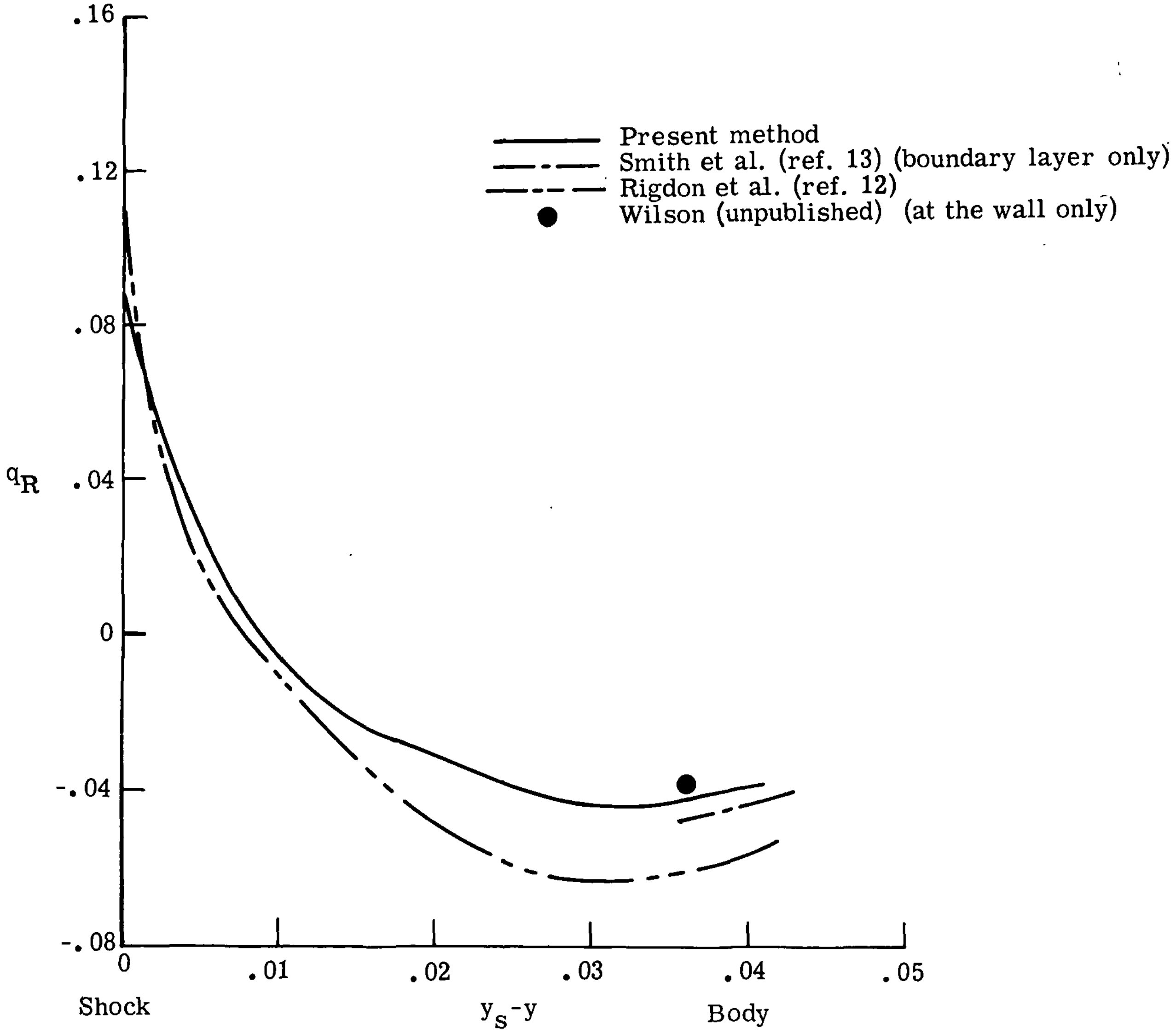

(d) Radiative heat flux.

Figure 13.- Concluded.

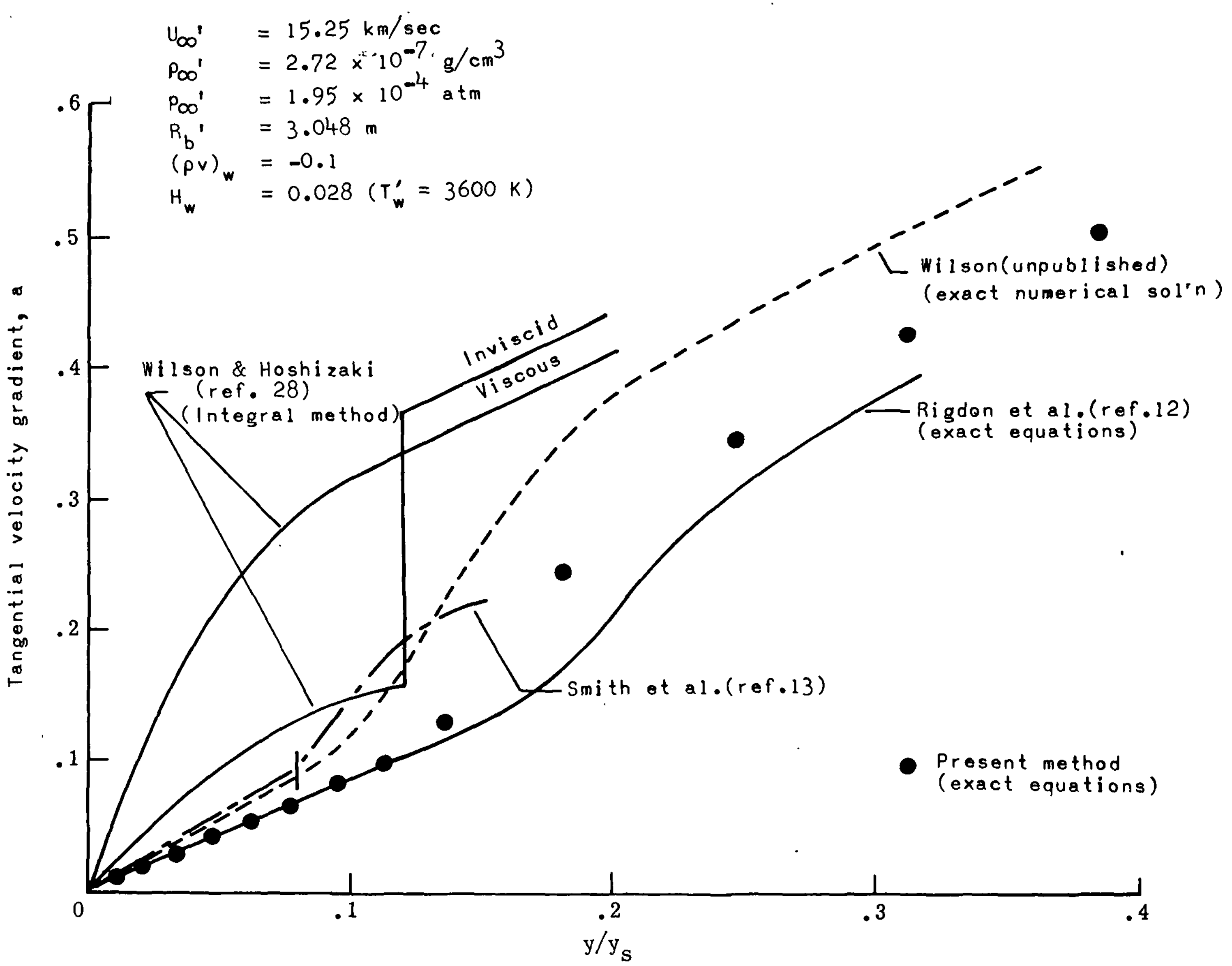

(a) Tangential velocity gradient.

Figure 14.- Detailed comparisons near the wall of existing equilibrium-air shock-layer solutions including radiation and air-to-air injection.

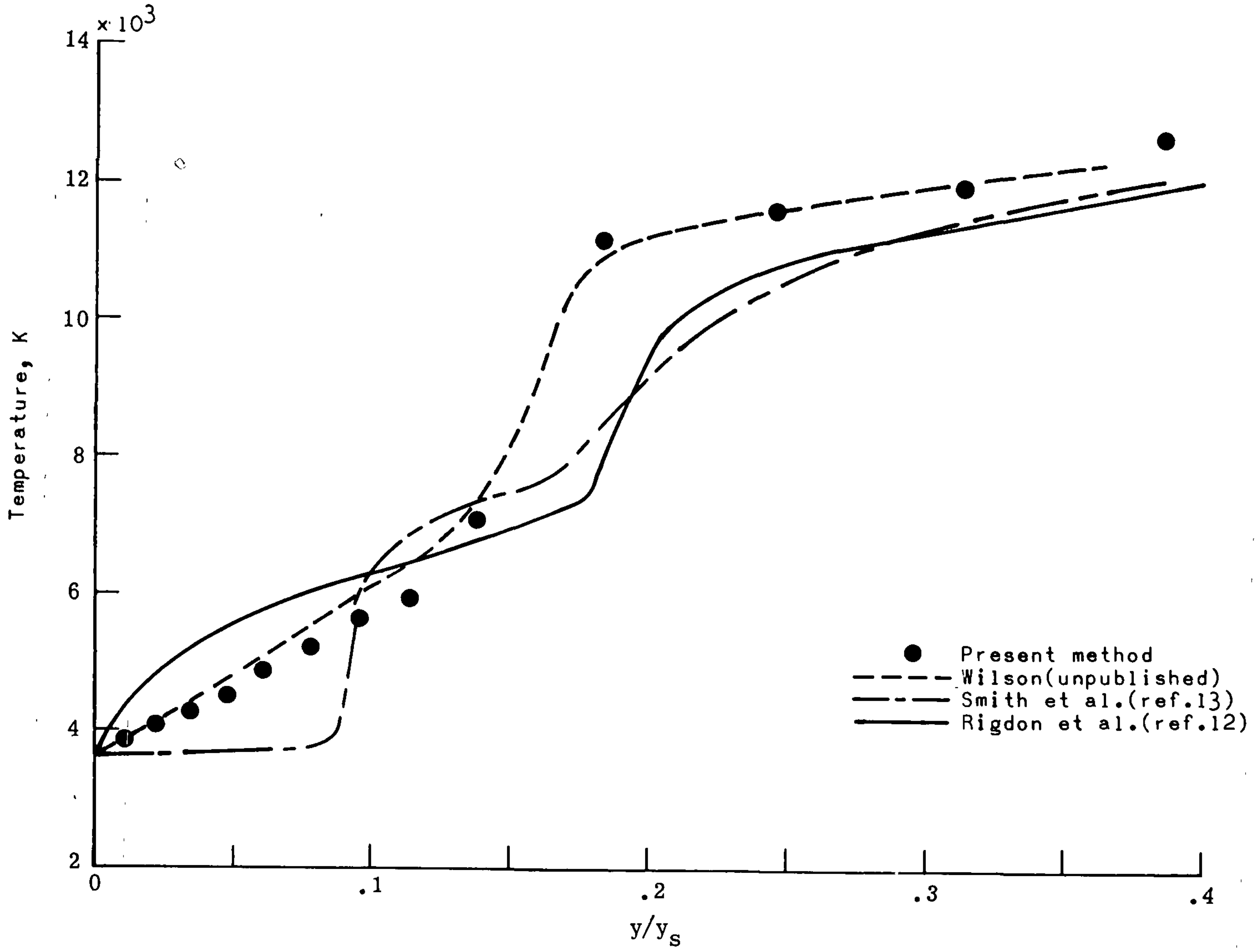

(b) Temperature.

Figure 14.- Concluded.

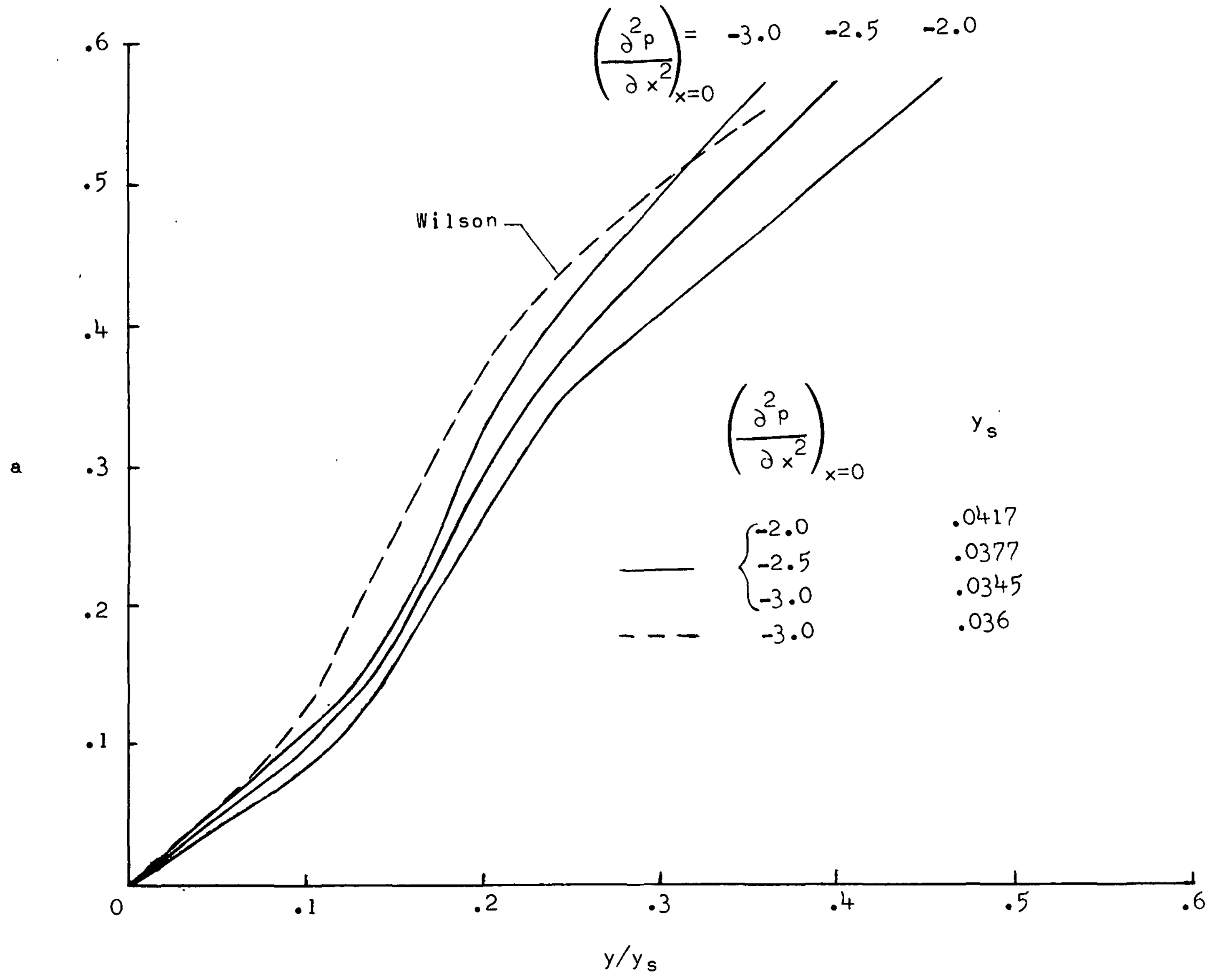

Figure 15.- Effect of pressure gradient on solution for tangential velocity gradient.

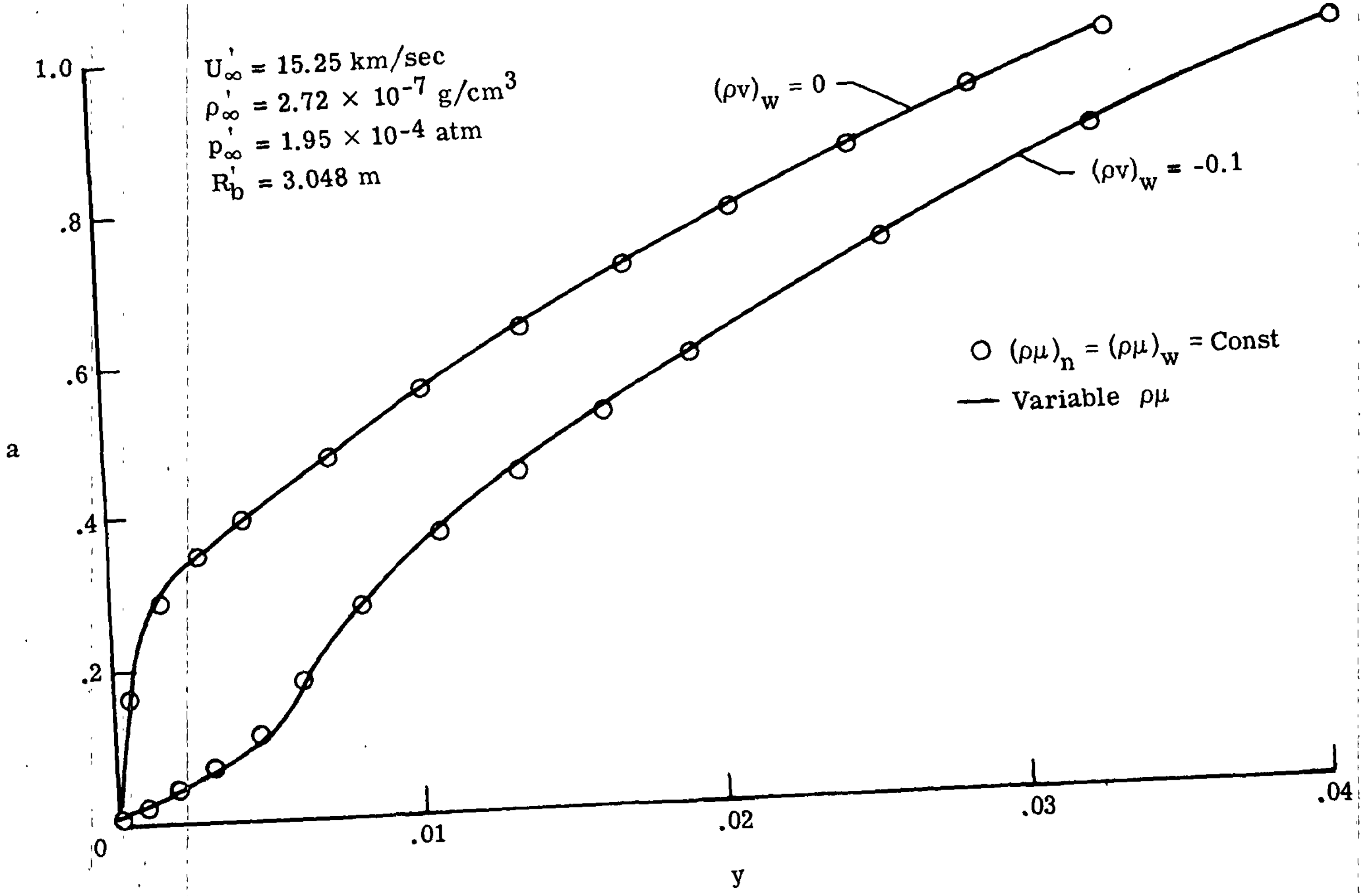

(a) Tangential velocity gradient.

Figure 16.- Effect of assuming constant product of density and viscosity on the solution.

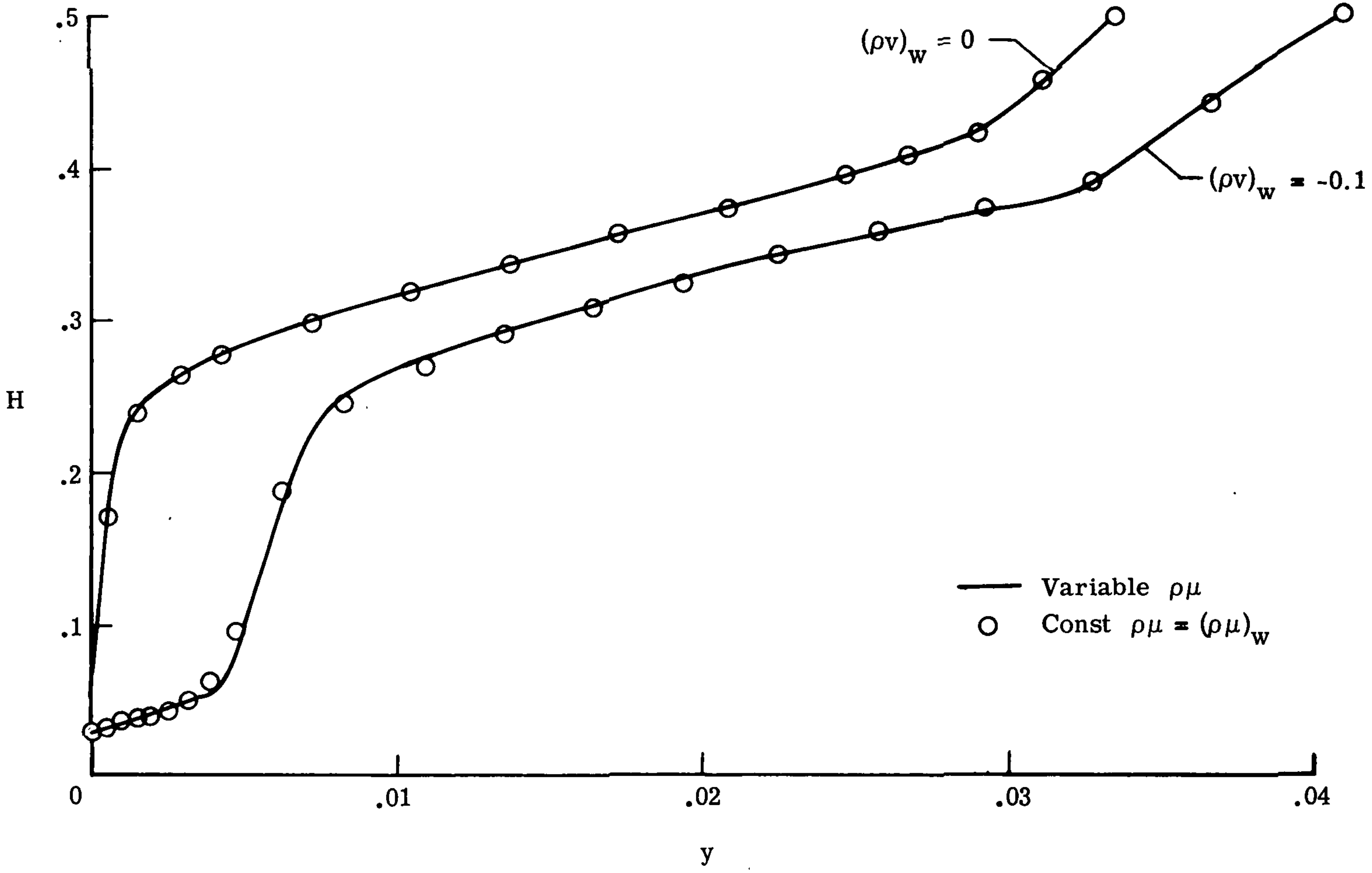

(b) Total enthalpy.

Figure 16.- Concluded.

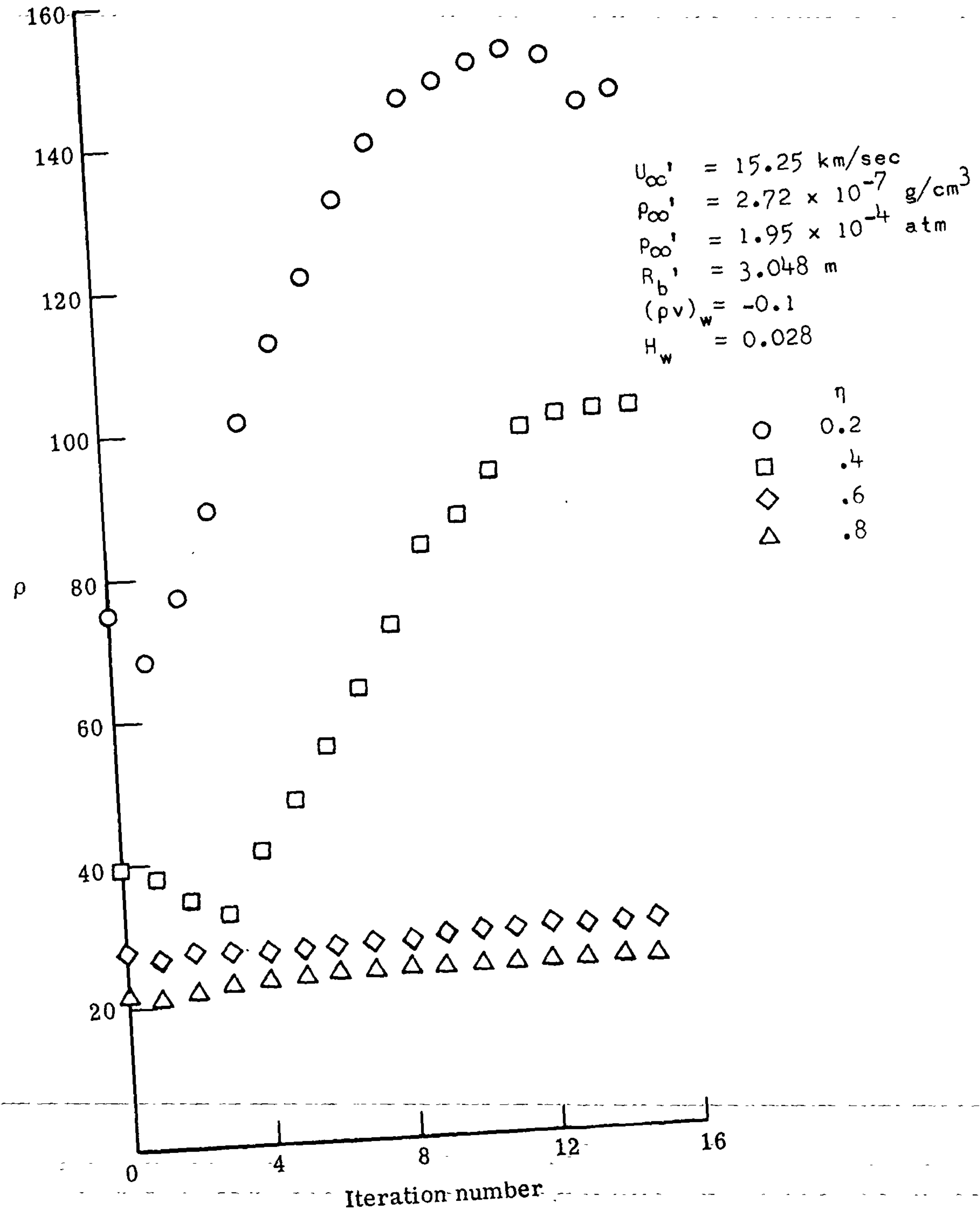

(a) Density behavior.

Figure 17.- Study of convergence of density and radiative heat flux.

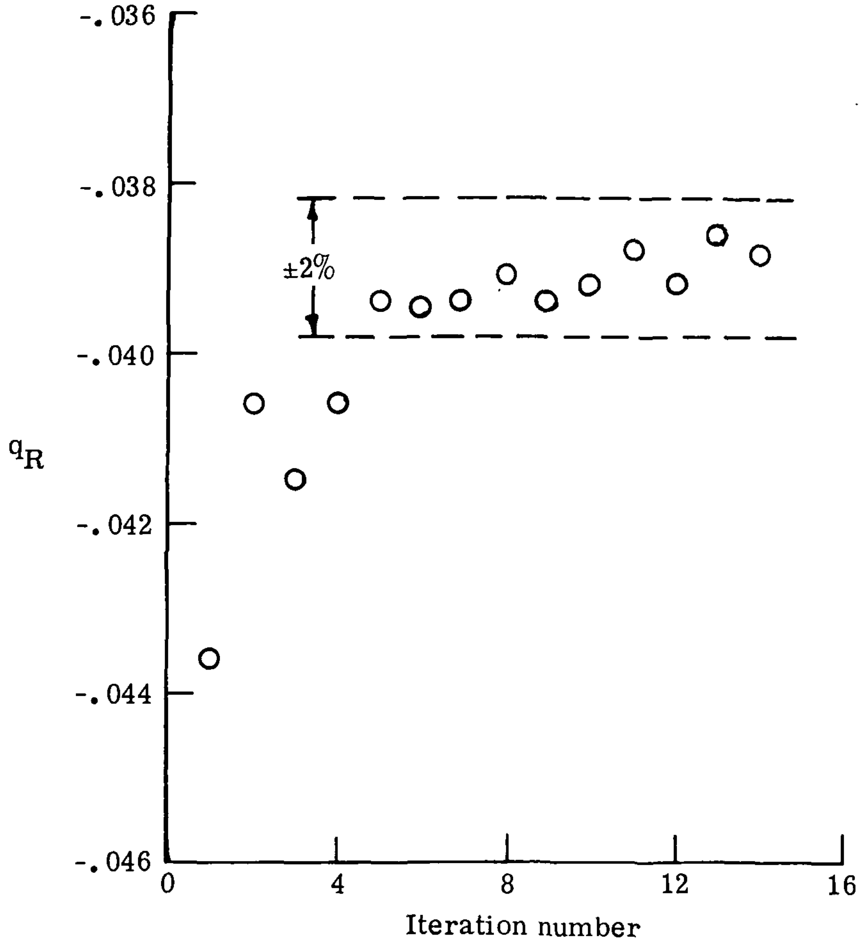

(b) Radiative-heat-flux behavior.

Figure 17.- Concluded.

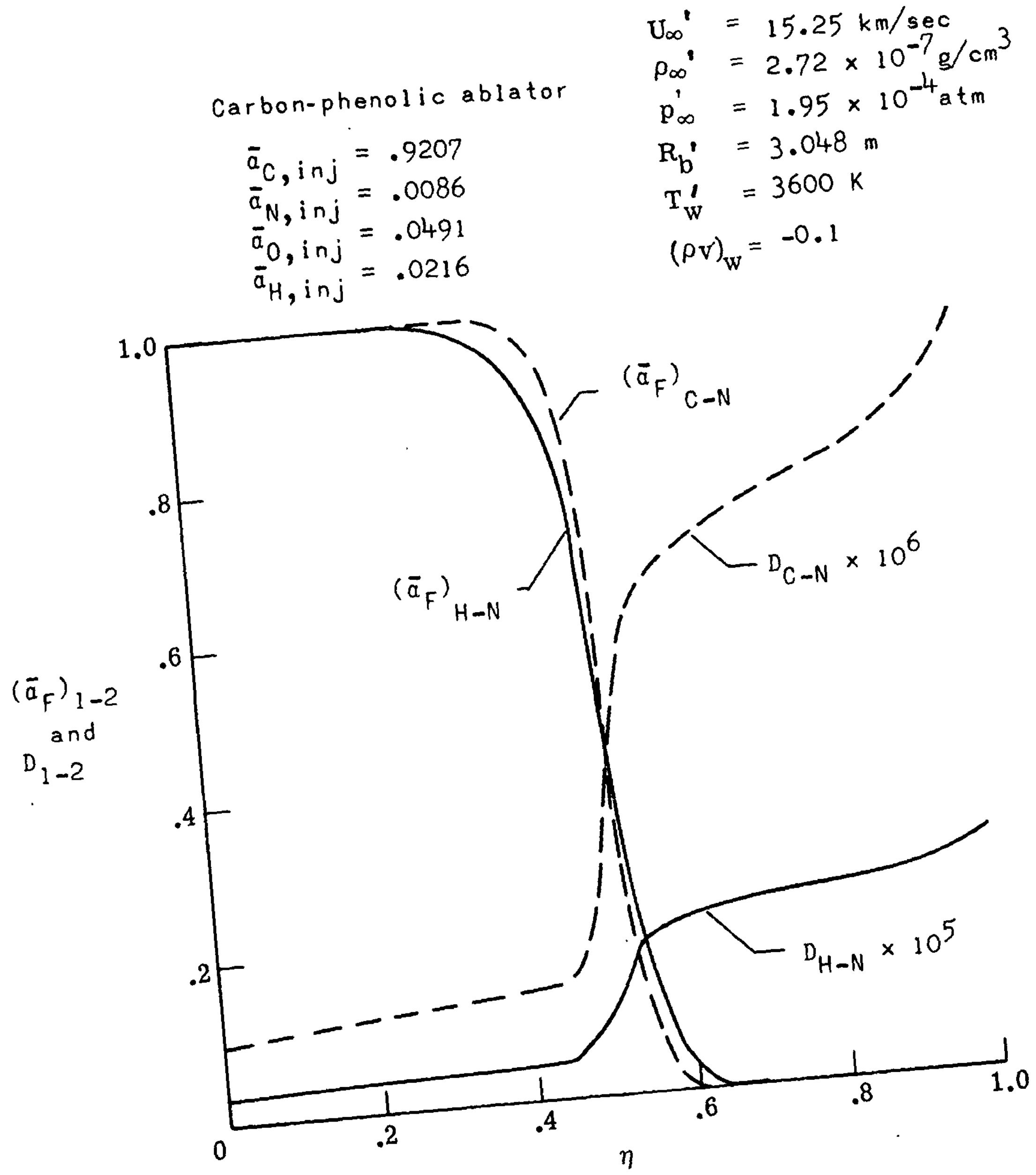

Figure 18.- Comparison of ablator mass-fraction profiles from solutions with binary carbon-nitrogen diffusion and hydrogen-nitrogen diffusion.

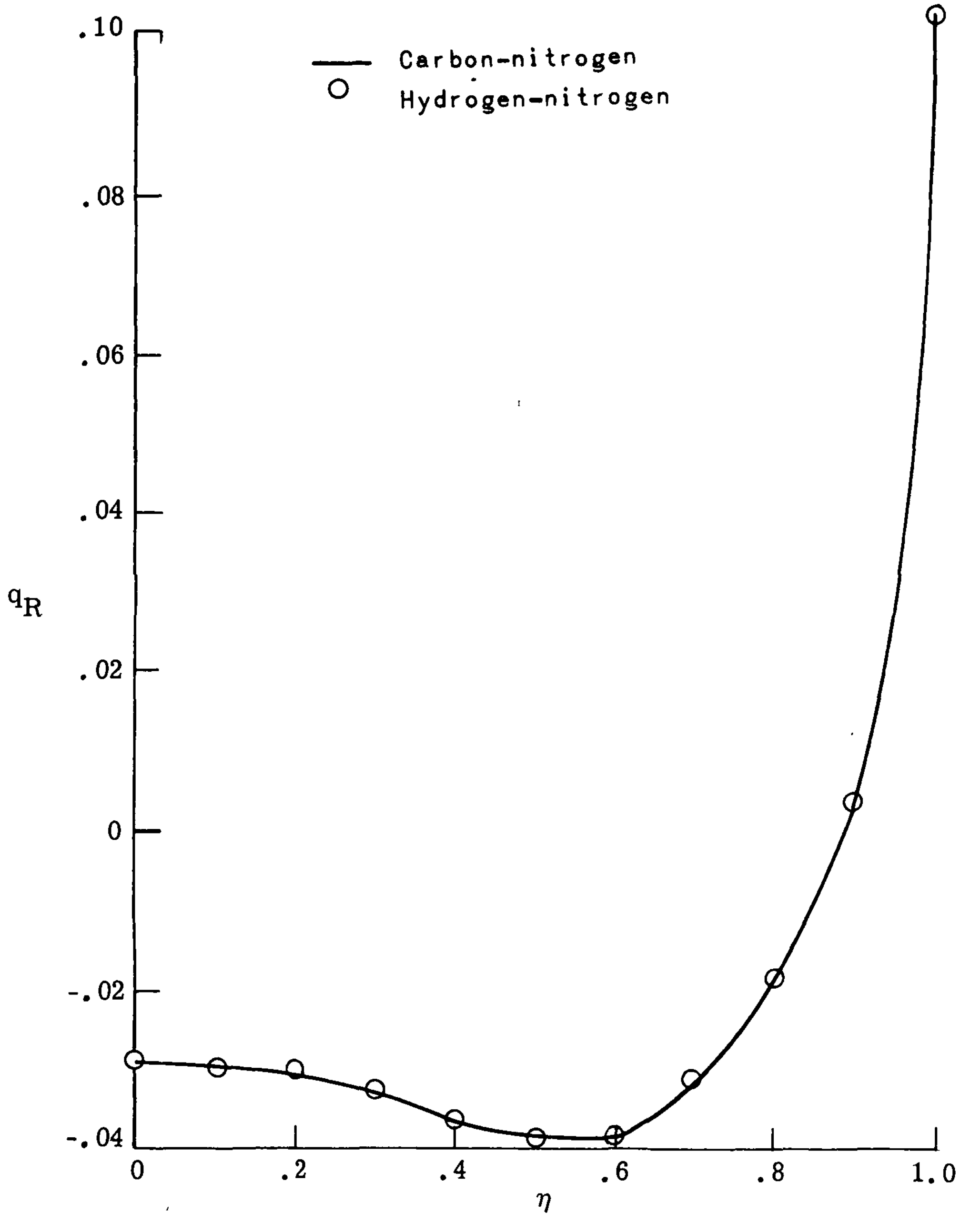

Figure 19.- Effect of the binary carbon-nitrogen and binary hydrogen-nitrogen diffusion models on the radiative heat fluxes.

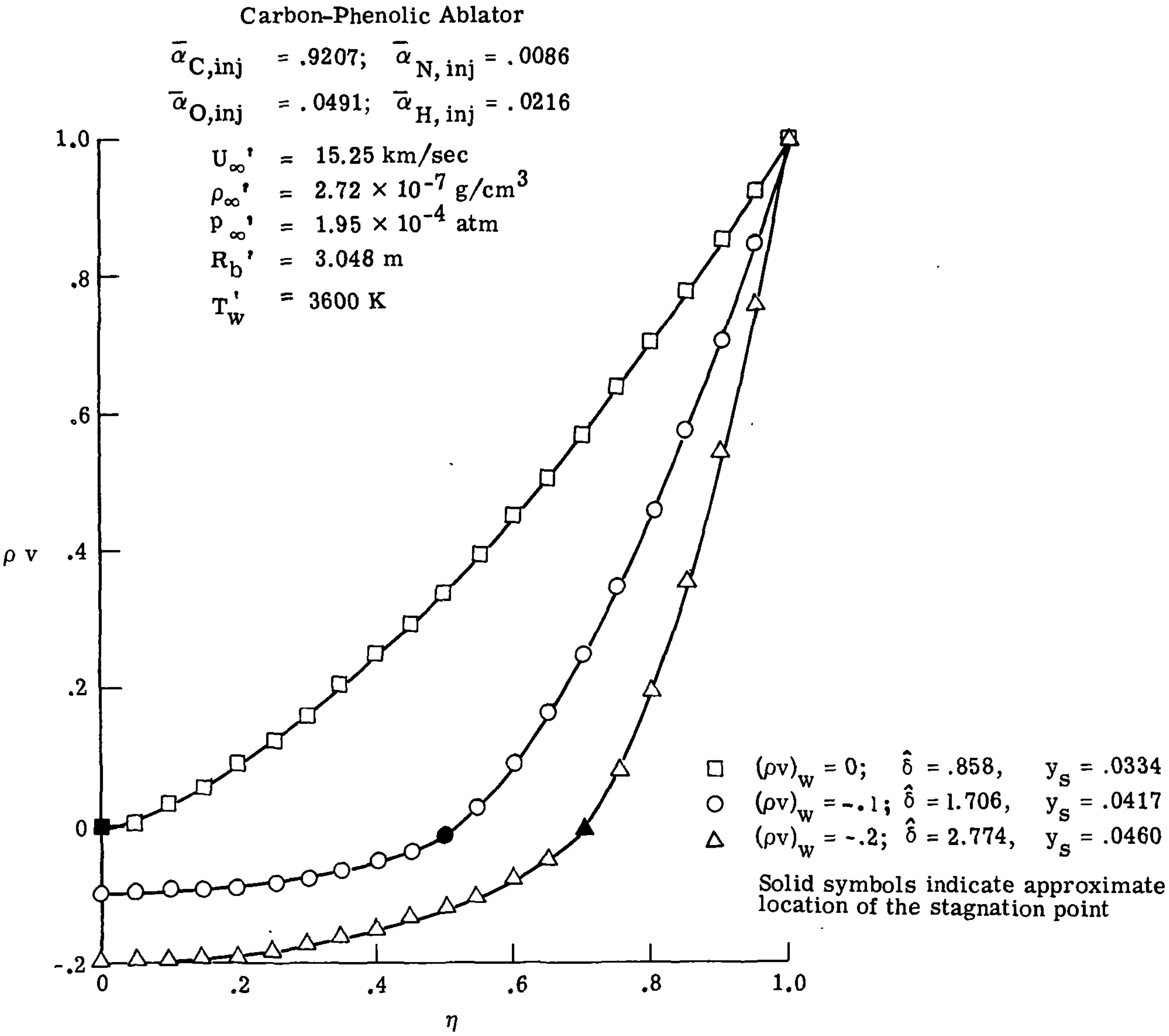

(a) Continuity equation.

Figure 20.- Solutions for radiating shock layer with injection of ablation products.

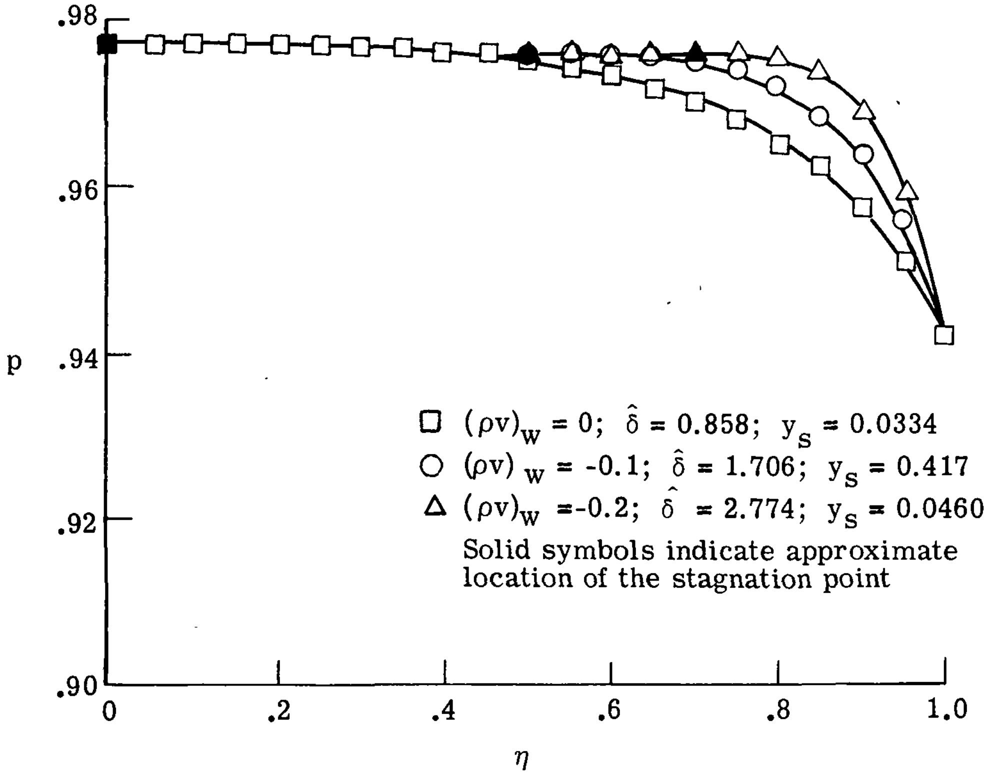

(b) y-momentum equation.

Figure 20.- Continued.

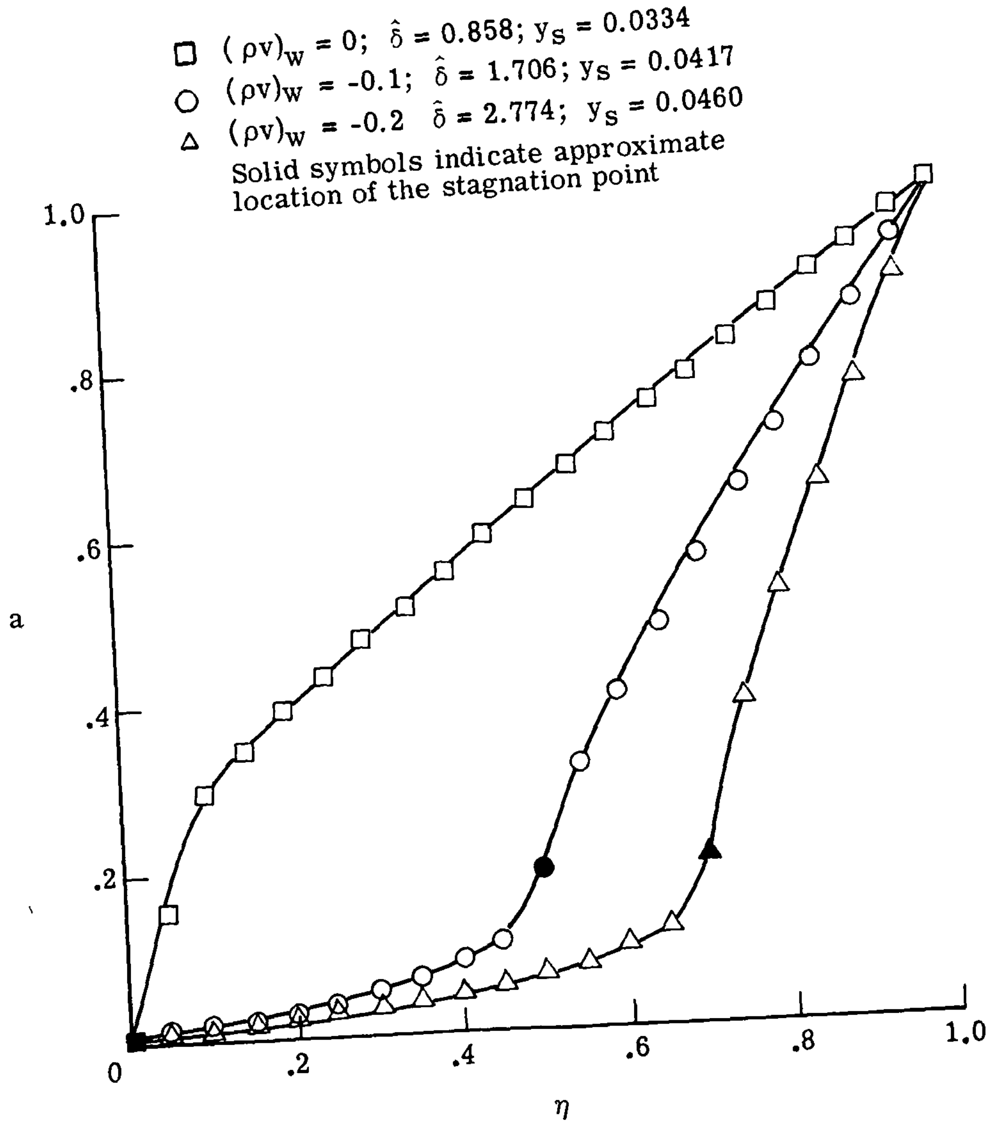

(c) x-momentum equation.

Figure 20.- Continued.

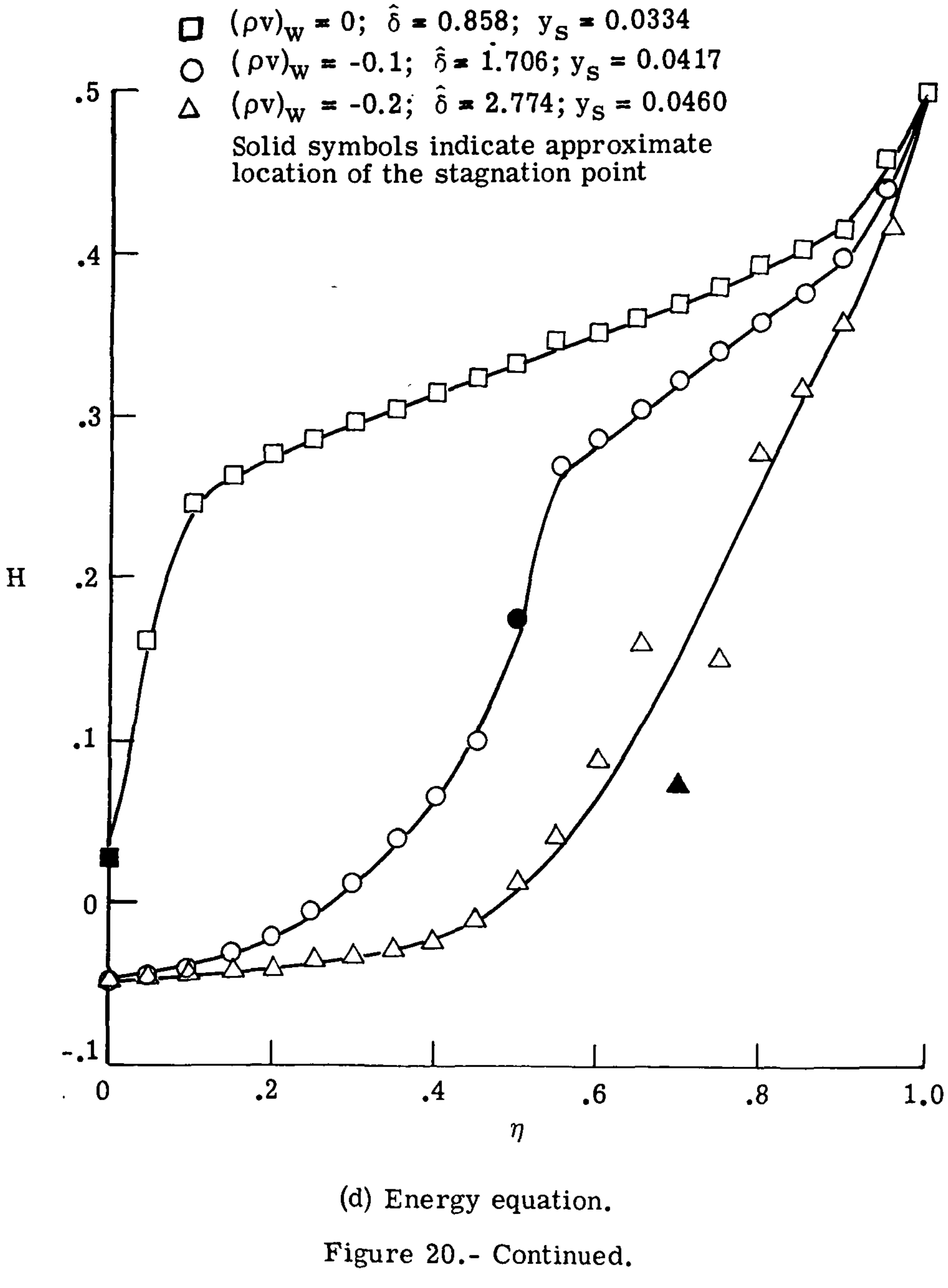

(d) Energy equation.

Figure 20.- Continued.

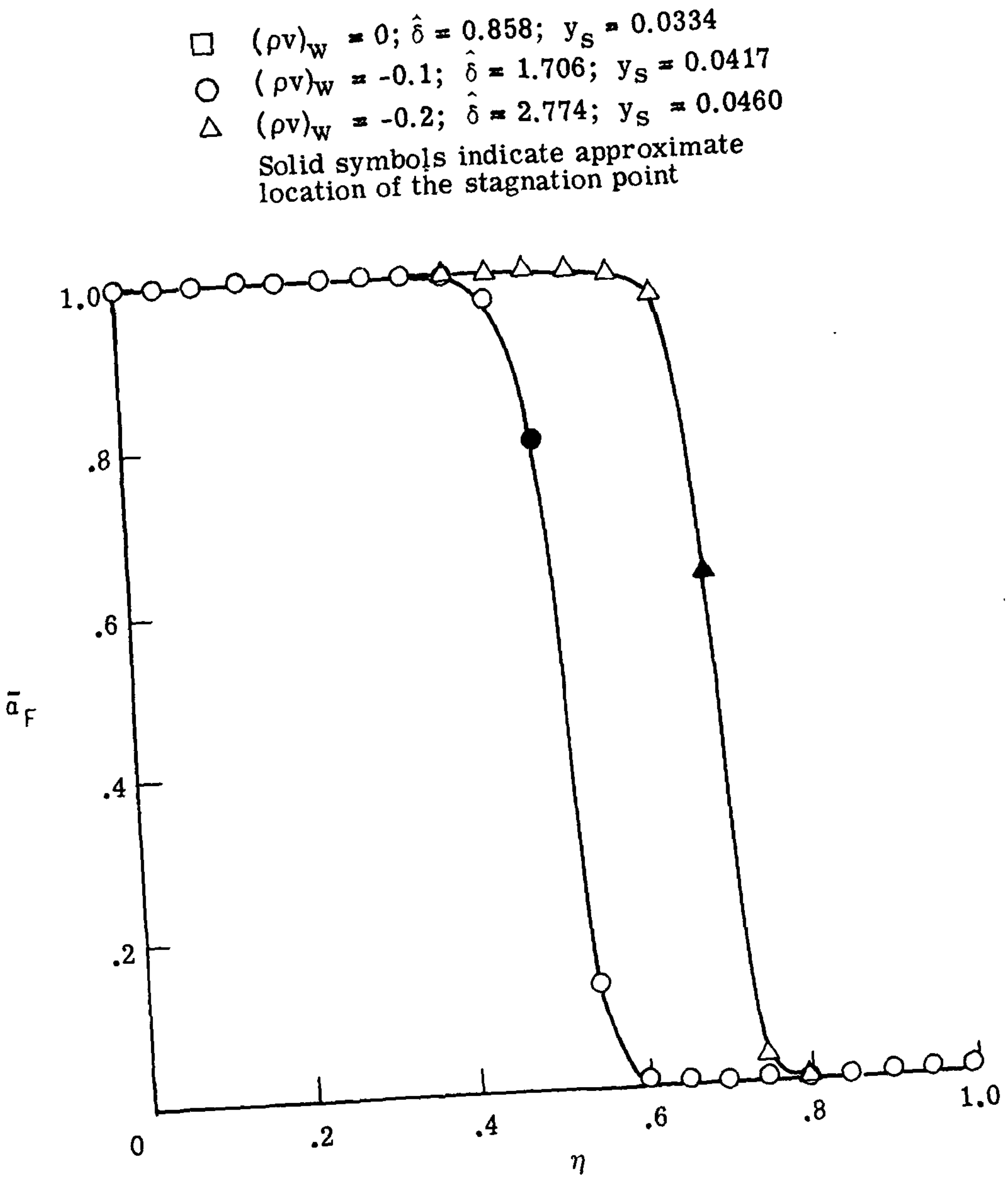

(e) Elemental-diffusion equation.

Figure 20.- Continued.

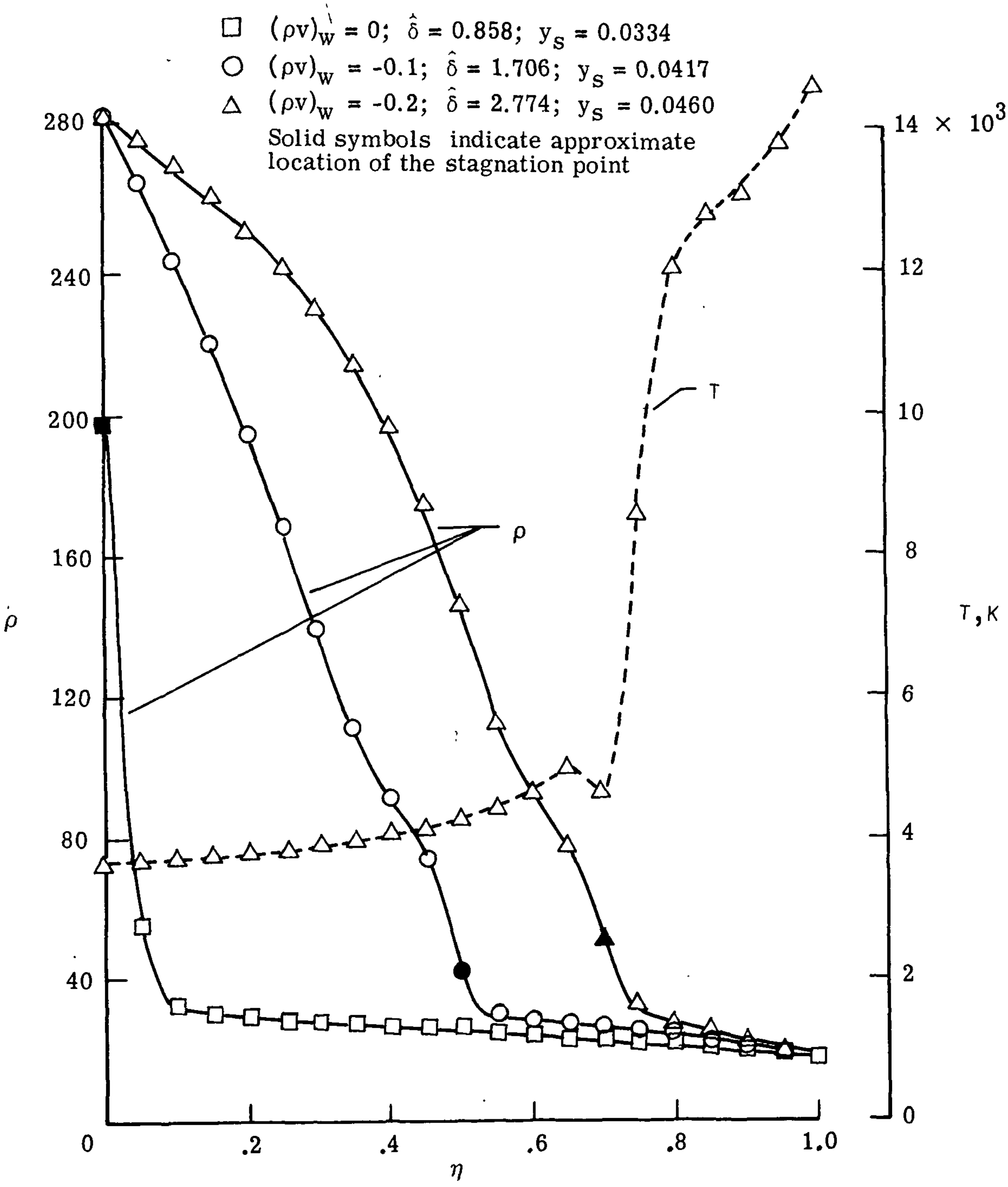

(f) Equation of state.

Figure 20.- Continued.

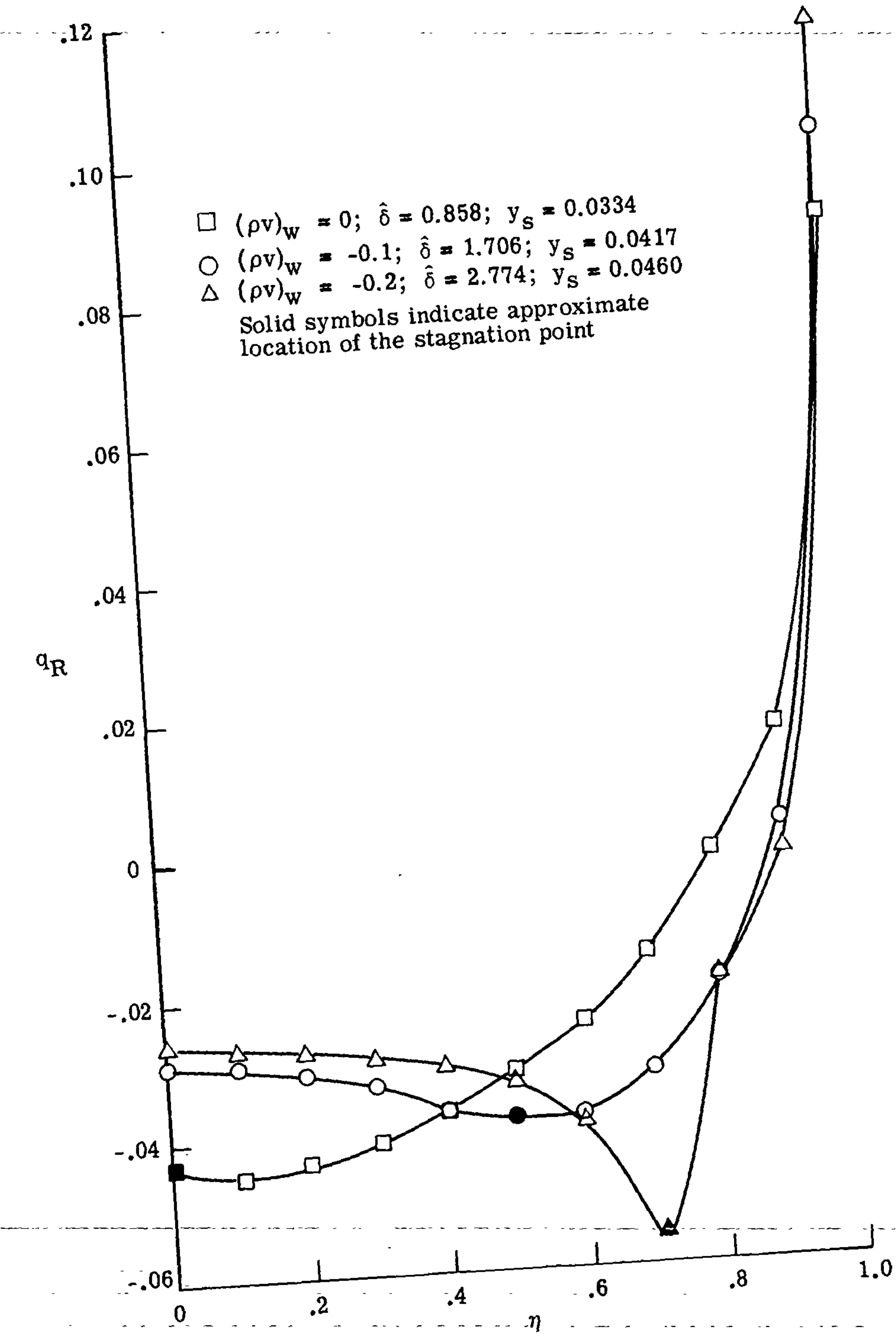

(g) Radiative heat flux.

Figure 20.- Concluded.

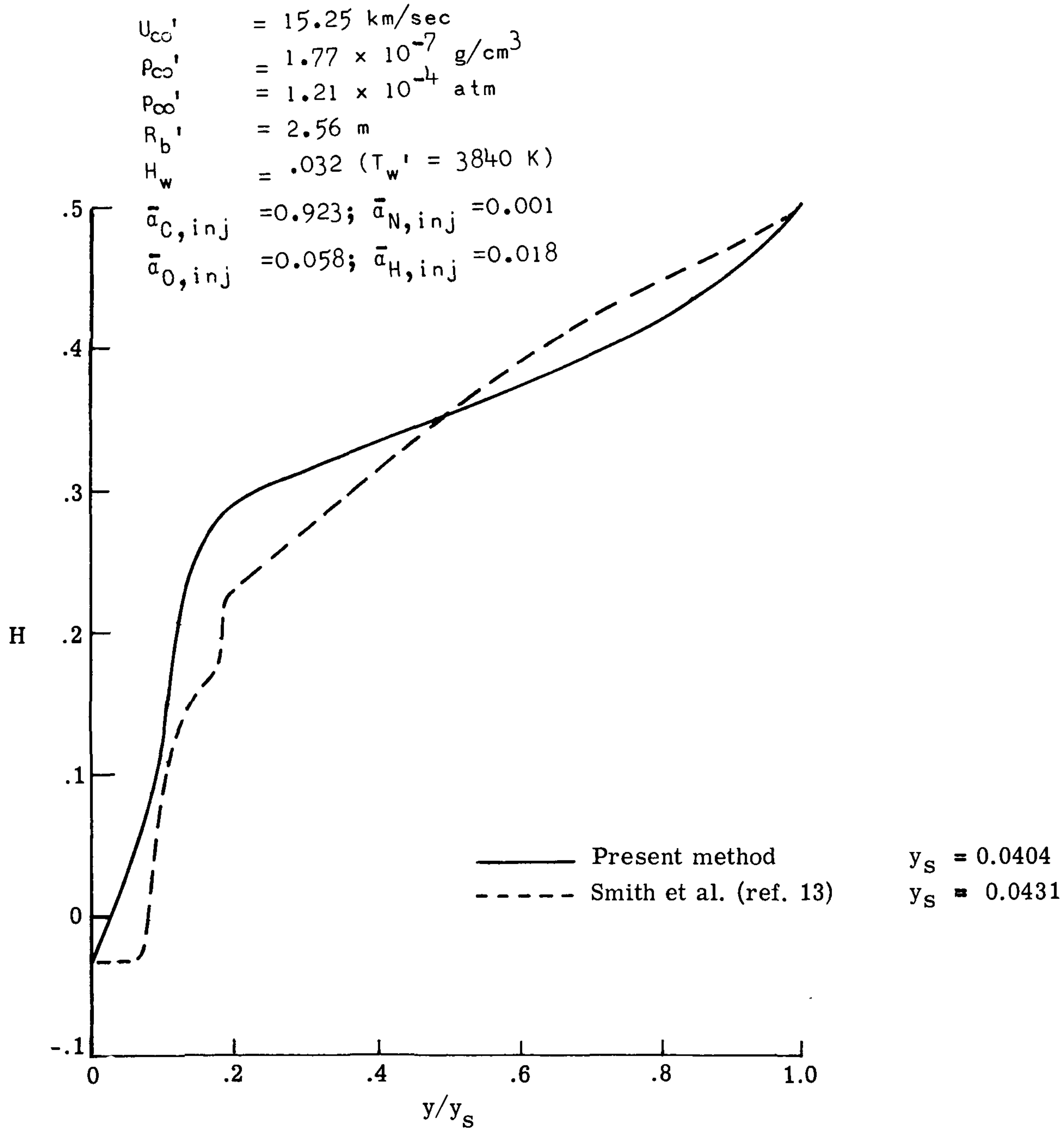

(a) Enthalpy.

Figure 21.- Comparison of flow-field results for carbon-phenolic injection at $(\rho v)_w = -0.076$.

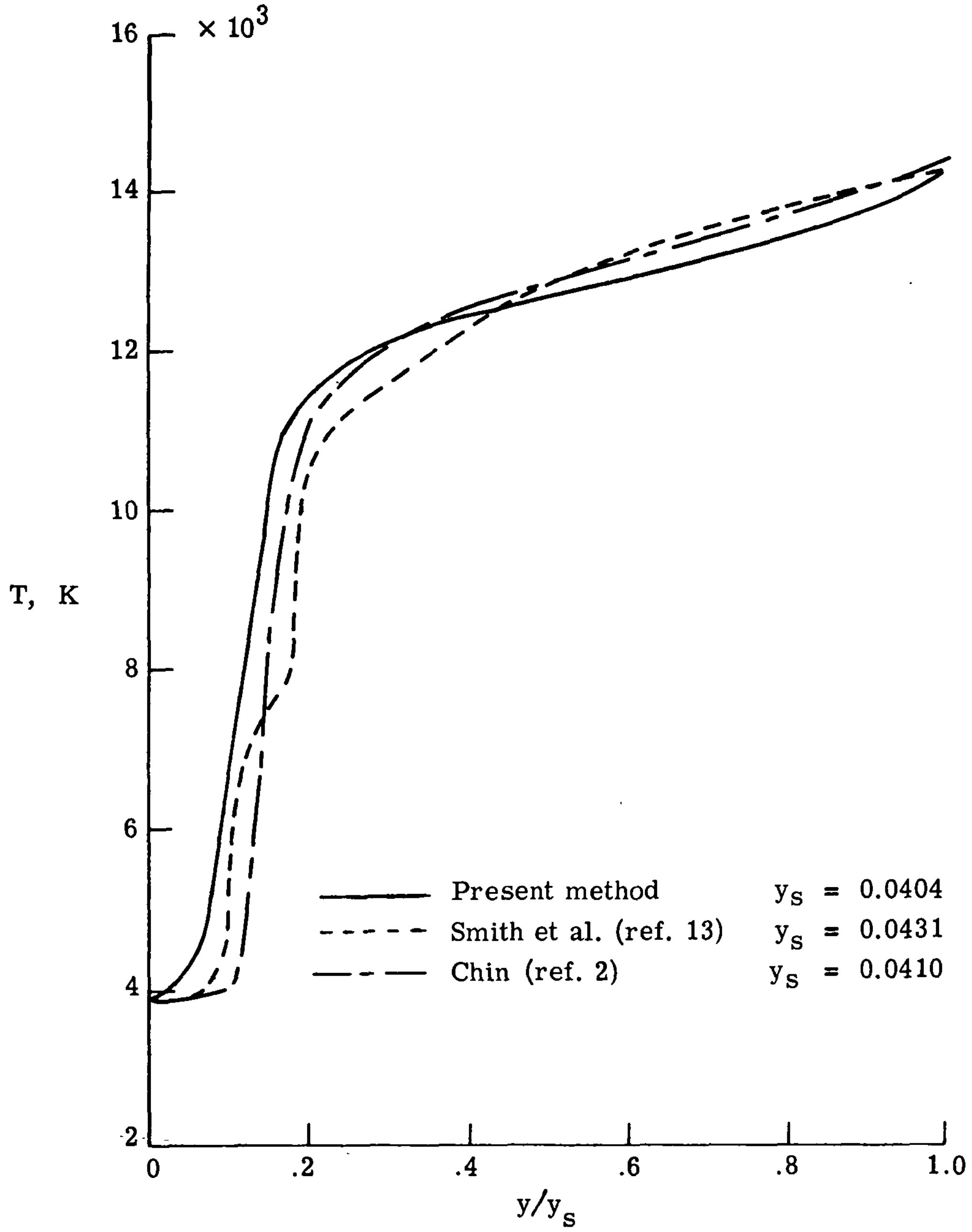

(b) Temperature.

Figure 21.- Continued.

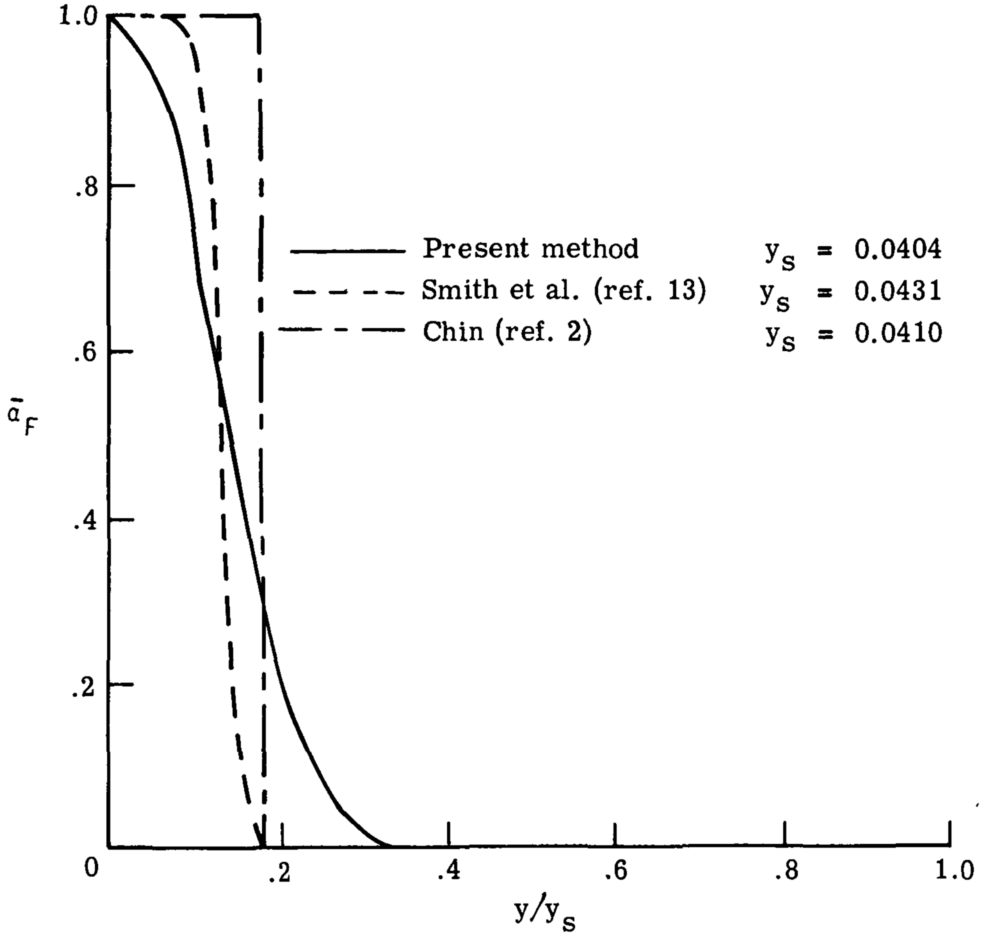

(c) Ablator mass fraction.

Figure 21.- Continued.

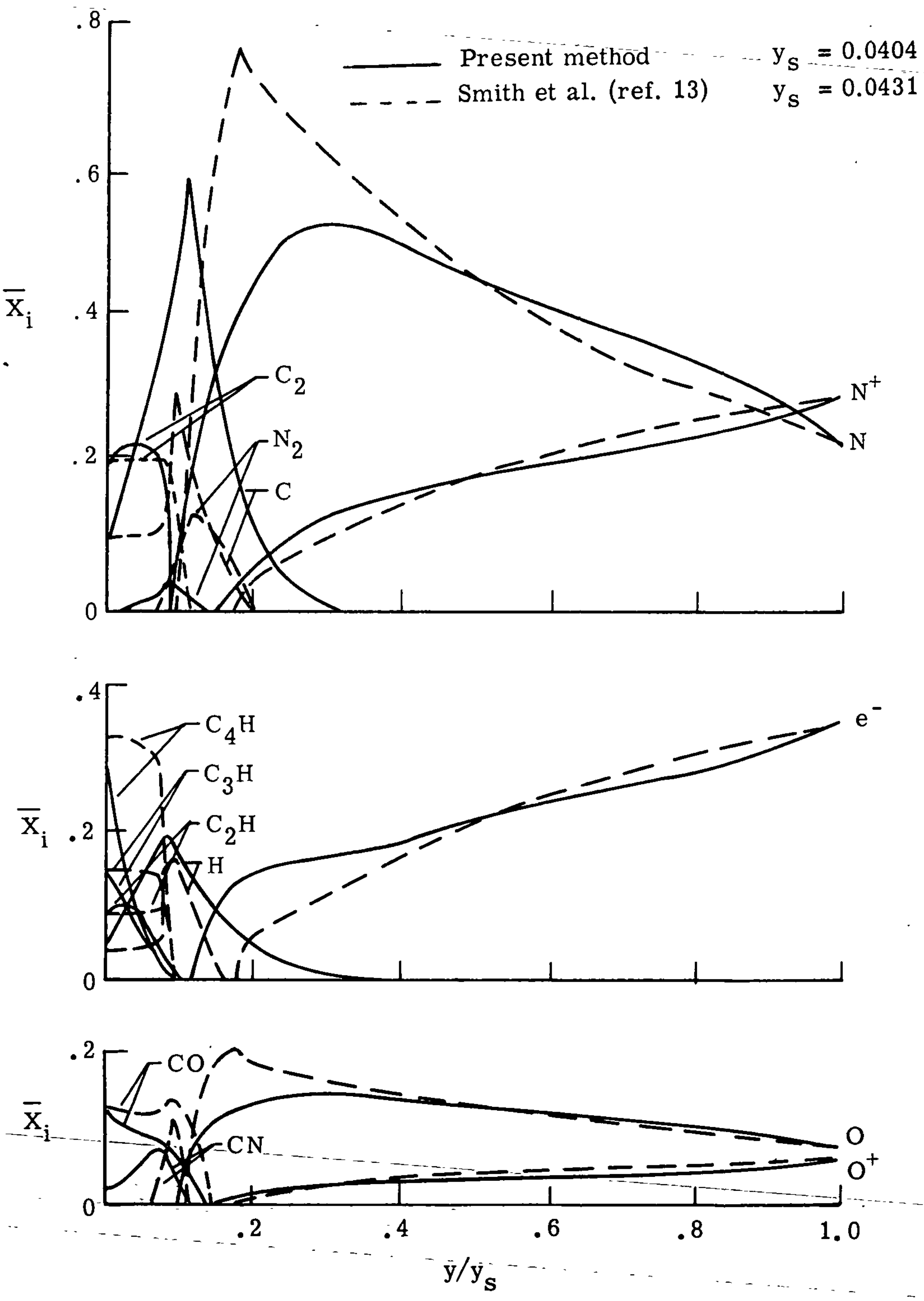

(d) Mole fractions.

Figure 21.- Continued.

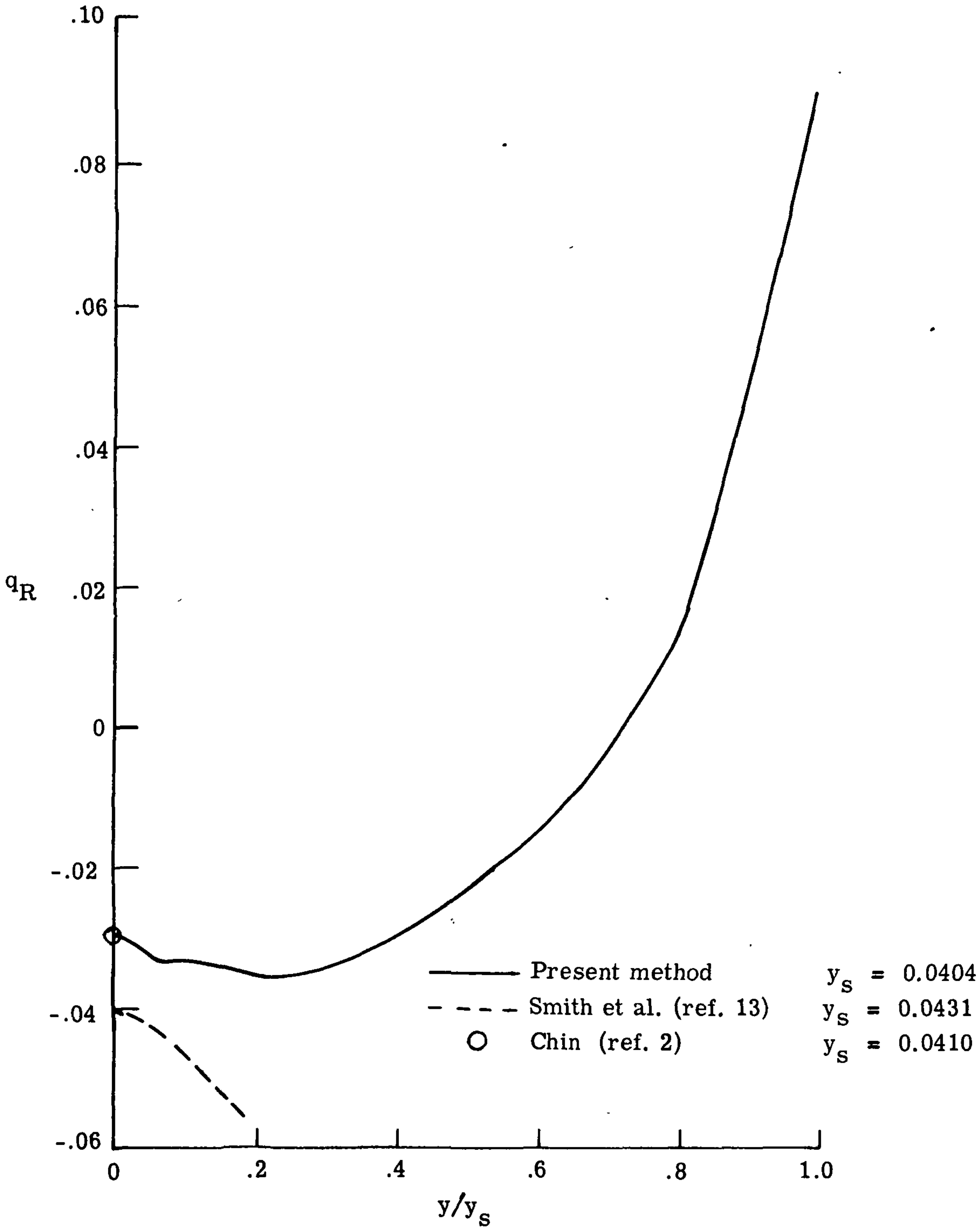

(e) Radiative heat flux.

Figure 21.- Concluded.

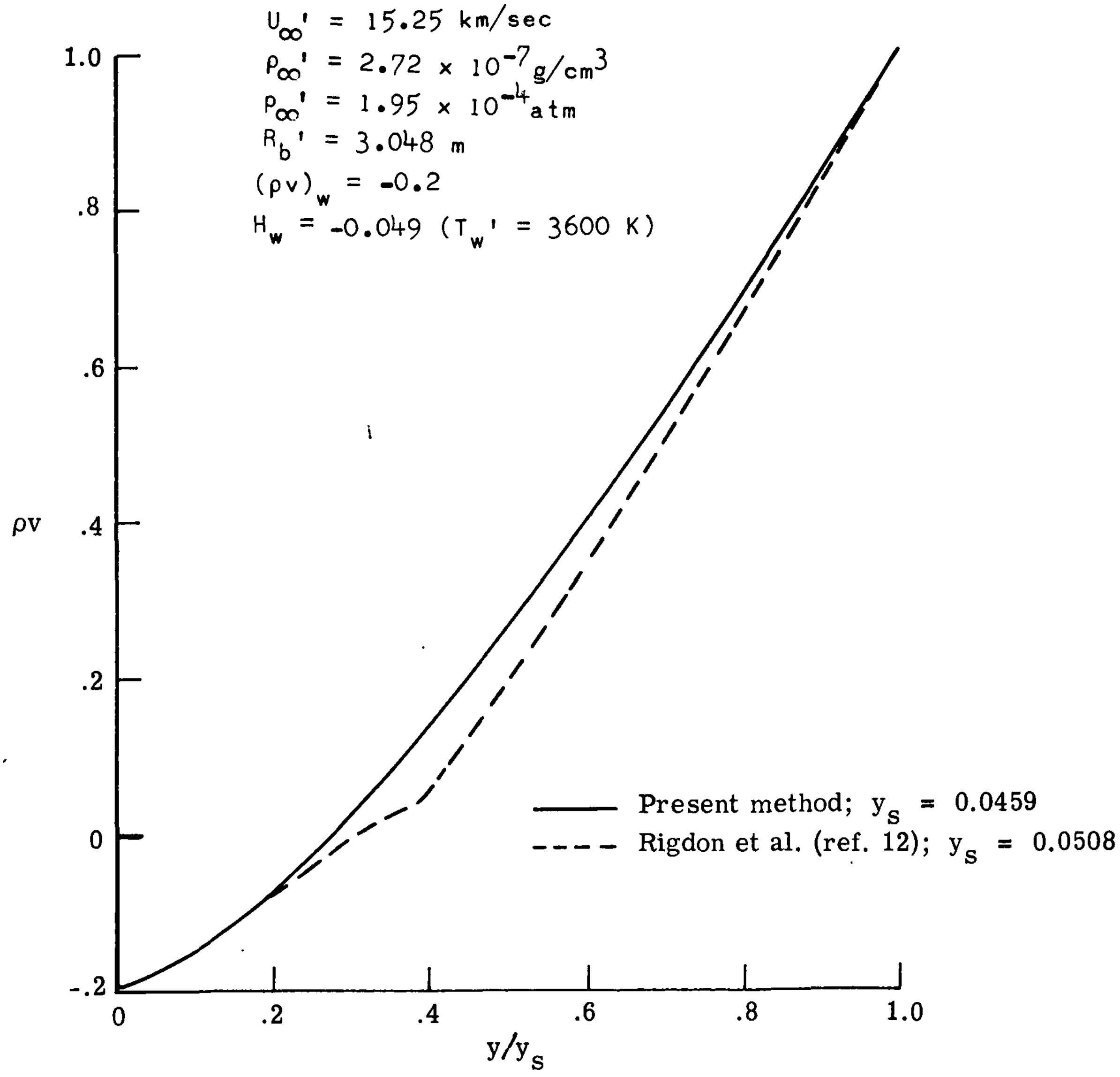

(a) Mass flux.

Figure 22.- Comparison of flow-field results for carbon-phenolic injection at $(\rho v)_w = -0.2$.

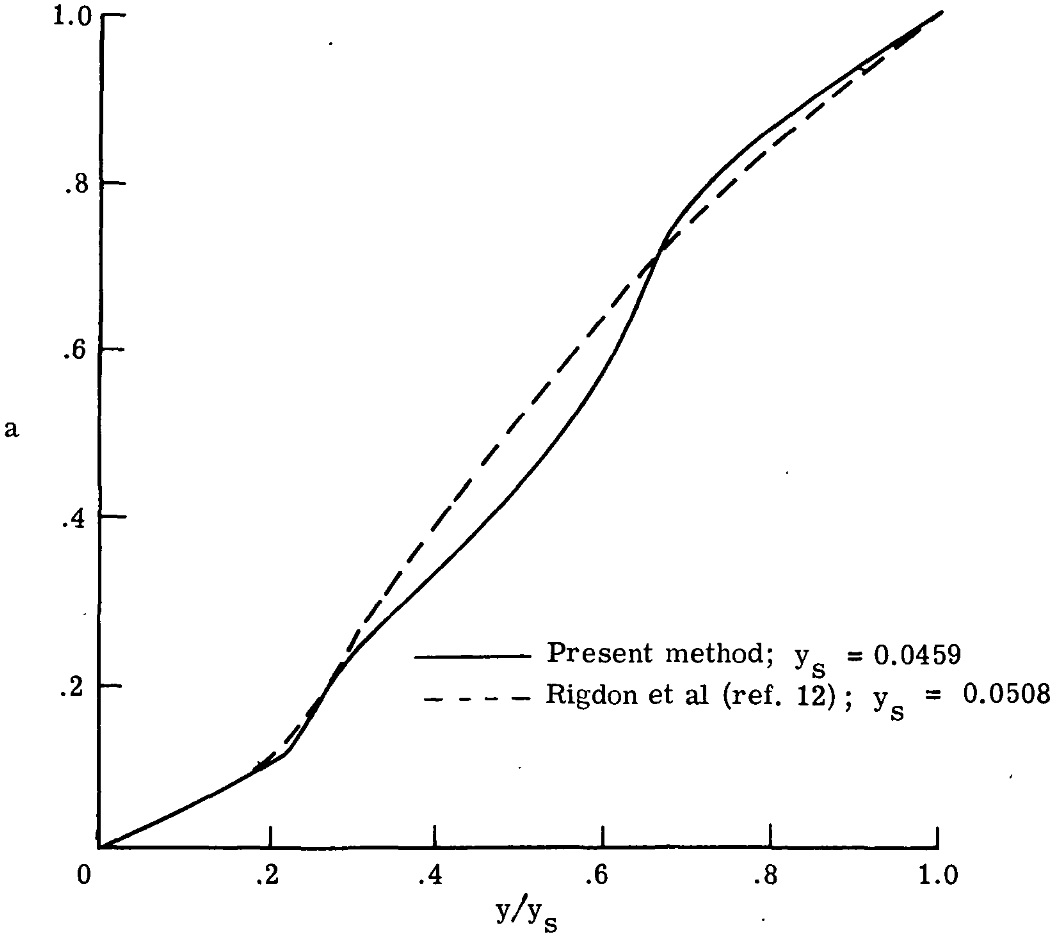

(b) Velocity gradient.

Figure 22.- Continued.

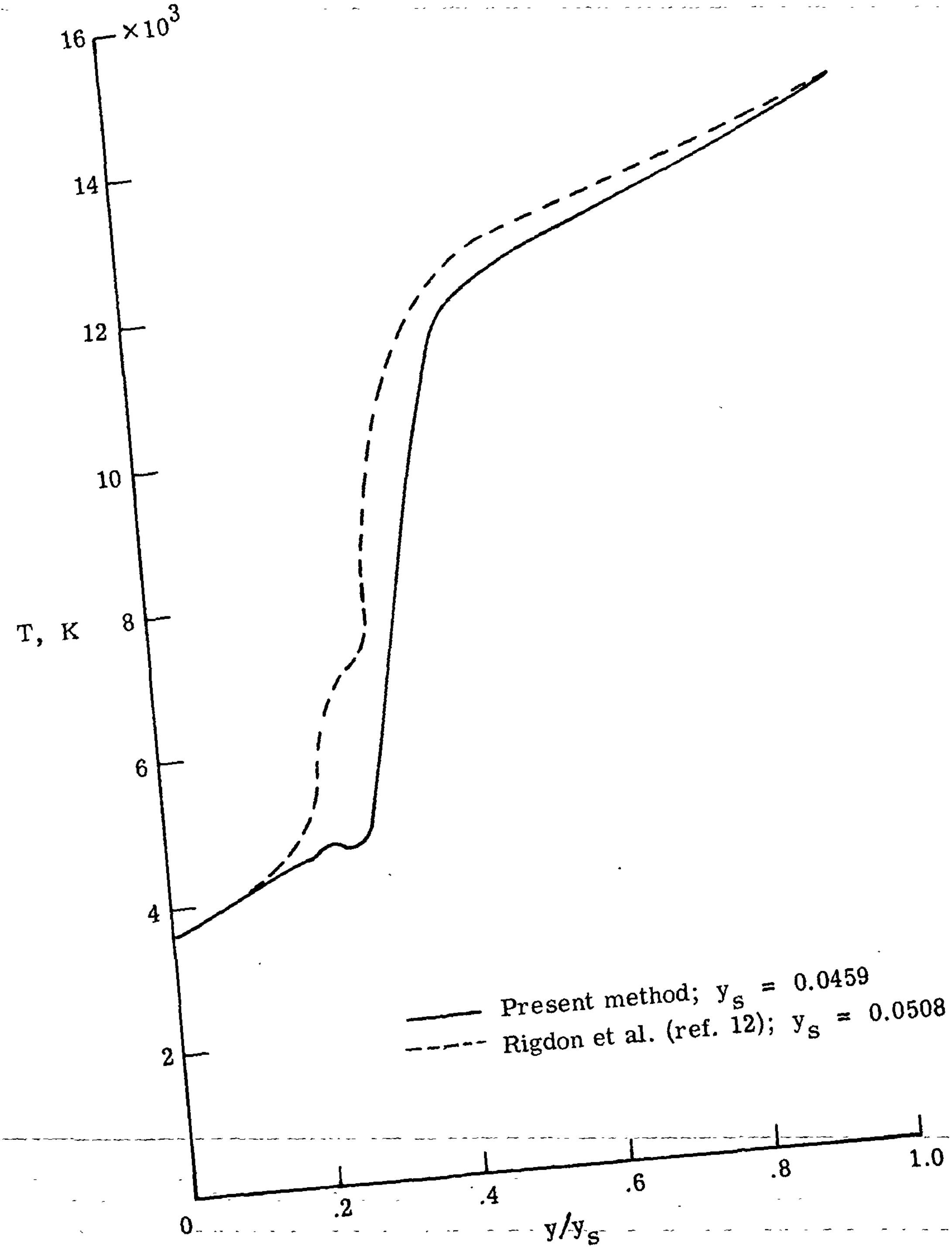

(c) Temperature.

Figure 22.- Continued.

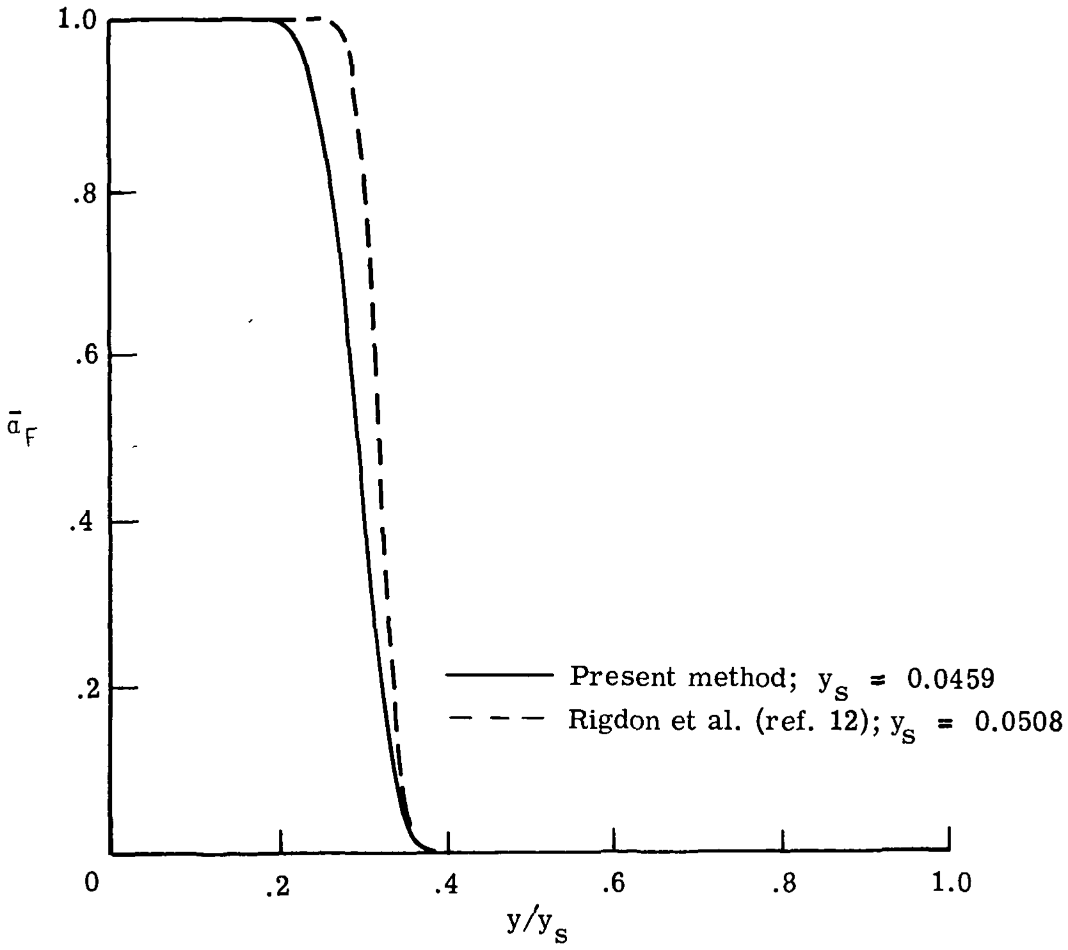

(d) Ablator mass fraction.

Figure 22.- Continued.

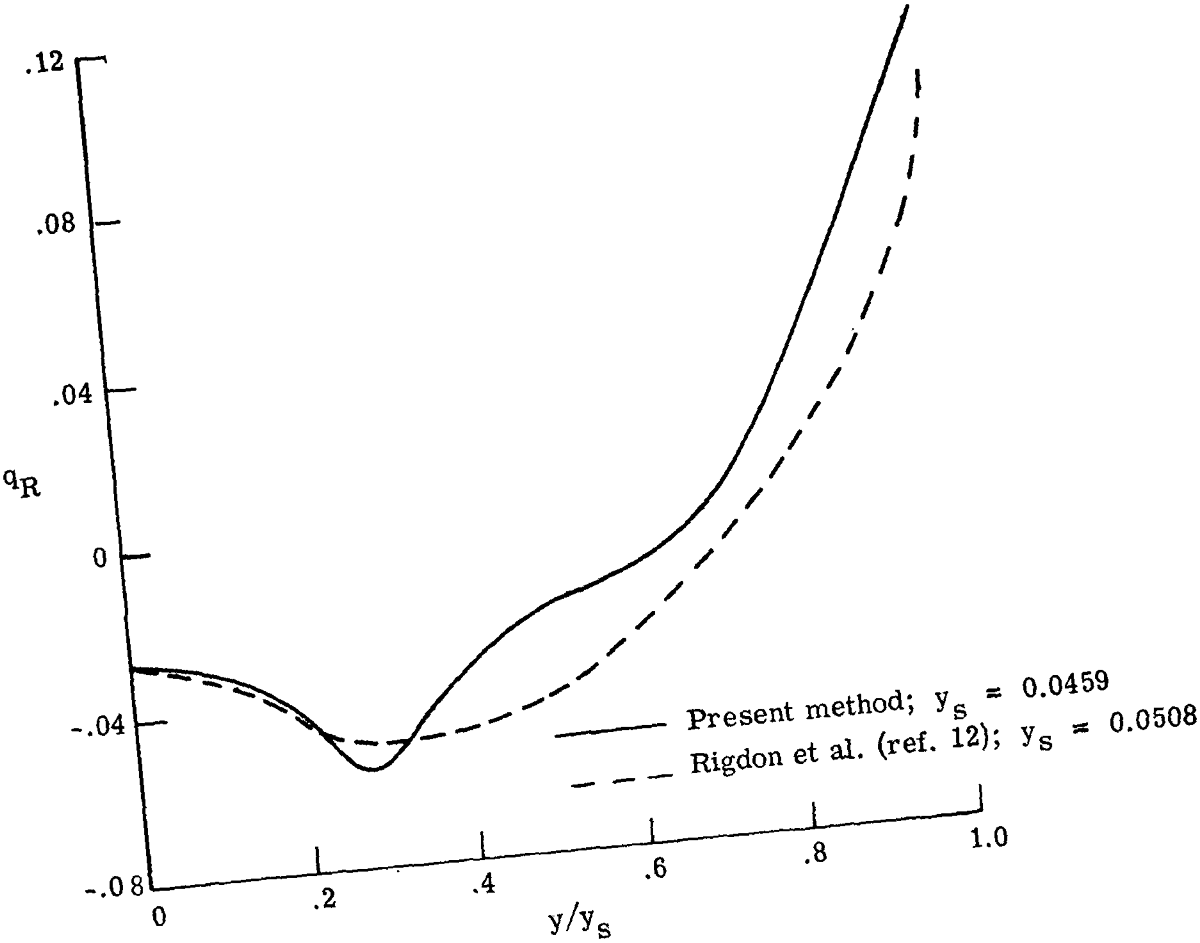

(e) Radiative heat flux.

Figure 22.- Concluded.

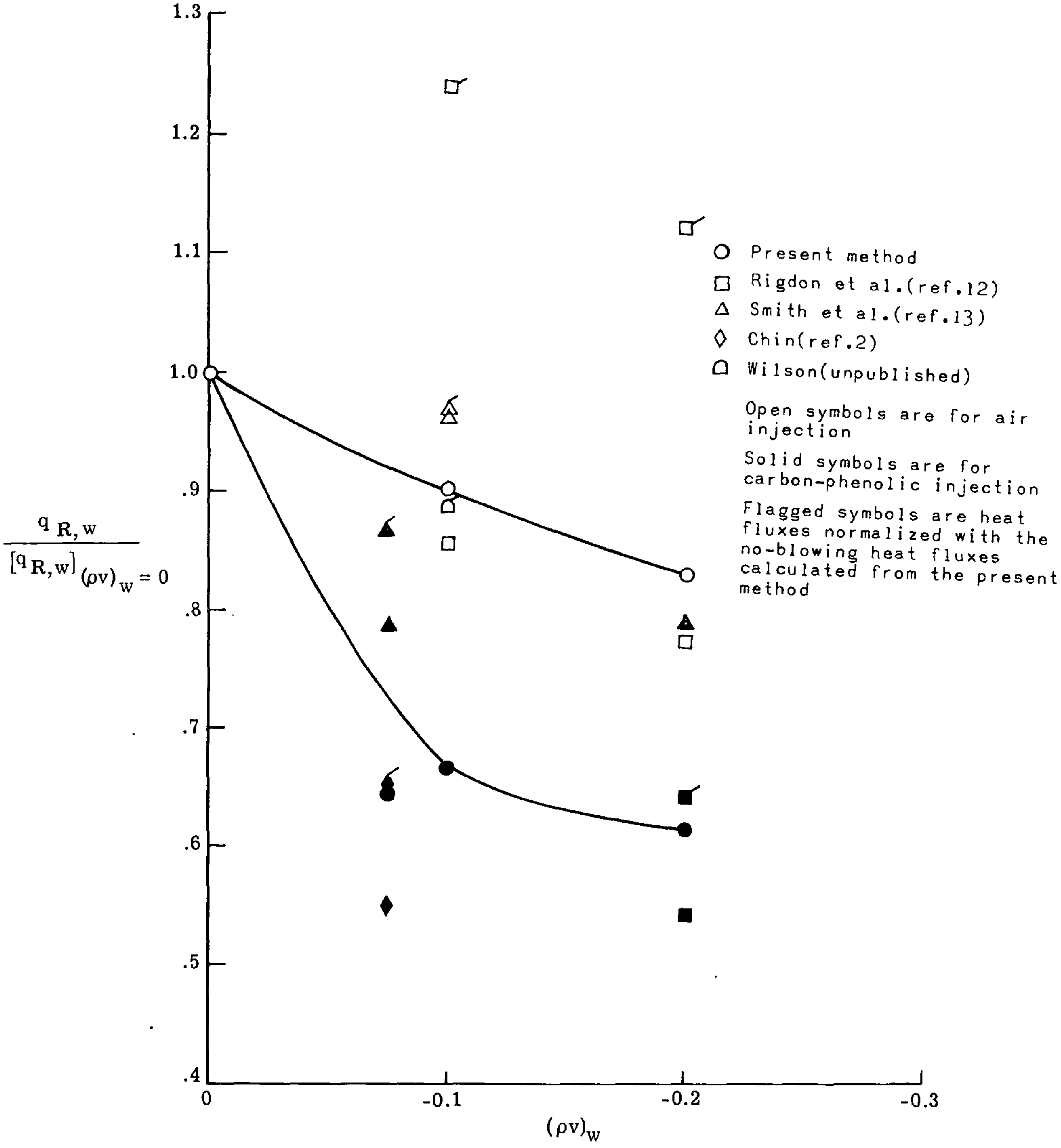

Figure 23.- Summary of wall radiative heat-flux predictions for air injection and for ablation-products injection. (Pertinent free-stream conditions and nose radii for each data point are given in table 2.)

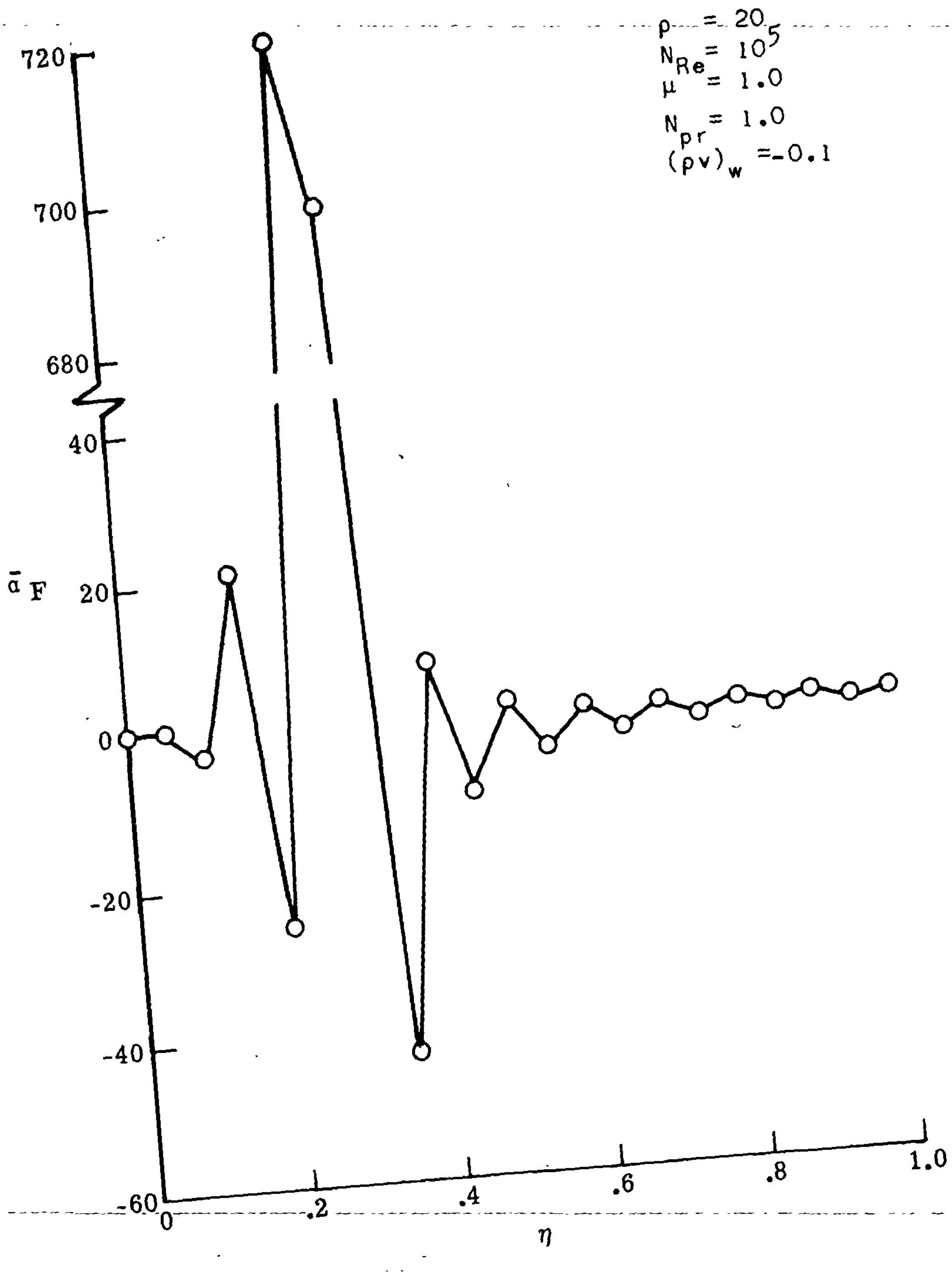

(a) $D_{12} = 10^{-6}$.

Figure 24.- Solution to the central-difference form of the elemental-diffusion equation for a constant-density flow.

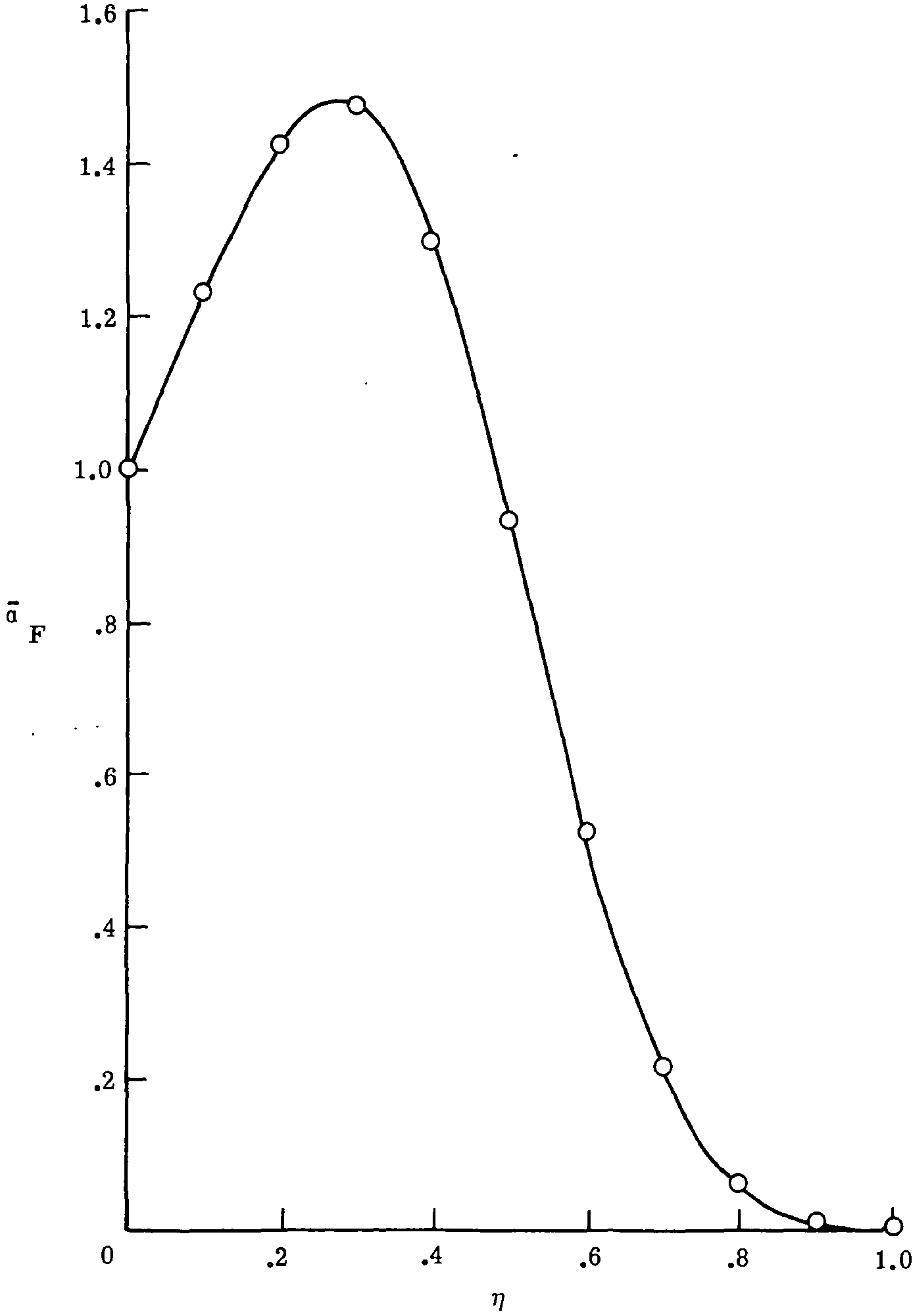

(b) $D_{12} = 1.25 \times 10^{-4}$.

Figure 24.- Concluded.

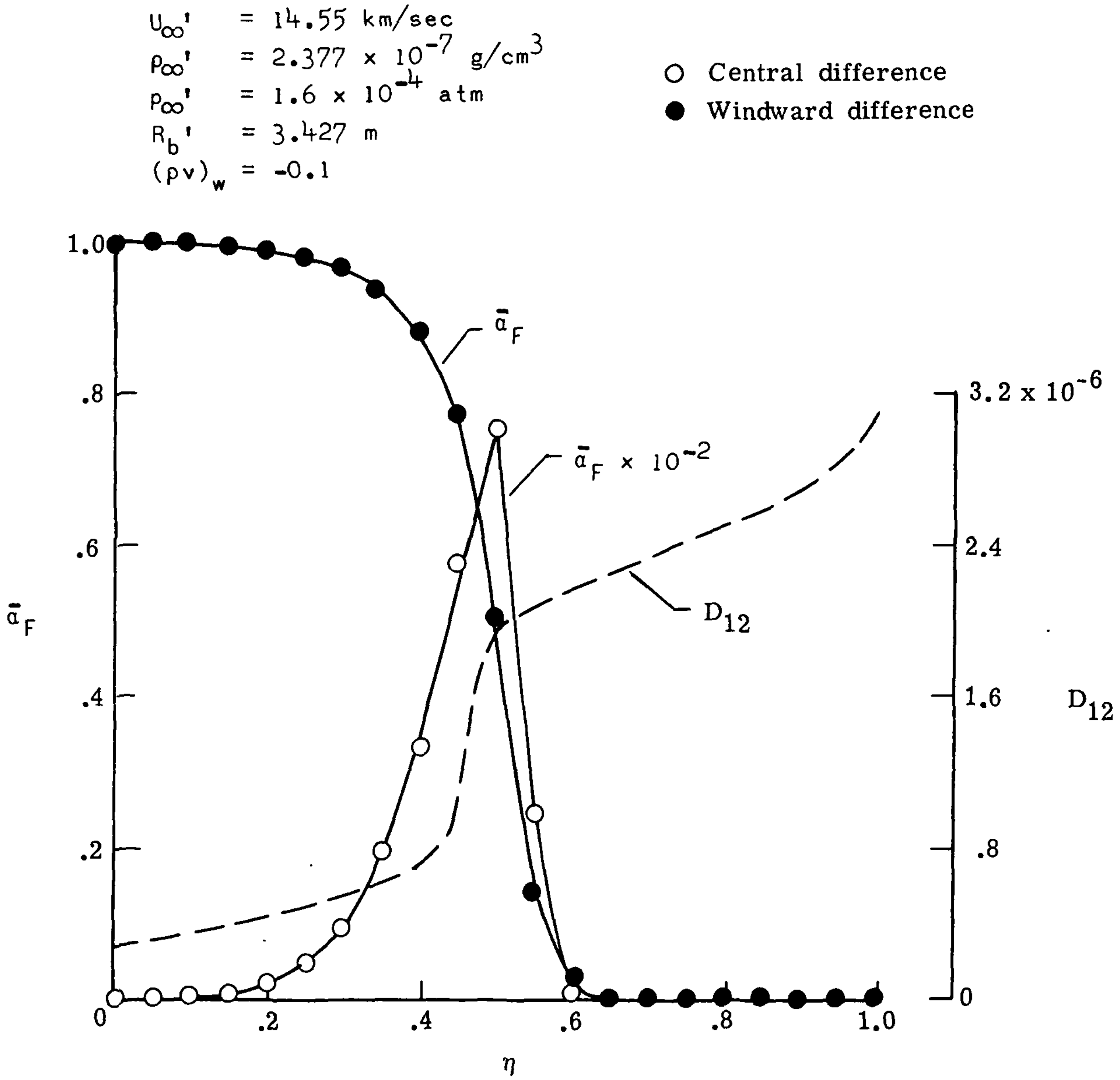

Figure 25.- Stability of the elemental-diffusion equation for central- and windward-difference approximations.

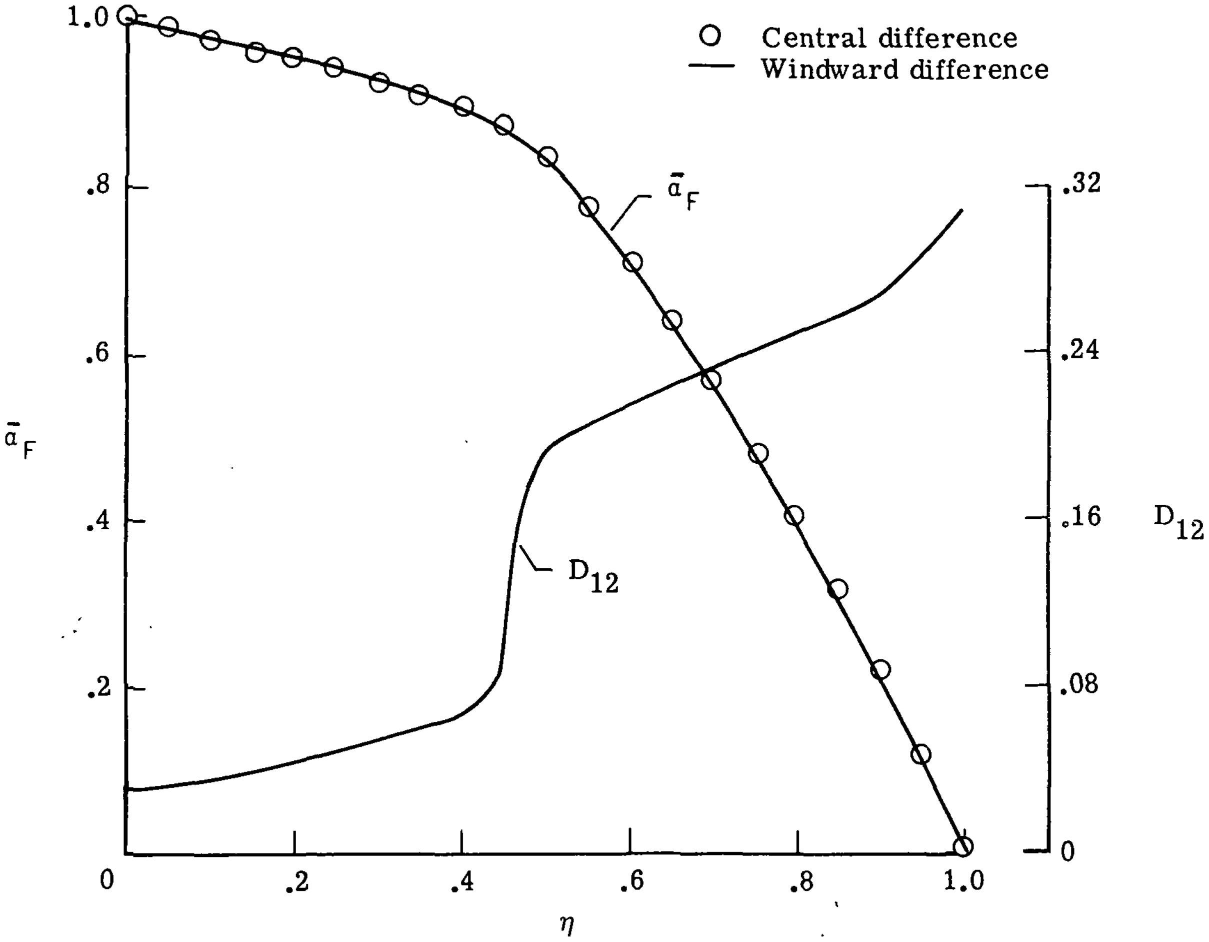

Figure 26.- Comparison of solutions of elemental-diffusion equation for central- and windward-difference approximations in the region where the equations are stable.

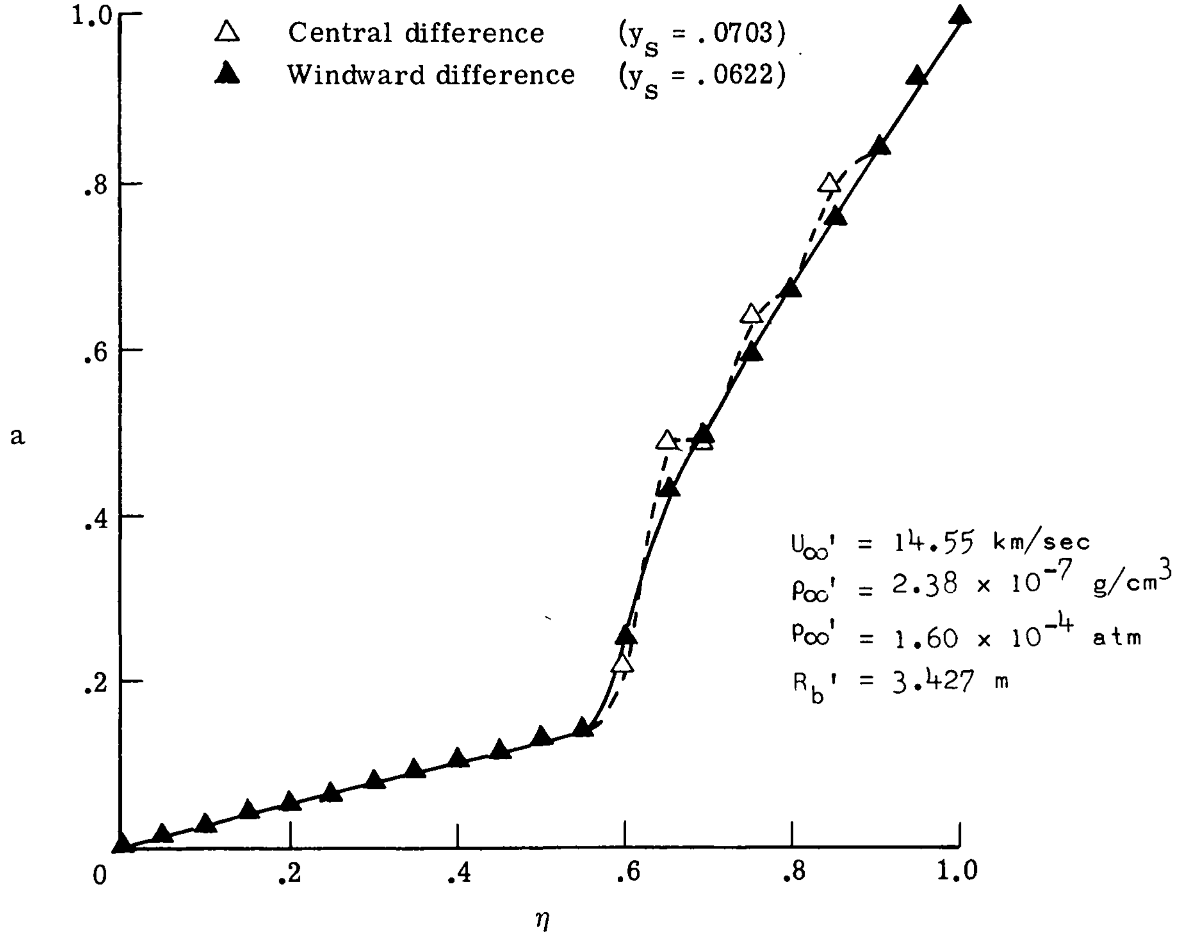

(a) x-momentum equations.

Figure 27.- Effect of windward differencing the energy equation on the solution for nonradiating air with massive blowing $(\rho v)_w = -0.2$.

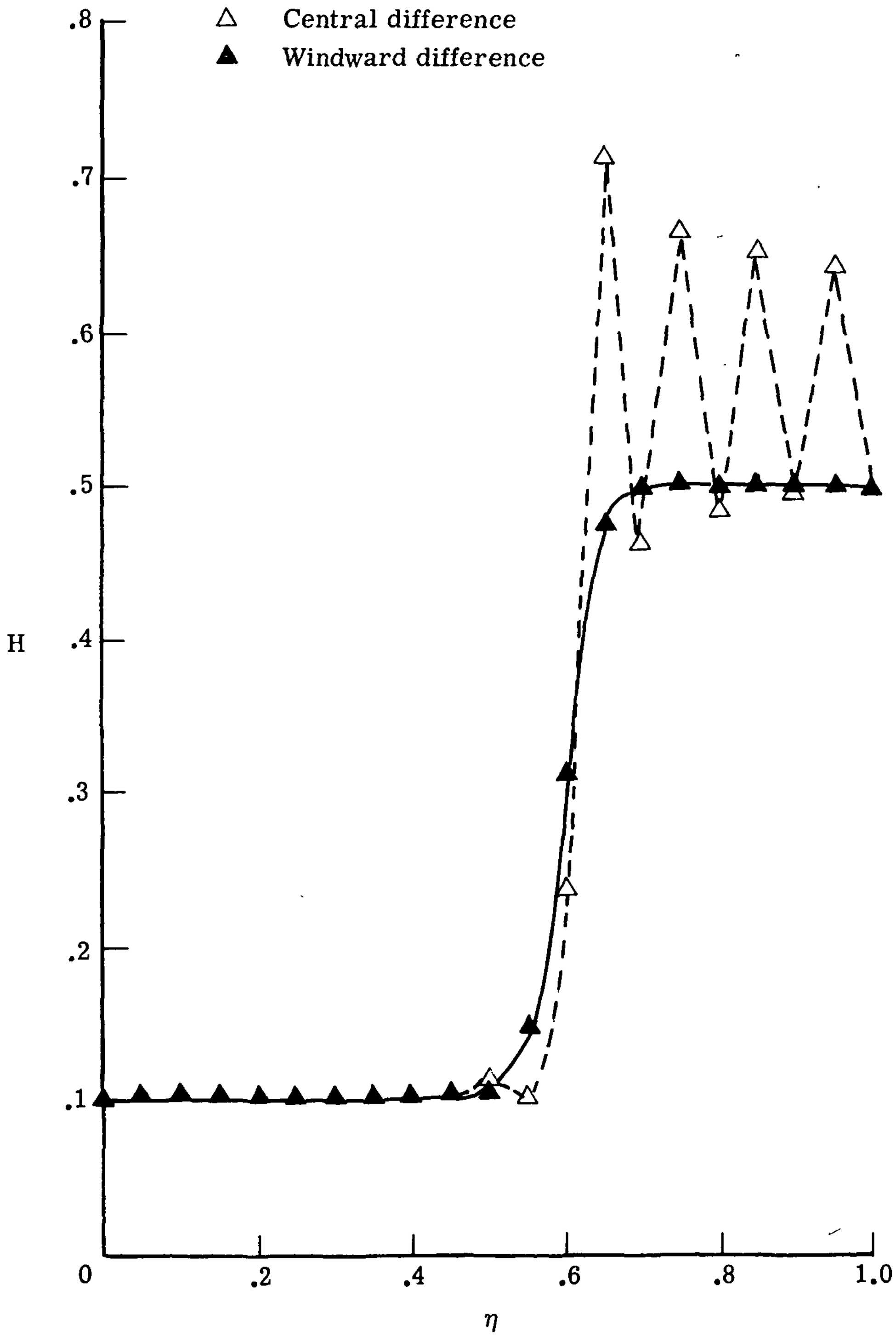

(b) Energy equation.

Figure 27.- Concluded.

NASA-Langley, 1972 —— 12 L-8302

NATIONAL AERONAUTICS AND SPACE ADMINISTRATION
WASHINGTON, D.C. 20546

OFFICIAL BUSINESS
PENALTY FOR PRIVATE USE $300

SPECIAL FOURTH-CLASS RATE
BOOK

POSTAGE AND FEES PAID
NATIONAL AERONAUTICS AND
SPACE ADMINISTRATION
451

U.S.MAIL

POSTMASTER: If Undeliverable (Section 158
Postal Manual) Do Not Return

> *"The aeronautical and space activities of the United States shall be conducted so as to contribute . . . to the expansion of human knowledge of phenomena in the atmosphere and space. The Administration shall provide for the widest practicable and appropriate dissemination of information concerning its activities and the results thereof."*
>
> —NATIONAL AERONAUTICS AND SPACE ACT OF 1958

NASA SCIENTIFIC AND TECHNICAL PUBLICATIONS

TECHNICAL REPORTS: Scientific and technical information considered important, complete, and a lasting contribution to existing knowledge.

TECHNICAL NOTES: Information less broad in scope but nevertheless of importance as a contribution to existing knowledge.

TECHNICAL MEMORANDUMS: Information receiving limited distribution because of preliminary data, security classification, or other reasons. Also includes conference proceedings with either limited or unlimited distribution.

CONTRACTOR REPORTS: Scientific and technical information generated under a NASA contract or grant and considered an important contribution to existing knowledge.

TECHNICAL TRANSLATIONS: Information published in a foreign language considered to merit NASA distribution in English.

SPECIAL PUBLICATIONS: Information derived from or of value to NASA activities. Publications include final reports of major projects, monographs, data compilations, handbooks, sourcebooks, and special bibliographies.

TECHNOLOGY UTILIZATION PUBLICATIONS: Information on technology used by NASA that may be of particular interest in commercial and other non-aerospace applications. Publications include Tech Briefs, Technology Utilization Reports and Technology Surveys.

Details on the availability of these publications may be obtained from:

SCIENTIFIC AND TECHNICAL INFORMATION OFFICE

NATIONAL AERONAUTICS AND SPACE ADMINISTRATION

Washington, D.C. 20546